Title	Amorphization and creation of lattice defects in crystalline Si by electron irradiation at low temperature
Author(s)	山崎, 順
Citation	大阪大学, 2001, 博士論文
Version Type	VoR
URL	https://doi.org/10.11501/3183829
rights	
Note	

Amorphization and creation of lattice defects
in crystalline Si
by electron irradiation at low temperature

Jun Yamasaki

Department of Physics

ABSTRACT

We have studied the effect of electron irradiation in crystalline silicon at low temperature. By means of transmission electron microscopy and associated experimental techniques, we have found new phenomena at the atomic level.

Firstly, we described the finding of amorphization which is induced in crystalline silicon under MeV electron irradiation. This finding is surprising, since it was believed for many years that electron irradiation never amorphizes crystalline silicon. From the investigation into the dose of electrons needed for amorphization with the various irradiation energies (0.2, 0.3, 1, 1.5, 2, 2.5, 3 MeV) and at various temperatures (25, 55, 75, 95, 115 K), we clarified that the irradiation by electron with energy of above about 1.5 MeV below 100K was needed for the amorphization. From the results, we conclude that amorphization in silicon by charged particle irradiation is caused by accumulation of not point defects but small cascade damages. Analyzing the change in the intensity of halo rings with irradiation energy and dose precisely, we clarified that the smallest cascade which contributes to amorphization included about only four atoms. This leads us into proposing a new mechanism of amorphization , which has remained unclear for the past two decades ; four interstitial atoms form the quasi-stable structure in crystalline silicon and it becomes an amorphous embryo. By means of electron-energy-filtered diffraction, electron energy loss spectroscopy, and *in-situ* observation at elevated temperatures, we clarified the atomic structure, the electronic structure, and the thermal stability of amorphous silicon by the new amorphization technique. The short range atomic structure and the electronic state in the conduction band is almost the same as that of amorphous silicon created by other existing techniques. However, unlike amorphous silicon introduced by ion implantation, amorphous silicon by electron irradiation is converted to polycrystals at 550℃.

Secondary, we found that numerous tiny defects are introduced by electron irradiation at low temperatures (4.2 - 100 K), by means of *in-situ* high resolution

transmission electron microscopy (HRTEM). Analyzing defect creation, post-irradiation HRTEM images, weak beam TEM images, *in-situ* observation of annealing, and image simulation, we conclude that the nature of the defects are voids as the result of athermal (not thermal) migration of lattice vacancies under electron irradiation even at the lower temperatures. We succeeded in finding the athermal diffusion of lattice vacancies at atomic level and in real time for the first time.

From these experimental results and analyses, we reach a generalized view about the behavior of point defects in crystalline silicon in low temperature under electron irradiation. We conclude that lattice vacancies can migrate and the agglomeration of them results in void defects. On the other hand, self interstitials contribute to the amorphization whenever higher energy is transferred to them.

Finally, we mention the application of the new amorphization technique to fabricating fine structure in silicon, such as the production of two dimensional photonic crystals, since an electron beam can be focused on an area smaller than 0.2 μ m in diameter, can be scanned and can penetrate about 0.5 μ m into crystalline silicon.

CONTENTS

IV. DEFECTS IN CRYSTALLINE SILICON INDUCED BY ELECTRON IRRADIATION AT LOW TEMPERATURE

V. APPLICATION OF THE NEW AMORPHIZATION TECHNIQUE

I. INTRODUCTION

I-1. General introduction

It is usually known that silicon forms covalent crystal as the thermal equilibrium in the ordinary condition. However, much less knowledge has been accumulated about excited states, which are driven from the thermal equilibrium. The elementary excitation in the atomic system is the creation of a Frenkel defect which is a pair of a lattice vacancy and a self interstitial atom. Nevertheless, the states much more deviated from the thermal equilibrium are not trivial. In fact, dynamic motions of covalent-bonded silicon atoms involving point defects have not entirely been revealed in the excited states. One of interesting issues is the behavior of point defects under electron irradiation at low temperature, which are in no way generated and moved thermally. The defects were so far studied by electron paramagnetic resonance (EPR) and electronic measurements. In addition to the analysis of the atomic and electronic structures of the defects, it was shown that self-interstitials were moveable under electron irradiation even at 4.2K [I-1]. At the low temperatures, electronic excitations induced by electron irradiation play an important role in dynamic natures in the atomic system. Attempts have therefore been made to pursue the behavior of point defects in real space at the low temperature utilizing transmission electron microscopy (TEM) [I-2, I-3]. Nevertheless, a lack of the stability of cryo-TEM has prevented us from observing the phenomena at high magnification.

It is usually thought that TEM cannot contribute significantly the study of point defects. In fact, individual point defects have not yet been clearly revealed by TEM. However, TEM studies may bring the reliable atomic data about the clusters of point defects. In addition, TEM observation has occasionally led us into finding novel phenomena involving point defects under electron irradiation. With the background,

1

we have re-examined the electron-irradiation-effects in Si at low temperature by advanced cryo-TEM. In this study, structural transformation, namely, amorphization and the generation of defects are realized in crystalline silicon. This thesis is therefore organized as follows. After introducing amorphous and defects in silicon, the previous studies of the electron irradiation effects and transmission electron microscopy in silicon are briefly reviewed in this section. The experimental techniques are summarized in section II. Then, we describe the amorphization induced by electron irradiation in section III. This finding of amorphization is surprising, since it was believed for many years that electron irradiation never amorphizes crystalline silicon. Furthermore, analyzing the process of amorphization precisely by means of TEM and associated techniques, we propose a new atomistic mechanism of amorphization, which has been under debate for many years. Next, we describe the identification of the nature of small defects introduced by electron irradiation at low temperatures in section IV based on these experimental results and the analyses of them. We obtain a generalized view about the behavior of point defects in crystalline silicon in low temperature under electron irradiation.

I-2. Amorphous Si

I-2-1 The features of amorphous silicon

Amorphous material is a solid which possesses no translation or rotation symmetry on its atomic structure. Unlike similar solids called glassy materials, which are usually obtained by super-cooling a melt [I-4], amorphous materials are created by various catastrophic procedures such as vacuum evaporation [I-5] on a cold substrate, sputtering [I-6], and chemical vapor deposition (CVD)[I-7] etc. as summarized in Table.I-1. Amorphous silicon (a-Si) and related semiconductors can usually be fabricated by

vacuum deposition [I-5], and metallic amorphous alloys can be usually produced by splat cooling [I-8].

One of important questions in the field of solid state physics is the atomic and electronic properties of amorphous materials, in which the periodic boundary condition is no longer imposed. Generally, though the atomic structure of a-Si has the short range order (SRO) within the second nearest neighbor distance, there is no long range correlations between atoms the distance away, since the third peak disappear in radial distribution function[I-9]. Structure models for a-Si usually assume no dangling bonds. The model is called continuous random network (CRN) model [I-10]. The CRN model created in computer reproduces experimental RDF well and includes 5 and 7 membered atomic ring structures [I-11,12] in spite that crystalline Si includes only 6 membered atomic ring structure. In amorphous semiconductors, the band gap exists [I-13] caused by the short range order of their atomic structures in which most of atoms are four-coordinated as in crystals. However, unlike crystalline Si, local changes of SRO, such as a nearest neighbor distance of atoms and a bonding angle make some tails of localized electronic states in both valence and conduction bands [I-14]. The localized band tails influence various characteristic of amorphous semiconductors, for example, electric conductivity and light absorption. At finite temperatures, electrical conduction is brought by not only usual transport of unlocalized conduction band electrons but also thermally activated hopping of electrons between the localized states [I-15]. In a spectrum of optical absorption, the feature of light absorption caused by transition between the localized tail states and an allowed band appears near the absorption edge [I-16]. In addition to the existence of the localized band tails, localized states in the band gap are formed by structural defects [I-17] such as three-fold coordinated atoms with dangling bonds and five-fold coordinated atoms.

I-2-2 Amorphization in Si

Through various thermally non equilibrium processes, such as splat cooling, crystalline materials occasionally undergo amorphization. Silicon melt behaves metallic and a amorphous silicon does semiconductors as well as crystalline silicon (c-Si). This indicates that semiconducting a-Si can never be produced by splat cooling from melt unlike various metallic amorphous alloys. In addition to supercooling, various amorphization such as surface scratch [I-18], indentation[I-19], and ion implantation[I-20] are known as summarized in Table.I-2. Among such catastrophic processes which lead crystalline silicon to amorphous silicon, the bombardment of charged particles can gradually modify a single Si crystal to amorphous silicon with increasing doses of particle. Over 30 years ago, a classic phenomenological model for amorphization in Si by F.F. Morehead, et al [I-25] is proposed. In the model, amorphization occurs in the cylindrical region around each ion path. Then, sufficient overlap of the amorphized cylindrical cascades lead to amorphization in bulk region. This amorphization mechanism model is called ' heterogeneous amorphization '. On the other hand, another model called ' homogeneous amorphization ' was proposed in about 10 years ago by O.W. Holland, et al[I-26]. In the model, amorphization is a phase transition induced by the accumulation of a sufficient number of defects in crystalline Si. Both models are illustrated schematically in Fig.I-1. Despite the extensive works, the mechanism of amorphization in silicon has remained unclear at the atomic level so far.

More recently, the elementary process of amorphization is discussed in atomic scale. Since, as mentioned in section I-2-1, a-Si probably contains odd-membered atom ring such as 5- and 7-membered rings, it is considered that the defect structure which contains odd-membered atom rings leads to amorphization. As such a defect structure which may be amorphous embryo, a self-interstitial with the Jackson configuration [I-27] is proposed[I-28].

4

However, self-interstitials are moveable even at the amorphization temperatures [I-29] and can't exist stably. A pair of a di-interstitial (two interstitials) and a divacancy (two vacancies) were also examined as amorphous embryo by molecular dynamics simulation [I-30]. However, they were assumed by a somewhat artificial manner in the simulation and have not been identified by experiments directly. In order to clarify the mechanism of amorphization, it is necessary to determine experimentally the number of atoms which are responsible for the elementary process of amorphization.

I-2-3   Finding of amorphization in Si by electron irradiation

The amorphization of materials induced by ion implantation was found about 40 years ago [I-31]. Amorphization in various metallic compounds was extensively studied for last a few decades [I-32]. Later, it was realized that electron irradiation renders intermetallic compound into amorphous [I-33]. As electron irradiation never changes the chemical composition of target materials unlike ions or neutrons, the basic study of the amorphization of various compounds utilize electron irradiation, since then. It was clarified that whenever a certain composition can be amorphized by electron irradiation, then amorphous can be formed by quenching of the liquid phase of the same composition. This shows that the manifold of coordinations, that is, the ease of site exchange among constitute atoms is the most important parameter for amophization of compounds. However, the amorphization caused by such site exchange can not occur in single element materials such as Si. The amorphization induced by electron irradiation had been known in only one single element material, Se. In a previous attempt [I-3], it was reported that 1 MeV electron irradiation at a dose of 3×10^{23} failed to amorphize c-Si. Therefore, amorphization in Si by charged particle has not been well understood from a basic point of view.

The difference between ion implantation and electron irradiation is summarized as follows. The energy of ions is usually between several ten keV and several MeV, since an ion with the energy lower than several ten keV stops near the entrance surface of a target material and amorphizes the very thin layer about a few nano meters just beneath the surface. This amorphization is certainly affected by the initial surface conditions and therefore is not bulk amorphization. When an incident ion transfers a kinetic energy of the order of keV(10^3eV) or MeV (10^6eV) to a target Si atom, a large collision-cascade-damage, which is started with the firstly displaced Si atom is produced. The cascade damage contains more than several hundred of displaced atoms. Not only such large cascade damages but also point defects and small cascade damages which contain only several displaced atoms are introduced together by energetic ions with the kinetic energies in a target material. Consequently, it is difficult to clear experimentally which is essential process for amorphization, the creation of cascade damages or point defects creation. This is the reason why the mechanism of amorphization in Si induced by ion implantation has been unclear. Whereas, since the mass of an electron is much smaller than that of an ion, from the conservation law of energy and momentum, an incident electron can transfer only a part of energy to a target atom. For example, an incident electron having an energy of 2 MeV can transfer the energy from 0 to 460 eV. Hence, by means of the irradiation of electron which have the energy between a few hundred keV and a few MeV, we can intensionally introduce only point defects or small cascades of only several displaced atoms as well as point defects. However, because it had been considered that electron irradiation fails to amorphize crystalline Si as mentioned above, so the studies of amorphization mechanism by means of electron irradiation has never been performed in Si.

I-3 Defects in Si crystal

It is well known that point defects exist in both equilibrium and non-equilibrium states in semiconducting crystals. They have been particularly studied since the usefulness of the material is derived by the defects. In addition to the simple point defects which are substitutional doped atoms, atomic structures of point-defect- complexes, often involving impurities atoms, have been no doubt clarified by electron paramagnetic resonance (EPR) [I-1,34,35,36]. A few kinds of vacancy clusters, V2, V3 etc.. can recently be identified by positron annihilation spectroscopy (PAS) [I-37]. We summarized the known features of point defects and point-defect-complexes in Si in Table.I-3 and I-4. However, atomic structures of various point-defect-clusters have been under debate, even though their electronic energy levels and/or vibrational frequencies are precisely determined by a variety of spectroscopic techniques, i.e. deep level transient spectroscopy (DLTS) , photo-luminescence spectroscopy (PL) etc.. In particular, clusters involving self-interstitials have been much less clarified since they are unlikely to exhibit energy levels inside the band gap [I-62]. Recent study about the Si device processing via ion implantation show that self interstitial atoms and their clusters play an important role in the electronic property of final devices even though they are electronically and optically inactive[I-63].

I-4 Interaction of fast electrons with a solid

When electrons enter a material, they interact with the constituent atoms via Coulomb forces. As a result of these forces, some electrons are scattered. The direction of their momentum is changed and in many cases they transfer an appreciable amount of energy to the specimen. The energy transfer from incident electrons to a material is due to the interaction with lattice system and with electronic systems.

I-4-1 Energy transfer to lattice system

Elastic scattering is essentially Coulomb interaction with an atomic nucleus. The majority of electrons travel further from the center of an atom, where the nuclear field is weaker as a result of the inverse-square law and the fact that the nucleus is partially screened by the atomic electrons. Most incident electrons are therefore scattered through smaller angles, typically a few degrees in the case of a few hundred keV incident energy. They lose a few eV via Coulomb interaction with atomic nucleus and result to induce phonon excitation. Because the energy they lose is negligible as compared with their total kinetic energy which is more than several tens keV, their scattering process is called as elastic scattering. Whereas, only part of incident electrons which approach closely to atomic nucleus can be deflected through a large angle. Such high-angle scattering is referred to as Rutherford scattering. Fig.1-4(a) shows a collision between an electron of mass m_0 and energy E with an atom of mass M. The scattering angle is θ. The energy transferred to the atom is given by

$$E_{trans} = \frac{2E}{Mc^2}(E + 2m_0c^2)\sin^2\frac{\theta}{2} \qquad (I\text{-}1)$$

, in which c represents the light velocity. The maximum energy E_{max} is transferred when $\theta = \theta_{max} = \pi$, and thus

$$E_{max} = \frac{2E}{Mc^2}(E + 2m_0c^2). \qquad (I\text{-}2)$$

A displacement damage occurs when the energy transferred to an atom is larger than the displacement threshold energy, E_d.

Electrons accelerated by a high voltage in the order of kV are relativistic and the scattering of an electron by a nucleus of an atom necessitates a quantum treatment. The exact calculation of the displacement cross section σ, derived by Mott [I-64,65], can be approximated by McKinley-Feshbach's formula [I-66] for the case of atoms whose atomic number is not too larger. The formula is written as

$$\sigma = \pi \left[\frac{Ze^2\gamma}{m_0c^2(\gamma^2-1)} \right]^2 \left[\frac{E_{max}}{E_d} - \frac{\gamma^2-1}{\gamma^2} \right] \ln \frac{E_{max}}{E_d}$$
$$+ \alpha\pi Z \sqrt{\frac{\gamma^2-1}{\gamma^2}} \left(2\sqrt{\frac{E_{max}}{E_d}} - 2 - \ln \frac{E_{max}}{E_d} \right)$$

(I-3)

where Z is atomic number of the atom, α (= 1/137) is the fine structure constant, and

$$\gamma = \sqrt{1 - \frac{v^2}{c^2}},$$

(1-4)

in which v is the velocity of the incident electron. In other words E_d is the minimum transfer energy for creation of a Frenkel pair. It is rewritten as

$$E_d = \frac{2E_{th}}{Mc^2} \left(E_{th} + 2m_0c^2 \right)$$

(1-5),

in which E_{th} represents the threshold electron energy for displacement damage. Fig.1-4(b) shows the cross section σ of the displacement as a function of incident electron energy calculated with Eq. (1-3), in which the E_d=15 eV(E_{th}=160keV) for Si was assumed.

I-4-2 Energy transfer to electronic system

High-angle collisions are comparatively rare, the major part of inelastic scattering

9

occurs as a result of Coulomb interaction between a fast incident electron and the atomic electrons surrounding each nucleus. Some inelastic processes can be understood in terms of the excitation of a single atomic electron into a Bohr orbital of higher quantum number or, in terms of energy-band theory, to a higher energy level.

The ground-state energy of an inner-shell electron lies typically some hundreds or thousands of eV below the Fermi level of the solid. Consequently, in order to excite the inner-shell electron into unoccupied states above the Fermi level, the fast electron must lose an amount of energy greater than the original binding energy of inner-shell electrons.

Outer-shell electrons can also undergo single-electron excitation. In an insulator or semiconductor, a valence electron makes an interband transition across the energy gap. In the case of a metal, a conduction electron makes a transition to a higher state, possibly within the same energy band. The fast electron supplies the energy needed for excitation of an outer-shell electron into unoccupied conduction band.

As a different excitation mode from the single-electron mode, a plasma resonance which is an oscillation of the valence-electron density is known. According to quantum theory, the excitation can also be described in terms of the creation of a pseudoparticle, the plasmon. The plasmon excitation energy, which equals to the energy the fast electron loses, is given by $E_p = \hbar\omega_p$, $\hbar$ being Planck's constant and ω_p being the plasma frequency which is proportional to the square root of the valence-electron density.

I-5 *In-situ* transmission electron microscopy of electron-irradiation-effects in Si

In basic studies of point defects, electron irradiation has been preferably utilized [I-1,34,35,36,62,67]. Among various excitations induced by electron irradiation such as plasmon, core electron excitations, displacement damage is a well known excitation to create point defects. Incident electrons of the correct energy give rise to the primary point defect as describe in section I-4. For instance, E_d is estimated in Si by electronic measurement to be about 160keV. When we need complex defect such as a small cascade damage, then a higher voltage electron microscope (a 2MV microscope, for instance) is needed. Transmission electron microscopy has so far contributed mainly to studies of extended defects in semiconductors. Various types of the extended defects, i.e. dislocations [I-68,69,70,71], stacking fault tetrahedra [I-72], interfaces between two different semiconducting crystals [I-73, 74, 75], and grain boundaries [I-76, 77] have been examined in detail . They are to some extent similar to those in other materials such as metallic alloys, but characteristic in many cases; they exhibit the bond topology which is governed by the general nature of covalent bonding and occasionally different from the parent diamond lattice. Point defects and their clusters including impurities such as dopant atoms, hydrogen, carbon, oxygen and metallic impurities may affect the nucleation and growth of extended defects, and hence its mechanism has been paid attention to from both scientific and technological points of view toward controlling the extended defects. *In-situ* TEM has revealed the nucleation, the growth and the occasional disappearance of extended defects in Si in the wide temperature range from 20 K to over 1000°C [I-78,79], thus demonstrating its capability of observing not only the static atomic arrangements but the dynamic nature of constituent atoms covalently interacted involving point defects in Si. Nevertheless, the structure analysis of small defects by HRTEM has been a puzzling task, which has prevented us from understanding the dynamic nature at the atomic level in particular at low temperatures.

In a TEM incident electrons therefore may have two rolls; some transfer their

11

energy to create the Frenkel pairs and other kinds of complex defects by the atomic displacement via elastic electron scattering and others undergo small angle scattering and form TEM images through conventional electron optics. Hence, the technique is a unique means to introduce primary defects and others selectively in a thin foil and pursue interaction of them by imaging at the atomic level.

II. EXPERIMENTAL

In this chapter, we explain the experimental methods used in this research. Fig.II-1 shows the procedure of the experiments. The instruments used in this study are summarized in Table.II-1.

II-1 Specimen preparation

A Czochralski(CZ)-grown, P-doped Si{110} wafer with resistivities between 1 and 10 Ω-cm was used in this study. The single crystalline wedge-shaped samples were prepared by two different techniques shown in Fig.II-2 : (1) A disk of 3 mm in diameter was taken from a wafer using an ultrasonic drill. The center of the disk was mechanically thinned using a dimpling machine, and then thinned by chemical etching in a solution of HNO_3 and HF. (2) a Si wafer was cleaved on {110} and {111} planes and set on a mesh. The surfaces of the samples prepared in the way (2) are covered with only natural oxidized layer about 2 or 3 nm in thickness, and hence the influence of surface to the electron-irradiation phenomena, such as recoil implantation of impurity from the electron entrance surface, is mostly cut down.

II-2 Electron irradiation

Electron irradiations were performed using TEMs equipped with liquid He cooling stages. As shown in Table.II-2, Hitachi H-3000 (Fig.II-2), JEM-3000HFI (Fig.II-3), and JEM2000EX were used for electron irradiation with the energies more than 1 MeV, of 0.3 MeV, and of 0.2 MeV, respectively. The electron beam was set parallel to the <110> zone axis. Irradiation was usually done with a most condensed electron beam

13

and its diameter on a specimen surface was about 1 μ m. The electron beam of TEM has a Gaussian flux distribution expressed by $I(r) = I_0 \exp(-(r/r_0)^2)$ along the radial distance r from the beam center. Using a Faraday cage, we measured the electron flux on the central area 300 nm in diameter of the beam, i.e. on the highest flux area.

II-3 Observation of atomic structures by means of transmission electron microscopy (TEM)

The process of amorphization and defect creation induced by electron irradiation is observed *in-situ* in TEMs. The image contrast in TEM is usually produced in two different ways, i.e. diffraction contrast and phase contrast. The former has been utilized most commonly to observe substructure of materials such as defects, greatly contributing to the field of material science, and the latter has recently achieved rapid development as high-resolution electron microscopy in observing atomic structure directly.

We performed *in-situ* observation of amorphization process and defect creation by means of diffraction contrast and selected area diffraction, since it is difficult to take a good HRTEM image at low temperature. Therefore, the post-irradiation HRTEM observation of the interface between the amorphized area and crystalline area were performed at room temperature in a JEM-2010. Whereas, as the exception, *in-situ* observation of 0.3 MeV irradiation was done by means of HRTEM using JEM-3000HFI equipped with a top-entry type liquid-helium cooling stage and the field emission gun. In the following, we explain of diffraction contrast imaging and HRTEM.

II-3-1 Diffraction contrast

Fig.II-5 illustrates the mechanism of production of contrast on transmission electron micrograph. The almost parallel illuminating beam of electrons is scattered by the specimen. In crystalline materials, this scattering takes the form of one or more Bragg diffracted beams traveling at small angles (1 or 2 degrees) with the incident beam, which are focused by the objective lens to form a transmission diffraction pattern in its back focal plane. An aperture is inserted to the back focal plane as shown in Fig.II-5(a). This aperture does not allow Bragg reflections to pass through to the final image, which is therefore formed by the direct beam and any low angle inelastic scattering. This type of image is called a bright field image. The contrast is therefore produced by differences in intensities of electrons scattered into Bragg reflections from various parts of the thin specimen and is consequently called 'diffraction contrast'.

Images can be formed by any one diffracted beam by tilting the illumination so that the required beam passes down the axis of the objective lens. The resulting image is known as a dark field image(Fig.II-5(b)). When some defects exist in a specimen, the contrast arises from local changes in diffracting conditions caused by the defect strain field. This is the most common imaging mechanism used in defects studies. A weak-beam dark-field image is formed in a "weak" reflection with large deviation parameter $\left| s_g \right|$. Here, S_g is the vector connecting reciprocal lattice point g and Ewald sphere shown in Fig.II-6 and called excitation error vector. The contrast in this case arises from regions of large lattice strain close to the cores of defects. Far away from defects the foil is tilted well away from the Bragg condition and so the image intensity is very low. However, in regions close to defects, the local strain-field may bend the reflecting planes back towards the Bragg condition, resulting in a local image peak of high relative (but low absolute) intensity.

It is usually considered that true weak beam conditions are obtained when the value of the deviation parameter $\left| s_g \right|$ is in the order of 10^{-1} nm^{-1} [II-1]. The appropriate

15

diffraction condition can be set up by reference to Kikuchi lines in a diffraction pattern. Suppose the foil is tilted such that the Ewald sphere cuts the line of systematic reflections at the point ng. The value of "n" is immediately apparent from the Kikuchi pattern. If n is integral then the bright excess Kikuchi line corresponding to the reflection ng will pass directly through the diffraction spot ng. Figure 2-E represents the case of $n = 3$. $|s_g|$ can be calculated from the formula

$$s_g = \frac{(n-1)g^2}{2k},$$ (II-1)

where $g = 1/d_{hkl}$ is the magnitude of the reciprocal lattice vector corresponding to the planes (hkl) with interplanar spacing d_{hkl}; $k = 1/\lambda$ is the radius of the Ewald sphere, where λ is the electron wavelength; and the "reflection" ng is satisfied in the sense explained above.

II-3-2 High-resolution electron microscopy

Suppose the aperture allows the transmitted plus one diffracted beam to reach the image (Fig.II-5(c)). Assuming the contribution of the transmitted and diffracted beam at the position x_i on the image plane as $\Phi_0(x_i)$ and $\Phi_g(x_i)$, respectively, the total wave function, $\Phi(x_i)$, is expressed as follows:

$$\Phi(x_i) = \Phi_0(x_i) + \Phi_g(x_i)$$ (II-2)

Thus the intensity on the image plane is

$$\begin{aligned}I(x_i) &= \Phi(x_i) \cdot \Phi^*(x_i) \\ &= I_0(x_i) + I_g(x_i) + 2\operatorname{Re}\left[\Phi_0(x_i) \cdot \Phi_g^*(x_i)\right]\end{aligned}$$ (II-3)

16

where $I_0(x_i) = |\Phi_0(x_i)|^2$, $I_g(x_i) = |\Phi_g(x_i)|^2$, and Re[] means taking the real part in the bracket. If the incident wave is assumed to have unit amplitude and the specimen thickness is small,

$$I(x_i) \cong 1 + 2\,\text{Re}[\Phi_g(x_i)] \qquad \text{(II-4)}$$

because $\Phi_0 \cong I_0 \cong 1 \gg I_g$. The image contrast is therefore determined by the second term (interference term) of the above equation. Since the term $\Phi_g(x_i)$ depends on the phase change of the incident wave in the specimen, the contrast is called ' phase contrast'. The intensity of phase contrast is proportional to the diffraction amplitude and suitable for obtaining the image of small objects such as an atom and fine particles accordingly. If the aperture allows two dimensional array of diffracted beams to pass through to the image plane, two dimensional structure of the specimen is to be reproduced, which is the fundamental principles of high-resolution electron microscopy.

II-3-3 Simulation of HRTEM images

In order to discuss the atomic structures on the basis of HRTEM images, experimental images should be compared with theoretically calculated images under adequate imaging conditions. For this purpose, computer programs based on the multislice method [II-2, 3] are used. In this method the crystal is divided into n-slices along the incident electron beam direction:

$$t = n \cdot \Delta t \qquad \text{(II-5)}$$

where t is the crystal thickness and Δt the slice thickness. Each slice is assumed to consist of vacuum space with a thickness of Δt and to represent a phase object. The electron beam is assumed to propagate in the vacuum in the way described by the small angle approximation of Fresnel diffraction theory and to transmit the two-dimensional phase object.

The general computational process of this calculation method is described in detail [II-4]. In order to explain the method we take, a simple case in which the incident-electron-beam-direction is parallel to [001] is explained here.

First the structure factors $F(hk0)$ are calculated as

$$F(hk0) = \sum_j f_j \exp[2\pi i(h_{xj} + k_{yj})] \qquad \text{(II-6)}$$

here f_j is an atomic form factor for electrons of the j-th atom. The average potential along z-axis is

$$V(x,y) = \frac{1}{V} \sum_{h,k} F(hk0) \exp[2\pi i(h_x + h_y)] \qquad \text{(II-7)}$$

where V is the unit cell volume. The transmission function of the phase object $q(x,y)$ is

$$q(x,y) = \exp\{-i\sigma V(x,y) \cdot \Delta t\} \qquad \text{(II-8)}$$

where σ is an interaction constant.

The propagation of the electron beam through the vacuum is described as follows based on the small angle Fresnel scattering theory (λ: wave length).

$$p(x,y) = \frac{i}{\Delta t \cdot \lambda} \exp\left\{-i \frac{x^2 + y^2}{2\lambda \cdot \Delta t}\right\} \qquad \text{(II-9)}$$

18

Using these functions, the wave at the rear surface of the (n+1)-th phase object $\psi_{n+1}(x,y)$ is

$$\psi_{n+1}(x,y) = q_{n+1}(x,y) \cdot \{\psi_n(h,k) * P_{n+1}(h,k)\} \qquad \text{(II-10)}$$

where the star symbol denotes the convolution integral.

The Fourier transformation of Eq.(II-10) is

$$\Psi_{n+1}(h,k) = Q_{n+1}(h,k) * \{\Psi_n(h,k) \cdot P_{n+1}(h,k)\} \qquad \text{(II-11)}$$

Functions with capital letters mean Fourier transformed functions,

$$P(h,k) = \exp\left[-2\pi i \cdot \Delta t \frac{\lambda}{2}\left\{\left(\frac{h}{a}\right)^2 + \left(\frac{k}{b}\right)^2\right\}\right] \qquad \text{(II-12)}$$

in which a and b are unit cell parameters in the image plane. The resulting $\Psi_{n+1}(h,k)$ is used as output and/or input data for the next slice.

The resulting reflections $\Psi(h,k)$ are inverted into an image through the lens system. The effect of lens system is summarized in a function $T(h,k)$, which can be described in a form as follows :

$$T(u) = A(u)E(u)\exp\{-i\chi(u)\} \qquad \text{(II-13)}$$

Here the sign ' u ' is used instead of h and k. The function $A(u)$ is an aperture function, and

$$\chi(u) = \frac{\pi}{2}\left(C_S\lambda^3 u^4 + 2\lambda u^2 \Delta f\right) \qquad \text{(II-14)}$$

19

whose value is changed by defocus Δf, the spherical aberration C_S. The function $E(u)$ means attenuation of the wave and the exact mathematical form of $E(u)$ is complex. In general, $E(u)$ is expressed by multiplication of E_c and E_a. E_c means the influence of the chromatic aberration and be expressed as

$$E_c = \exp\left[-(\pi\lambda\delta)^2 u^4/2\right] \qquad \text{(II-15)},$$

where δ is the defocus spread due to the chromatic aberration. E_a means the influence of non-parallelity of incident wave and be expressed as

$$E_a = \exp\left[-\left(\pi\alpha/\lambda\right)^2\left(C_S\lambda^3 u^3 + \lambda u\Delta f\right)^2\right] \qquad \text{(II-16)},$$

where α is the semiangle of incident beam.

If the specimen is very thin, it is approximated that $\psi(x,y) = 1 + i\sigma V_p$. Here, $\sigma = \pi/\lambda V$ and V_p is projection of potential in crystals. This is called ' Weak Phase Object Approximation'. By applying a Fourier transformation on $T(h,k)\Psi(h,k)$, a wave $\psi(x,y)$ and an image $I(x,y)$ in real space are obtained.

$$\psi(x,y) = F[T(h,k)\Psi(h,k)] \qquad \text{(II-17)}$$

$$I(x,y) = |\psi(x,y)|^2 \qquad \text{(II-18)}$$

By applying Weak Phase Object Approximation,

$$I(x,y) = 1 - 2\sigma\Delta t \cdot F[V_u E(u)\sin\chi(u)] \qquad \text{(II-19)}$$

Here, the sign F[ ] means Fourier transform and V_u is $F[V_p]$. Because the image

contrast depends on $\sin\chi(u)$, $\sin\chi(u)$ is called ' Contrast Transfer Function'. The procedure of HRTEM image analysis based on above formulation is summarized in Fig.II-7.

II-3-4 Stereoscopic observation

The spatial distributions of the formed defects in a specimen foil were investigated by means of stereomicroscopy. In this technique, two micrographs of the same area of the specimen where the defects to be investigated exist are taken from two different directions by using a tilting specimen stage while keeping the reflection condition being almost the same so that every defect is visible in the two micrographs with the same contrast. The depth difference between two defects, z, is related to the parallax difference,p, and the angle of tilt between the two photographs, θ , as follows:

$$z = p/(2M_a\sin(\theta/2))\qquad\text{(II-20)}$$

where M_a is the magnification of the micrographs. Thus, the depth distribution of defects can be determined by measuring the parallax difference of the defect on the two micrographs.

II-4 Analysis of amorphous structures by means of Radial Distribution Function (RDF)

II-4-1. RDF [II-5]

The electron, X-ray and neutron diffraction pattern of an amorphous material consists several broad diffuse rings. The pattern is different from the diffraction pattern of powdered crystalline material which shows a large number of fairly sharp rings. In a simple monoatomic amorphous, the positions of the atoms show only a short range structure referred to an origin on any one atom. We expect to find the number of nearest-neighbor atoms as we find in a crystalline form of the material. From a typical diffraction pattern of amorphous, the only quantity which can be determined directly is the radial distribution function (RDF). This is obtained from a Fourier analysis of the experimental electron scattering curve, and gives directly the average number of atoms to be found at any distance from a given atom.

In the case of crystalline materials, the structure factor is given as

$$S_G = \sum_j f_j \exp(-i\mathbf{G} \cdot \mathbf{r}_j) \qquad \text{(II-21)}$$

with f_j the atomic form factor of atom for electron scattering. The sum runs over all atoms in the unit cell. Whereas, in amorphous materials, unit cell and reciprocal lattice can't be defined. Then, instead of writing it for the structure factor of the basis, we write the sum for all the atoms in the specimen. Further, instead of specializing the scattering to the reciprocal lattice vectors $\mathbf{G}$ characteristic of a crystal, we consider arbitrary scattering vectors $\Delta\mathbf{k} = \mathbf{k}' - \mathbf{k}$, where $\mathbf{k}$ and $\mathbf{k}'$ is the wave vector of incident and scattered electron, respectively.

Therefore the scattered amplitude from an amorphous material is described by

$$S(\Delta\mathbf{k}) = \sum_m f_m \exp(-i\Delta\mathbf{k} \cdot \mathbf{r}_m) \qquad \text{(II-22)}$$

The sum runs over all atoms in the specimen. If α denotes the angle between $\Delta\mathbf{k}$ and

22

$\mathbf{r}_m - \mathbf{r}_n$, then the scattered intensity at scattering vector $\Delta\mathbf{k}$ is given by

$$I = S^*S = \sum_m \sum_n f_m f_n \exp[i\Delta\mathbf{k} \cdot (\mathbf{r}_m - \mathbf{r}_n)]$$
$$= \sum_m \sum_n f_m f_n \exp(iKr_{mn}\cos\alpha) \qquad \text{(II-23)}$$

where K is the magnitude of $\Delta\mathbf{k}$ and r_{mn} is the magnitude of $\mathbf{r}_m - \mathbf{r}_n$.

In an amorphous specimen the vector $\mathbf{r}_m - \mathbf{r}_n$ may take on all orientations, so we average the phase factor over a sphere:

$$I = \sum_m \sum_n \frac{f_m f_n \sin Kr_{mn}}{Kr_{mn}} \qquad \text{(II-24)}$$

For atoms of only one type, we let $f_m = f_n = f$ and separate out from the summation (II-24) the terms with $n = m$. For a specimen of N atoms,

$$I = Nf^2[1 + \sum_{m,n(m\neq n)} \frac{\sin Kr_{mn}}{Kr_{mn}}]$$
$$= Nf^2\left\{1 + \int_0^R 4\pi r^2[\rho(r) - \rho_0]\frac{\sin Kr}{Kr}dr + \frac{\rho_0}{K}\int_0^R 4\pi r\sin Krdr\right\} \qquad \text{(II-25)},$$

where $\rho(r)$ is the concentration of atoms at distance r from a reference atom and ρ_0 is the average concentration. Because R is the very large radius of the specimen, the second integral in (II-25) may be neglected except in the forward region of very small angles. Then (II-25) is changed to

$$\frac{I(K)}{Nf^2(K)} - 1 = \int_0^R 4\pi r^2[\rho(r) - \rho_0]\frac{\sin Kr}{Kr}dr \qquad \text{(II-26)}$$

We must note that I and f are the function of K. In order to obtain the information in real space, we apply Fourier transformation to (II-26)

$$4\pi r^2 \rho(r) = 4\pi r^2 \rho_0 + \frac{2r}{\pi} \int_0^\infty \left(\frac{I(K)}{Nf^2(K)} - 1 \right) \cdot K \sin Kr dK \qquad \text{(II-27)}$$

$4\pi r^2 \rho(r)$ is referred as RDF (Radial Distribution Function).

II-4-2 Instrument used in experiments

In order to obtain a precise RDF, it is important to remove the background intensities due to inelastically scattered electrons. We removed electrons losing energy more than 8eV using the electron energy filter. Because the plasmon energies of both c-Si and a-Si (mentioned later) are about 16-17 eV, the background due to plasmon excitation which is major part of inelastic scattering was cut off. The experiments were performed in JEM2010FEF(Fig.II-8) equipped with the omega type energy filter shown in Fig.II-9 [II-6,7]. The omega filter is the magnetic device to obtain TEM images and diffraction patterns in which inelastic scattered electrons are reduced. Fig.II-9(b) is the schematic diagram of the path of incident electrons from a position D1. As the result of energy dispersion within four magnetic prism, an energy loss spectrum is formed at a position D2. By inserting an energy-selection slit in plane D2, energy loss electrons can be cut.

We measured the radial profile of diffraction patterns from irradiated areas, i.e. partially and fully amorphized areas. Then, we measured the intensity of the first halo ring from the profiles. Fig.II-10 shows a typical example of measurement. (a) and (b) are the diffraction data without and with the energy filter, respectively. In the profile of (b), inelastic background is almost cut down. Because all of our measurements were performed using the energy filter, we can measure the intensity of halo rings precisely.

We recorded energy-filtered diffraction patterns on Imaging Plates (IP) [II-8] for precise analysis instead of negative films. IP is a good device for quantitative analysis

24

in TEM experiment, because they have good characteristics which are high sensitivity, wide dynamic range, good linearity to the electron dose. The IP is mainly made of phosphor doped with Eu^{2+}. When electrons incident the phosphor, electron-hole pairs are created. Created electrons are trapped at the defects inside crystal of phosphor and holes are trapped at Eu^{2+}. In order to read out the data of the energy of incident electrons stored like this, the phosphor is irradiated with visible light. This light excites the trapped electrons and electrons recombine with the holes. Its recombination energy is converted to photons of about 390 nm wavelength at Eu^{2+} and converted to electrical signals.

II-5 Analysis of electronic structures by means of Electron Energy-Loss Spectroscopy (EELS)

II-5-1 Electron energy-loss spectrum

In electron energy-loss spectroscopy (EELS), we study directly the primary processes of electron excitation, each of which results in a fast electron losing a characteristic amount of energy. The beam of transmitted electrons is directed into a high-resolution electron spectrometer which separates the electrons according to their kinetic energy and produces an electron energy-loss spectrum showing the scattered intensity as a function of the decrease in kinetic energy of the fast electron.

A typical loss spectrum, recorded from a thin Si film over a range of about 280 eV, is shown in Fig.II-11. Inelastic scattering caused from plasmon excitation is visible as a peak at 16-17 eV in the spectrum. The inner-shell intensity rise rapidly at 100 eV and then falling more slowly with increasing energy loss. They take the form of edges rather than peaks and called as ELNES (Energy Loss Near Edge Structure). The

energy-loss coordinate at the edge is approximately the binding energy of the corresponding L-shell. The form of ELNES and the peak position of plasmon reflect the elemental component and the crystallographic or energy-band structure of the specimen. If an element or compound occurs in different forms, quite distinct fine structures are produced.

When the change of incident electron wave vector, q is very small, transition probability from a state of principal quantum number n and angular momentum quantum number l to a state of n' and l' is in proportion to

$$q^2 |\langle n',l'|\mathbf{u}\cdot\mathbf{r}|n,l\rangle|^2 \cdot \delta(E_{n',l'} - E_{n,l} - E) \qquad \text{(II-28)}$$

, where u is the unit vector parallel to q, r is the position vector of incident electron, and E is the energy loss of incident electron. Consequently, only transition which the change of l is ± 1 is allowed. For example, ELNES due to the transition from L2 and L3 shell states to conduction band in crystalline Si reflect partial density of states of s-like and d-like state in the conduction band.

If the energy-loss spectrum is recorded from thicker samples, there is a probability that a transmitted electron will be inelastically scattered more than once. In the case of plasmon scattering, the result is a series of peaks at multiples of the plasmon energy. The multiple scattering peaks have appreciable intensity if the specimen thickness approaches or exceeds the mean free path of the inelastic scattering process, which is 115 nm [II-9] at 100 keV incident energy which we used in our experiments, respectively. These values are utilized for measuring the thickness of samples. The mean free path is the average distance between scattering events.

II-5-2 Instruments used in experiments

Electron energy loss spectroscopy (EELS) was performed on a JEM3000F operating at 300kV and equipped Gatan parallel EELS spectrometer in Osaka National Research Institute. An EELS spectrometer is installed beneath the camera system of a TEM. Schematic diagrams of the spectrometer optics are shown in Fig.II-12. From Fig.II-12 we can see that electrons are selected by an entrance aperture. The electrons pass through the spectrometer and are deflected about $90°$ by the surrounding magnetic field. Then, electrons with greater energy loss arrive in points on the dispersion plane further than the point zero where loss electrons arrive in. A spectrum is obtained from the array of the detectors in the dispersion plane.

III. AMORPHIZATION IN SILICON BY ELECTRON IRRADIATION

III-1 Introduction

The energy of ions is usually between several ten keV and several MeV, since an ion with the energy lower than several ten keV stops near the entrance surface of a target material and amorphizes the very thin layer about a few nano meters just beneath the surface. When an incident ion transfers a kinetic energy of the order of keV(10^3eV) or MeV (10^6eV) to a target Si atom, a large collision-cascade-damage, which contains more than several hundred of displaced atoms. Not only such large cascade damages but also point defects and small cascade damages which contain only several displaced atoms are introduced together by energetic ions with the kinetic energies in a target material. Consequently, it is difficult to clear experimentally which is essential process for amorphization, the creation of cascade damages or point defects creation. Whereas, since the mass of an electron is much smaller than that of an ion, from the conservation law of energy and momentum, an incident electron can transfer only a part of energy to a target atom. Hence, by means of the irradiation of electron which have the energy between a few hundred keV and a few MeV, we can intensionally introduce only point defects or small cascades of only several displaced atoms as well as point defects. For a long time, it had been considered that electron irradiation fails to amorphize crystalline Si. However, we found the amorphization by electron irradiation and performed the studies of amorphization mechanism in Si by means of electron irradiation.   As mentioned above, one of the fruits in this study is to have found amorphization in Si by electron irradiation and to have solved the mechanism of amorphization. To begin with,

28

we present *in-situ* observation of amorphization. Next, we summarize the conditions of amorphization. Then, we characterize amorphized area by various methods as summarized in Table.III-1. Finally, we propose a new mechanism based on the experiments.

III-2 *In-situ* Observations of Amorphization Process

It was found that *c*-Si films are converted to *a*-Si by MeV electron irradiation at low temperatures. Fig.III-1(d) shows a typical series of *in-situ* TEM observation of amorphization process. The electron irradiation energy is 2.0 MeV. All micrographs are bright field images from <110> zone axis. The center of irradiation area come to appear to be white with increase of irradiation dose in the temperatures below 94K. Then finally the area of approximately 300 nm in diameter change into uniformly white in the TEM images. The insets are the corresponding electron diffraction patterns, in which the selected area aperture covered the central area of about 250 nm in diameter. The halo rings appear in diffraction patterns and their intensities increase with irradiation time. Evidently, the irradiated areas are amorphized. Because of the lack of Bragg reflections, incident electrons almost straightly transmit the amorphous area much more than crystalline area. This is the reason that amorphous area appears to be brighter than surrounding crystalline area in bright field images. A careful look at Fig.III-1 shows that amorphized grains and crystalline grains coexist in the irradiated area at the intermediate stage of amorphization.

III-3 Experimental Conditions of Amorphization

In Fig.III-1, we compile *in-situ* TEM observation of 2 MeV electron irradiation at 25 K, 60 K, 94 K and room temperature. Comparing irradiation dose needed for amorphization below 94 K, we note that more irradiation dose are needed at higher temperature. At room temperature, the numerous {113} defects was observed in the irradiated area. Nevertheless, the crystallinity was retained at room temperature. On the other hand, Fig.III-2 shows a few series of *in-situ* TEM observation of electron irradiation with various energy at about 25K. The electron irradiation energies in each series are 2.0, 1.5, 1.0 and 0.2 MeV. Except for 0.2 MeV irradiation, irradiated areas convert to amorphous. A 0.2 MeV electron irradiation induces not the amorphization but a dislocation loop. Comparing irradiation dose needed for amorphization in each irradiation energy, we note that lower energy irradiation need more dose for amorphizing Si.

We compile the dependence of amorphization condition on temperature and irradiation energy in Fig.III-3. By interpolating experimental data shown by black dots in Fig.III-3, we obtained the curved boundary which separate the two kind of steady states under electron irradiation ; amorphized Si and crystalline Si with defects. Here, doses needed for amorphization mean the doses when the central area of approximately 300 nm in diameter turned white in bright field TEM images without any residual contrast due to fragmented *c*-Si. On the other hand, the doses below the curved surface mean the doses that they are insufficient for amorphization. Clearly, more doses are needed for amorphization in higher temperature and lower irradiation energy. It is clarified that the electron irradiation with above about 1.5 MeV below 100 K is needed for efficient amorphization with low irradiation dose of 10^{20}e/cm^2. It is usually thought that irradiation damages are recovered thermally. So, amorphization is prevented at

higher temperature, above 100 K.

The periphery area of an amorphized area receives lower dose, since an irradiation electron probe has the Gaussian like intensity profile. In the periphery, numerous small defects are introduced without distinct habit plane by irradiation at 25K (Fig.III-2(d)). We mention about the defects in chapter IV.

It is well known that when a Si crystal is irradiated by electrons, an incident electron with energy of more than 160 keV can produce a Frenkel-pair which is a pair of a self interstitial atom and a lattice vacancy. In addition, if a Si crystal is irradiated by electrons with energy of more than a few hundred keV, an atom, which is primarily knocked on by an incident electron, causes multiple recoil of surrounding atoms (collision cascade damage). As shown in Fig.III-3, with the irradiation energy getting lower than 1 MeV, it becomes steeply hard to amorphize Si. Consequently, it is considered that only accumulation of Frenkel pairs are not enough and collision cascade damages are needed for amorphization. In section III-7-1, we will discuss on the size of the smallest cascade which contributes to amorphization.

III-4 Atomic Structures

In order to characterize disordered atomic structures, RDF is used in general as in section II-4. Using RDF, we examined the difference between the atomic structure of *a*-Si produced by electron irradiation and that by other amorphization methods. Though RDF is usually obtained from X ray or neutron scattering, we utilize electron diffraction, since an amorphized area by electron irradiation is small.

Fig.III-4(a)-(d) is the post-irradiation TEM observation, and corresponding

selected are diffraction (SAD) patterns which are obtained from the central part about 250 nm in diameter of irradiated areas. The areas received the doses of (a) 1.7 x 10^{22} cm^{-2}, (b) 3.5 x 10^{22} cm^{-2}, (c) 7.0 x 10^{22} cm^{-2} and (d) 9.9 x 10^{22} cm^{-2}, respectively. The irradiation flux was 5.8 x 10^{20} cm^{-2}s^{-1}. Energy filter was used, so that electrons losing energy smaller than 8eV contribute to the SAD patterns. The plasmon energies of both c-Si and a-Si (mentioned later) are about 16-17 eV, so the contribution from plasmon, which is the major part of inelastic scattering and prevent accurate analysis was cut off. As mentioned above, electrons slightly losing energy via thermal vibration of atoms and interband transition are not removed by the energy filter in this study. For subtracting such inelastic contributions from the SAD profiles [III-1], we assumed that inelastic background intensity $I_{background}(K)$ is identical in both irradiated and non-irradiated areas of the same foil thickness. Using $I_{background}(K)$ and relativistic atomic scattering factor $f(K)$ of a Si atom [III-2], we decided the interference function as shown in (III-1).

$$K \cdot i(K) \equiv K \cdot \left(\frac{I_{observe}(K) - \alpha \cdot I_{background}(K)}{\beta \cdot \{f(K)\}^2} - 1 \right) \quad \text{(III-1)}$$

where α and β are the fitting parameters. We can obtain the RDFs $t(r) = 4\pi r \rho(r)$ from

$$t(r) = 4\pi r \rho_0 + \frac{2}{\pi} \int_0^{K_{max}} K \cdot i(K) \sin K \exp(-BK^2) dK \quad \text{(III-2)}$$

where ρ_0 is average atomic density and K_{max} is the maximum scattering wavenumber for Fourier transformation. The termination errors were reduced by the use of an artificial temperature factor $\exp(-BK^2)$ multiplying $i(K)$. Following a convention, B

32

was chosen so that $\exp\left(-BK^2_{max}\right) = 0.1$. α and β in Eq.(III-1) are determined so as to minimize the rollings in $t(r)$ at values for r less than 0.15 nm which is the nearest neighbor distance in Si.

Fig.III-4(f) shows the RDF obtained from the SAD patterns in (c) and (d). K_{max} is 108.4 nm^{-1}. In Fig.III-4, a few small peaks which appear in a range r<1.5A are artifact, since the heights and/or locations of the peaks are changed largely with changing of fitting parameters or K_{max} . As shown in Fig.III-4(f), the peaks are located in the RDF (the dose: 7.0 x 10^{22} cm^{-2}) at 0.235 nm, 0.382 nm, 0.588 nm and 0.755 nm, and in the RDF (the dose: 9.9 x 10^{22} cm^{-2}) at 0.238 nm, 0.378 nm, 0.581 nm and 0.753 nm. The third peak of c-Si at 0.45 nm is missing [I-12] as in a-Si produced by the other methods[I-9]. We compared the peak positions in RDFs obtained from electron irradiated areas to those from a-Si fabricated by other already known techniques (Table.III-2). All of them agree within the accuracy of 2 %. Therefore, we conclude that, in terms of pair-wise atomic correlation, the structures of the a-Si induced by electron irradiation are similar to those of a-Si created by other existing techniques.

III-5 Electronic Structures

An amorphized area which we produce by electron irradiation is about 300 nm in diameter. Since it is difficult to examine such a small area by optical and electrical measurements, we examined the electronic structure of amorphized areas by means of EELS. The full width at half maximum (FWHM) of zero loss peak was about 1.4 eV. The spectra were obtained from the four areas: a perfectly amorphized area, a partially amorphized area, a crystalline area close to the amorphized area and a crystalline area.

The low loss part in EELS spectrum obtained from these four areas are summarized in Fig.III-5(b). The plasmon peak is located in 16.0-16.5 eV in each spectrum and no significant change appears between a-Si and c-Si within our experimental energy resolution. It is known that plasmon peak of a-Si created by other techniques locate in 16.0-16.5 eV (Fig.III-5(b)). This shows that the electron density in valence band of a-Si created by electron irradiation is the same as that of c-Si and other a-Si, since the plasmon energy of semiconductors is determined by electron density in valence band. No remarkable peak appears at about 23 eV where a-SiO$_2$ exhibits the plasmon peak. Clearly, the amorphous induced by electron irradiation is not a-SiO$_2$.

Fig.III-5(c) shows a core loss part in the EELS spectra. The spectrum obtained from a crystalline area is flat in the energy range from 120 to 130 eV and has a sharp L$_{23}$ edge. As is generally known, in a core-electron excitation regime of a material, the loss spectra is practically identical to the loss function and the imaginary part of the dielectric function. Accordingly, the L$_{23}$ ELNES of silicon perfect crystal corresponds to the partial (or projected) state density in the conduction band: the 2p-inner-shell electrons can be excited by fast electrons to the s and d states in the conduction band whenever the dipole-transition rule is valid. The shape of the spectrum from the crystalline area is the same as the references [III-7,8]. On the other hands, the spectrum obtained from amorphous areas is sharp in the range 120-130 eV and the L$_{23}$ edge is blunt. The shape of the spectrum from the perfectly amorphized area is the same as the references [III-8]. In the core loss spectrum of a-SiO$_2$ [III-8], the first edge appears at about 106 eV. Consequently, it is clear that the amorphous induced by electron irradiation is not a-SiO$_2$ but a-Si. These EELS results shows that a-Si by electron irradiation has the same density of states as a-Si created by other techniques.

III-6 Thermal Stability

Fig.III-6 shows an *in-situ* observation of recrystallization process of an amorphous region. Before annealing (Fig.III-6(a)), halo rings appear in a SAD pattern and, as mentioned above, an a-c interface is rough. After annealing at 500 ℃ for 120 minutes (Fig.III-6(b)), the recrystallization was caused by solid phase epitaxy (SPE) at the a-c interface and the roughness of interface is reduced. The SPE growth rate is about 4 nm/hour. However, significant change in SAD pattern is not found. 10 minutes later, we raise the sample temperature to 550 ℃. After annealing at 550 ℃ for 35 minutes (Fig.III-6(c)), the SPE growth at the a-c interface progress further. The SPE growth rate is about 137 nm/hour. The activation energy for SPE are estimated to be about 2.6 eV at both temperatures. On the other hand, in the amorphous region away from the interface, it is found that several crystalline grains nucleate. After annealing at 550 ℃ for 43 minutes (Fig.III-6(d)), the amorphous region was perfectly converted into a lot of tiny poly-crystalline grains. In SAD, halo rings change to Debye-Scherrer rings due to poly-crystalline Si.

Table.III-2 summarizes the characteristics of *a*-Si created by various methods. The activation energies for SPE in pure *a*-Si are different from those in hydrogenated *a*-Si prepared by PECVD. It is considered that hydrogen influences on recrystallization process. *a*-Si created by CVD or vacuum evaporation tend to be converted into polycrystal by annealing, since its recrystallization is greatly influenced by the interface structure between the substrate and the deposited *a*-Si. The amorphized Si introduced by self ion implantations is converted into not polycrystal but monocrystal with solid phase epitaxy (SPE) [III-3]. In our experiments (Fig.III-6), electron-irradiation-induced amorphous

was converted to polycrystal. We suppose that fragmented tiny c-Si regions, as seen in Fig.III-6(c), are included in amorphous area and they act as the nucleation centers for poly-crystallization. This suggests that the structure of a-Si created by electron irradiation slightly differ from that of a-Si created by ion implantation, even though the peak positions of RDF are identical.

III-7 Discussion

III-7-1 Elementary process of amorphization

We clarified that amorphization is induced by overlapping of cascade damages. Consequently, it is considered that amorphized volume is the sum of the cascade damages' volume. Thus, measuring the change of amorphized volume with irradiation, we obtain more information about elementary process of amorphization. The procedure of our analysis is summarized in Fig.III-7. The amorphized volume is approximately in proportion to the intensity of halo ring in electron diffraction. As mentioned in section II-4-2, we measured radial profile of diffraction pattern. Then, we measured the intensity of the first halo ring from the profiles. Fig.III-8 shows the change of diffraction patterns with dose.

According to kinematical diffraction approximation, intensity of halo rings is in proportion to the volume of amorphized areas as

$$I_{kinematical}(K) = N\{f(K)\}^2 \left\{ 1 + \int_0^\infty 4\pi r^2 [\rho(r) - \rho_0] \frac{\sin(Kr)}{Kr} dr \right\} \propto N \qquad \text{(III-}$$

3),

where N is the number of atoms which are involved in the intensity of halo ring, $f(K)$ is atomic forming factor of Si, $4\pi r^2 \rho(r)$ is the RDF, ρ_0 is the number density of atoms in amorphized silicon, and K is twice of scattering vector($\frac{4\pi \sin\theta}{\lambda}$). The mean free path of elastic scattering of 100 keV incident electrons is about 120 nm [III-9]. The foil thickness, t of the irradiated areas which we measured intensity of halo rings range from 40 nm to 120 nm. However, even in the thickness range, it is considered that multiple elastic scattering lead to the gap from the kinematical approximation (III-3). In an area thinner than 120 nm, it is expected that the effect of multiple scattering reduces halo intensity. We measured halo intensity at five fully amorphized areas of different thicknesses (Fig.III-9). As we expected, the intensities of the first halo rings is not linearly proportional to thickness. Nevertheless, $I_0(t)$ can be fitted with the function shown in Fig.III-9, and this function, $I_0(t)$ is used in the following analysis.

We determine the number of atoms in the smallest cascade. The measurements of intensity of halo rings were performed over the thirty irradiated areas. Then, we normalized all $I(D,E,t)$ by

$$n(D,E) = \rho_0 \frac{I(D,E,t)}{I_0(t)} \qquad \text{(III-4)},$$

where ρ_0 is the number density of atoms in amorphized silicon. Since the number density of atoms in c-Si and a-Si is the almost same within 1-2% error [III-10], we consider the density to be $\rho_0 = 8/5.43^3$ (Å^{-3}). $n(D,E)$, determined by Eq.(III-4), is the

37

number of atoms involved in amorphous,N per unit volume. It is equal to 0 in perfect

crystal and to ρ_0 in fully amorphized area, respectively.   In Fig.III-10, we plot all

$n(D,E)$ as a function of D (dose)and E (irradiation energy). Here, we calibrated also

the fluctuation of the electron beam current during recording diffraction patterns. In

Fig.III-10, we see again that higher energy electron irradiation efficiently induces

amorphization.

The fraction of crystalline volume left in partly amorphized areas is expressed as

$1 - n(D,E)/\rho_0$ ($0 \leq n \leq \rho_0$), as $n(D,E)$ in fully amorphized area is equal to ρ_0. The

derivative, $\dfrac{\partial n(D,E)}{\partial D}$ is the amorphization ratio per irradiated electron, and is in proportion

to $1 - n(D,E)/\rho_0$ as

$$\frac{\partial n(D,E)}{\partial D} = k_0(E)\{1 - n(D,E)/\rho_0\} \qquad \text{(III-5)},$$

$\dfrac{\partial n(D,E)}{\partial D}$ converge on zero when the volume of crystal decrease as a result of the

progress of amorphization. $k_0(E)$ in Eq.(III-5) is the value of $\dfrac{\partial n(D,E)}{\partial D}$ at $D = 0$.

Solving Eq.(III-5) with the initial condition that $n = 0$ when $D = 0$, $n(D,E)$ should be

described as

$$n(D,E) = \rho_0\{1 - \exp[-k_0(E)D/\rho_0]\} \qquad \text{(III-6)}$$

In Fig.III-10, the experimental data can be fitted with the curve expressed in Eq.(III-6).

Determining $k_0(E)$ by the fitting, we estimate the number of atoms included in a

cascade (or a amorphous area) which is created by a simple recoil of an incident

electron with an atom.

All incident electrons can not produce cascades which lead to amorphizaion.

38

The cascade can be formed whenever the sufficient large energy is transferred from an electron to an Si atom. In fact, only cascade which is larger than a critical size can exist stably, and cascades which are smaller than the critical size disappear and don't contribute to amorphization. As mentioned above, we roughly estimate the lowest irradiation energy to be below 1 MeV. Here, we use the notation E_{trans} as the transfer energy from an incident electron to a target Si atom, and the notation E_{th} as the threshold transfer energy for producing the smallest cascade for contribution to amorphization. In other words, when E_{trans} is larger than E_{th}, the cascades that induce amorphization are produced. E_{max}, which represents the maximum energy transfer, changes with irradiation energy E and, for example, $E_{max}=155$ eV for $E=1$MeV. So, referring the experimental data, E_{th} may be less than 155 eV. $n(D,E)$ should be expressed as

$$n(D,E) = \int_{E_{th}}^{E_{max}(E)} n_c(E_{trans}) \cdot \sigma(E_{trans},E) \rho_0 D \cdot dE_{trans}$$

$$k_0(E) = \frac{\partial n(D,E)}{\partial D} = \rho_0 \int_{E_{th}}^{E_{max}(E)} n_c(E_{trans}) \cdot \sigma(E_{trans},E) dE_{trans} \qquad \text{(III-7)},$$

where $\sigma(E_{trans},E)$ is the energy differential of scattering cross-section that an incident electron having energy E transfers the energy E_{trans}; and $n_c(E_{trans})$ is the number of atoms included in a cascade which is produced via energy transfer E_{trans}.

Since the energy needed for production of a Frenkel pair is about 15 eV, the number of displaced atoms may be expressed by $E_{trans}/15eV$. However, as an actual recoil process, it is almost impossible that the energy is distributed equally and ideally to associated atoms as mentioned above. In Eq.(III-7), though $\sigma(E_{trans},E)$ and $E_{max}(E)$ can be calculated (Eq.(I-2) and [I-66]), $n_c(E_{trans})$ is still unknown. As the first

39

approximation, we assumed

$$n_c\left(E_{trans}\right) = \alpha\left(E_{trans} - 15eV\right) + 1 \qquad \text{(III-8)}$$

, where α is a parameter. When E_{trans} is 15 eV which is the energy for production of one Frenkel pair, Eq.(III-8) gives $n_c(15eV) = 1$, which means one Frenkel pair. As the result of substitution Eq.(III-8) into Eq.(III-7), we obtain the following equations.

$$n(D,E) = k_0(E) \cdot D \qquad \text{(III-9)}$$

$$k_0 = \int_{E_{th}}^{E_{max}(E)} \left(\alpha\left(E_{trans} - 15eV\right) + 1\right) \cdot \sigma\left(E_{trans}, E\right) \rho \cdot dE_{trans} \qquad \text{(III-10)}$$

By comparing k_0 calculated by Eq.(III-10) with k_0 experimentally obtained in Fig.III-10, the parameter α and E_{th} can be determined. Thus from Eq.(III-8), we can estimate the number of atoms included in the smallest cascades which contribute to amorphization.

As the result of weightened least square fitting to k_0 which are experimentally determined (Fig.III-10), we obtained that E_{th} =90eV and α =0.037. Fig.III-11 shows $n_c\left(E_{trans}\right)$ with the above value of α . By substituting E_{trans}=90 eV into the determined formula of $n_c\left(E_{trans}\right)$, we obtain n_c=3.8 $\pm$0.2, which is the number of atoms included in the smallest cascade which contributes to amorphization.

In case of ion implantation, E_{trans} is much larger than E_{th} and huge cascades are produced. So, it is difficult to estimate the number of atoms included in a minimum cascade which contributes to amorphization. Whereas, in case of electron irradiation, it is possible to introduce small cascades uniformly, because of high transmission ability of electron beam. As the result, we could estimate the number of atoms in cascade

experimentally.

III-7-2 Proposal of a new mechanism of amorphization

It is generally described that transformation from crystal to amorphous takes place whenever the average squared displacement of atoms from their equilibrium positions reaches a critical value [III-11]. It is also known that electron irradiation renders various compounds into amorphous [III-12], while it hardly does the elemental materials. These imply that a specific defect configuration exists in Si that possesses a certain life time during electron irradiation. Accumulation of these defects increases the static average squared displacement monotonously with dose, naturally leading to amorphization. Self-interstitials and their clusters have already been suggested as embryos of a-Si [I-3,30, III-12]. In fact, a self-interstitial [I-28] with the Jackson configuration [I-27] and a pair of di-interstitials and a divacancy [I-30] were examined theoretically, since the models include odd-membered atom rings that a-Si probably contains [I-11]. From our experimental result mentioned in section III-7-1, the number of the smallest cascade which contributes to amorphization is determined to be about four. The result means that interstitial clusters including less than four atoms aren't stable and dissolve within a short time. Whereas, it is considered that four interstitial atoms agglomerate and form a quasi-stable structure of cluster. The models are therefore evolved with the recently proposed clusters of four self-interstitials, i. e. I4 [III-13], which consist of 5-, 6- and 7-membered rings without any dangling bonds. The cluster of four self-interstitials, i. e. I4 [5-7] may be an embryo of a-Si, since I4 has the six-orientation variants as seen in Fig.III-12(d) and is stable once it is formed. A possible picture of the amorphization

41

is the accumulation of I4 clusters which possess the certain life time during electron irradiation. We suggest that the clustering of four self-interstitials takes place heterogeneously via the complex collision events and the accumulation of the clusters with dose induces amorphization.

The schematic illustration of amorphization mechanism is shown in Fig.III-12(a)-(c). During electron irradiation, not only such cascade damages but also point defects are induced in Si . We also clarified that vacancies agglomerate and form voids. In the next chapter, we discuss on them in detail.

The well known clusters of self-interstitials, i. e. the {113} defects also contain odd-membered rings. However, the environment in Si crystal, where the one-dimensionally periodic structure of the {113} defect [III-14] can be formed, presumably prevents amorphization (Fig. III-1(a)). It is know that a-Si is produced by indentation [I-19] or surface scratch [I-18]. Knowing that self-interstitials are left in c-Si after the unload as described in a theoretical study [III-15], one may also relate the amorphization under stress to the clustering of self-interstitials. On the other hand, the clusters of vacancies are unlikely to contain odd-membered rings in their structures [III-16], so they do not seem amorphous embryos.

A Molecular Dynamics simulation study [III-17] shows that when 15-20 eV recoils are given around a-c interface of Si at 250 K, recrystallization are induced at amorphous side of the interface. Consequently, high energy recoil which can knock on some atoms simultaneously promote the amorphization, on the other hand, low energy recoils which transfer only the energy near the threshold for knocking on is transferred promote the crystallization. The irradiation with the energy of more than a few hundred keV produces the competition of both effects mentioned above. It is considered that with the irradiation energy getting higher, the proportion of high energy recoils increase,

and then the amorphization become easier. The crystallization is promoted by thermal relaxation of the lattice and shaking by electron impulse. Consequently, with the temperature getting higher, effect interfering the amophization become greater. In electron irradiation, recoil energy transferred to a target atom is much smaller than in ion implantation. For example, a 2 MeV electron can transfer at most 460 eV to a Si atom. It means that the ratio of low energy recoils is rather large in electron irradiation. This may be the reason that it is difficult for electron irradiation to amorphize Si than for ion implantation.

In Fig.III-1(d), to observe the transition region between an amorphous area and a crystalline area, we notice that very rough and complicated amorphous-crystal (a-c) interfaces are formed. The transition region spreads out over several ten nm in width. Fig.III-13(a) shows HRTEM image of such a transition region at room temperature. In the area, we observed localized amorphized areas in the damaged crystal (Fig.III-13(b)) and many fragmented c-Si areas embedded in a-Si (Fig.III-13(c)). This result suggests that the amorphization by electron irradiation occurs in a heterogeneous manner.

In RDF (Fig.III-4(f)), the peaks in RDF obtained from the area at which amorphization is in progress and a lot of a-c interfaces are contained are located at the same positions as the peaks in RDF obtained from the area fully amorphized. Therefore, we conclude that, in terms of pair-wise atomic correlation, RDFs do not change whenever halo rings are detected in diffraction patterns. Transitional structure between crystalline and amorphous region is hardly identified.

As shown in Fig.III-5(c), the EELS spectrum from the crystalline side of a-c interface, is different from those from a-Si and c-Si. We tried to reproduce the spectrum as a superposition of the spectrums from crystalline and amorphous Si. When the ratio of the former to the latter for superposition is 6 to 4, the spectrum from crystalline side

of a-c interface is reproduced very well as shown in Fig.III-5(d). It may mean that no intermediate structure is formed when crystal is converted into amorphous. The results of HRTEM, RDF, EELS imply that homogeneous amorphization, in which point defects are uniformly introduced and causes gradual structure change, doesn't take place under electron irradiation.

As previously mentioned, amorphized grains and crystalline grains coexist in the irradiated area at the intermediate stage of amorphization. We suppose that cascade damages are produced as amorphous embryo, and subsequently, amorphization extends. The extension of amorphous volume may be more promoted near an a-c interface rather than inside of perfect crystal. Therefore, it is considered that expansion rate of amorphous grains surpass the production rate of amorphous embryo. At higher temperature, thermal recovery of cascade damages is greater than at lower temperature. We consider that this is the reason why the expansion of amorphous grain occurs predominantly much more at higher temperature as in the amorphization process at 94 K (Fig.III-1(b)).

Fig.III-14(a) shows dependence of amorphization on flux. More dose is needed for amorphization with higher flux irradiation. The energy transferred to specimen via inelastic scattering causes temperature rising in irradiated area. So, with the flux getting higher, the temperature rising become higher. In Fig.III-3, with the temperature getting higher, the dose needed for amorphization become higher. So, it is considered that the dependence on flux in Fig.III-14(a) comes from temperature rising in irradiated area.

Fig.III-14(b) shows dependence of amorphization on specimen thickness. All the data in Fig.3-14(b) are taken at the irradiation condition in which electron energy is 2MeV, temperature is about 25K, and fluxes range from 5.4 to 6.4 x 10^{20} cm^{-2}s^{-1}. The result means that with specimen thickness of irradiated area getting thicker, the dose needed for amorphization increases but in not proportion to thickness. If amorphization

44

progress from electron incident surface, dose needed for amorphization should be in proportion to thickness. Therefore, the amorphization occur not from surface but in bulk. It is considered that because of dispersion of electron probe caused by scattering in the specimen, substantial flux decreases in the thick specimen and, therefore, the irradiation dose needed for the amorphization increase with the increase of specimen thickness. It is supposed that this causes to gentle dependence on thickness in Fig.III-14(b).

It is well known that electron irradiation sputter the exit surface of materials and total thickness of the irradiated area decrease[III-18]. If amorphized areas have been extremely thinned by sputtering effect with electron irradiation, we can't tell whether the amophization by electron irradiation is the phenomenon in bulk Si or in extremely thin film. In order to confirm that amorphization by electron irradiation doesn't depend on such thin film effect, we performed thickness measurement by EELS, since the thickness in amorphized area can't be measured by techniques used to measure thickness of crystalline materials, such as the method by thickness fringes and convergent beam electron diffraction. The specimen thickness t is represented[III-9] as

$$t = \lambda_p \cdot \ln\left(I_{total} / I_0\right) \qquad \text{(III-11)}$$

where I_{total} is the sum of total counts in a EELS spectrum, I_0 is the sum of the counts belonging to zero loss peak, and λ_p is the mean free path about plasmon excitation, respectively. The value of λ_p depends on incident electron energy, plasmon energy, and Fermi energy of the material. Plasmon energy of amorphous Si produced by electron irradiation is almost equal to that of crystalline Si as mentioned later. We calculated Eq.(III-11) , assuming that Fermi energy of a-Si is the same value as in crystal. The measurements were performed at the two areas. The one is the center of

fully amorphized area by 2 MeV irradiation, and the other is a non-irradiated area. Thicknesses at both area were equal before irradiation. The result of thickness measurement after irradiation is that the amorphized area: 313 ± 6nm, and the non-irradiated area: 302 ± 6nm. It is clear that Si is amorphized without decreasing of thickness at the 2 MeV irradiated area and that amorphization occurs in the area more than at least 300 nm in thickness. Consequently, there is no essential relevance between amophization and thin film.

As the reason for existence of fragmented tiny c-Si regions in amorphous area, the following two can be supposed : (1) Local tiny grains may be left from amorphization in the amorphized area. In this case, the left tiny grains may common almost same crystallographic directions each other. However, rather uniform Debye-Scherrer rings appear in Fig.III-6, and hence this model is inconsistent with the experimental result. (2) There is a possibility of existence of fluctuation such as creation and annihilation of crystalline embryo as a result of competition between low energy recoil and high energy recoil as mentioned above. If such tiny c-Si regions cause to polycrystallization, uniformity in the Debye-Scherrer rings is acceptable.

IV. DEFECTS IN SILICON INTRODUCED BY ELECTRON IRRADIATION AT LOW TEMPERATURES

IV-1. Introduction

In chapter III, we reported that high energy electron irradiation at rather high dose ($D \geq 10^{22}$ e/cm^2, $E \geq 1$ MeV, $T \leq 100$ K) converts a crystalline Si to amorphous Si. It is an electron-irradiation-induced phenomenon. On the other hand, a careful look at Fig.III-1(d) shows that when irradiation was performed at 25 K, the ringed dark area surrounding the amorphized area is formed. This is caused by scattering of electron beam by defects. The ringed area received lower dose. We investigated the defects in order to clear electron-irradiation-effects extensively. The phenomenon is caused by the interaction between incident electrons as the most elementary charged particles and crystalline Si as the most typical covalent material. As the example of electron-irradiation effects in Si, the creation of {113} defects induced by electron irradiation above room temperature is well known [I-61]. Self interstitials agglomerate into {113} planes. In Fig.IV-1, we show electron micrographs of {113} defects in Si-Ge induced by electron irradiation at 500 ℃. Observing the defects by weak beam TEM technique near the [110] zone axis, they show several different shapes. This is caused by the fact that there are twelve {113} equivalent planes. There are two kinds of {113} planes which are parallel to the electron beam direction. Thus in Fig.IV-1(a), a part of the defects clearly exhibit the habit planes. Fig.IV-1(b) and (c) are HRTEM images of a side view and an inclined view of a {113} defect, respectively. In (b), the defect clearly extends along (113) plane. In (c), the strain field surrounding the defect appears asymmetrically and darkly. Such {113} defects are produced as the result of both thermal migration and athermal migration of a lot of point defects induced by electron irradiation. In order to separate two kinds of migration and to examine pure electron-irradiation effects, it is necessary to perform

irradiation at low temperature at which point defects can't migrate thermally. The lowest temperature at which point defects diffuse thermally in crystalline Si was estimated by EPR[I-1] to be 170 K for self interstitials and to be 70 K for lattice vacancies. Point defects possibly migrate below these temperatures, influenced by electronic excitation states induced by electron irradiation. Though some models for athermal migration mechanisms were proposed[IV-1], they have not been verificated experimentally. In crystalline Si, it have been found by EPR that self interstitials migrate athermally under electron irradiation at 4.2 K[I-50]. As a research by means of TEM, the small and unidentified defects were observed in c-Si irradiated by 0.65MeV electrons below 35K [I-2]. The experimental evidence on electron-irradiation-induced migration of point defects in Si at low temperature is shown in only these two reports and the whole picture, such as structures, diffusion constant, migration mechanism and so on, are unclear.

IV-2 *In-situ* TEM observation of defect production

In order to examine the ralation between the defects and the amorphization, we irradiated c-Si at 25 K with 2 MeV electrons, i.e. the same condition for amorphization, at the dose which is rather less than the dose needed for amorphizing Si. We simultaneously made *in-situ* observation of the process of defect production (Fig.IV-2). A large number of small defects are introduced only in the area about 1 μ m in diameter in which the electron probe are focused. The defects must be the same as the defects created around the amorphized area in Fig.III-1(d).

IV-3 Post-irradiation weak beam observation of the defects

The area irradiated with 2 MeV electrons at 25 K was post-irradiation observed at room temperature by means of weak beam (WB) imaging (Fig.IV-3(a)). The electron acceleration voltage was 160 kV. The WB image was taken using g=220 near the <110> zone axis. In Fig.IV-3(a), the defects appear bright and their size ranges from 1 to 5 nm. Their shape is granular and they don't exhibit the habit plane, in contrast to the well known planar clusters of self-interstitials such as the {113} defects. The spatial distribution of the defects determined by means of stereo analysis is shown in Fig.IV-3(b). Position of one surface was determined by contamination on specimen surface and the other was determined from the specimen thickness which was calculated by counting the number of thickness fringes from the edge of the specimen. It can be seen that the defects are formed not on the specimen surface but in the specimen bulk.

IV-4 Post-irradiation HRTEM observation at room temperature

Post-irradiation HRTEM observation of the defects produced by 2MeV electron irradiation at 25 K was performed with a 200 kV TEM at room temperature. Fig.IV-4(a) shows low magnification view from a <110> direction of an irradiated area in which a lot of defects are created. The defects show contrast depending on specimen thickness. They appear bright in the area in which matrix appears dark, and oppositely dark in the area in which matrix appears bright. Fig.IV-4(b) is the more magnified image of the irradiated area.

The defects show characteristic image contrast. In Fig.IV-5(a), we see experimental through focus images of the two defects located in the area of different thickness. The both defects about 3 nm in diameter are observed in the center of micrographs. In the thinner area, the defect can only be seen at $\Delta f=-70nm$ and $\Delta f=-80nm$. On the other

hand, in the thicker area, the imaging condition is much more narrow and, in fact, defect contrast can only be seen at Δf=-80nm. Such a characteristic image contrast isn't known and is different from that of planar defects, such as {113} defect shown in previous chapter. It is clarified that the structure of the defects found here is different from the structure of known defects in pure Si.

IV-5 *In-situ* HRTEM observation of defect production

In order to examine whether the defects are produced by low energy irradiation which never induces amorphization, we performed 0.3 MeV irradiation to crystalline Si. A cleavaged sample was set on a cooling specimen container in 0.3 MV TEM. A sequence of the *in-situ* HRTEM observation at 4.2 K is depicted in Fig.IV-6. It is certain that defects are created by electron irradiation. The creation process of a defect is summarized in Fig.IV-7. After irradiation for 30 s, we find that a defect grew. After prolonged irradiation, it appeared more clearly. Fig.IV-8 is a set of HRTEM images observed at 4.2 K and room temperature of the same irradiated area. It is clear that there is no change in the positions of the defects before and after temperature raising. In addition, we found that the defects show the same characteristic image contrast in Fig.IV-5(b) as that of the defects induced by 2MeV irradiation in Fig.IV-5(a). Consequently, we conclude that the defects produced by 0.3 MeV and 2 MeV irradiation have the same nature, and they retain their nature after temperature raising to room temperature. The energy of incident electrons (0.3MeV) is sufficient to create Frenkel pairs, and insufficient to create cascade damages, since the threshold electron energy for displacement damage is about 0.15MeV. Therefore, we conclude that the defects are secondary defects which are due to the agglomeration of point defects at 4.2K.

50

IV-6 Thermal stability of the defects

As mentioned in the previous chapter, since the nature of the defects at room temperature is the same as that at low temperature, we performed precise analysis of their nature at higher than room temperature. To examine the nature of the defects, thermal stability of the defects at 500 ℃ was examined. Fig.IV-9(a)-(d) shows a sequence of the *in-situ* weak-beam observation during thermal annealing. Fig.IV-9(e) is the histgram showing the distribution of the defect size. Though about 30 % of the defects at room temperature disappear after 1 hour annealing at 500 ℃, most of them remain. After that, when 1 hour annealing at 600 ℃(Fig.IV-9(c)) and 1 hour annealing at 700 ℃(Fig.IV-9(d)) are performed, only part of the defects grow up and exhibit the habit planes, although most of them disappear.

IV-7 The structure model of the defects induced by electron irradiation at low temperatures

As introduced in the previous section, the planar defects which extend two dimensionally are well known in Si. In contrast, the defects found here extends three dimensionally. Therefore, the following two models are possible.

1) void: A three-dimensional cluster of lattice vacancies is called ' void'. The outer walls of voids tend to be crystallographic surface whose surface energy is low, such   as (1 1 1).

2) tiny amorphous grain:

51

since, from the result of the previous chapter, it was clarified that 0.3 MeV electron irradiation can't induce amorphization, the possibility of this defect model may be low. We list this model purely as one choice based on the three dimensional form of defects.

IV-8   HRTEM image simulation of defect models

As mentioned above, planar defects don't represent experimental HRTEM images in Fig.IV-5 at all. On the other hand, we performed HRTEM image simulations of two defect structure models for checking whether the models represent experimental HRTEM images. Fig.IV-10(a),(b) illustrates cross-sectional view of the simulated structures, which are crystalline Si films including inside a defect, i.e. a void or an amorphous grain. The defects have the shape of a cylinder of 4.6 A in diameter and in height. The structures shown in Fig.IV-10(a),(b) were build by stacking of layers shown in Fig.IV-10(c)-(e). All of the three different super cells in Fig.IV-10(c)-(e) have volume of 65.3 A x 65.2 A x 7.68 A. The shortest lattice vector is parallel to [110] direction of Si crystal. The unit (a) is the super cell of perfect crystal and includes 1632 atoms. In (b), the central cylindrical area of 4.6 A in diameter is removed. In (c), atoms in the same cylindrical area are randomly displaced keeping nearest neighbor distance above 1.5 A. For constructing the structure of Fig.IV-10(a), the stacking of six layers shown in (d) was put between some of layer shown in (c). And for the structure in Fig.IV-10(b), six layers shown in (e) which have different random structure one another were used instead of the stacking of layer (d).

The parameters for the image simulations are as follows:

· Accelerating voltage   :   200 kV

· Spherical aberration constant   :   0.5 mm

· Defocus spread caused by

        chromatic aberration   :   82.5 A

· Beam divergence semi angle   :   1.5 mrad

· Objective aperture size   : $0.7 A^{-1}$

     The simulated images shown in Fig.IV-11,12 are calculated based on the multislice method (section II-2-3) for different values of the crystal thickness and the defocus. The feature that the defects appear brightly in a thin area and darkly in a thick area agrees with Fig.IV-4. In addition, the characteristic image contrasts in Fig.IV-5(a) and Fig.IV-5(b), which planar defects never show, are well reproduced. Therefore, it is certain that either of the defect models is right. However, the difference between the results of both models is slight and it is difficult to determine only from experimental HRTEM images whether of the models is right. Therefore, we consider the result of annealing(sectionIV-6).

IV-9 Discussion on the nature of the defects

     As mentioned the previous chapter, amorphous Si is recrystallized from a-c interface by SPE process at the rate of about 30 nm / hour at 500℃. Consequently, if the defects are amorphous grains less than 5 nm in size, they must disappear after 1 hour annealing at 500 ℃. Therefore, the model that the defects are amorphous grains is denied.

     In Fig.IV-9, the diameter of the defects which disappeared after 1 hour annealing at 500 ℃ is less than 3 nm. It is considered that the small voids shrank by releasing of vacancies and/or absorption of interstitials. since decrease of diameter of a large void by releasing of one vacancy is smaller than that of a small void, the number of the voids more than 3 nm in diameter may scarcely change. Possibly, by Ostwald-Ripening

mechanism[IV-2], large voids absorbed vacancies released from small voids. There is also a little possibility that part of the disappeared defects less than 3 nm in diameter is amorphous grains. However, the defects about 5 nm in diameter are observed in Fig.IV-9 and it is certain that they are voids. It is considered that they absorbed a lot of vacancies released from other small voids resulted in extension to vacancy-type planar defects as shown in Fig.IV-9(c) and (d). In conclusion, a large number of voids are surely produced in irradiated areas.

IV-10   HRTEM image simulation of void model

We summarize the characteristics of the defects in Table.IV-1. As the result of discussion in section IV-9, the defect model which can reproduce all the characteristics in Table.IV-1 is only the void model. In this section, we perform the more precise image simulations of the void model also taking the size and the figure of a defect into consideration and compare the results to experimental HRTEM images of the defect. The parameters used in the simulation are the same as in section IV-8. About the HRTEM images recorded at the three different values of defocus, we obtained the radial profiles of the Fourier transform(Fig.IV-13) which is from the images of the oxidized amorphous area at the sample edge. since amorphous materials have almost uniform Fourier coefficient of electrostatic potential, it is clear from Eq.(II-19) that radii of dark rings in a Fourier transform of an amorphous image mean a spatial frequency that a contrast transfer function is equal to zero. We decided the values of defocus satisfying the above condition. The result is that (a) -61nm, (b) -70nm, (c) -80nm. Based on the values of defocus, we performed image simulations. Fig.IV-14 shows the best fit with experimental HRTEM images of a defect. The void model reproduces the observed images very well. The

value of defocus previously measured is the value at the edge of the wedge-shaped sample. At the area 13 nm in thickness, it is expected that the values of defocus shift to minus values about 6 nm which is the half of thickness of the wedge-shaped sample.

From the above results, we conclude that voids are produced in crystalline Si by electron irradiation at low temperature. since also 0.3 MeV irradiation produces them, they are due to athermal migration of vacancies. Consequently, we succeeded in finding the athermal diffusion of voids at atomic level and in real time for the first time.

IV-11   Discussion on the relation between amorphization and defect creation

In Fig.III-1, although the numerous small defects at the periphery of the irradiation spot are introduced by electron irradiation at 25 K or 60 K. Whereas, the production of defects are suppressed at 94 K. The difference suggests that the production of defects isn't directly connected with amorphization in Si. The result denies that the defects are the early stage of amorphization and doesn't contradict that the defects are not amorphous grain. since the 2 MeV electron irradiation produces small cascades less than 1 nm in size, the irradiated area should contains voids and cascades. All the cascades must disappear during annealing at 500 ℃.

It is clarified that most of the defects which are produced by much lower dose than the dose needed for amorphization are not amorphous grains but voids. We compile the dependence of defect creation condition on temperature and irradiation energy in Fig.IV-15. The border between creation condition of voids and {113} defects exsist somewhere between about 100 K and room temperature. In Fig.IV-16, we summarized the conditions of amorphization and defect creation expressed as the cross-sectional view of Fig.III-3 and Fig.IV-15. The defects are introduced also by 0.3 MeV electron irradiation

which can introduce Frenkel pairs but can't introduce cascade damages. So, this agrees with the result gained from the analysis of amorphization condition in section III-3 and amorphization rate in section III-7-1.

The displacement of an atom by primary knock on under irradiation produces two types of defect which are cascades and point defects. The production of cascades lead to amorphization. On the other hand, point defects migrate and agglomerate under irradiation. The agglomeration of vacancies results in the production of voids. Though interstitials are unidentified experimentally, they also may migrate[I-50]. Even if an interstitial meet another interstitial, they may not produce a stable complex. As the result of migration, they reach an a-c interface or a surface of specimen. The one which reached an a-c interface may contribute to increasing of amorphous volume. On the other hand, in the case of 0.3 MeV irradiation, amorphous areas aren't created. Therefore, it is considered that vacancies agglomerate and voids are created as the result of athermal diffusion of point defects(Fig.IV-17). This situation is a contrast to that interstitials agglomerate in {113} plane under high temperature irradiation(Fig.IV-18)

V.   APPLICATION OF THE NEW AMORPHIZATION TECHNIQUE

As mentioned in the previous chapter, we obtained a new method, electron irradiation, to amorphize c-Si. The method has the advantage of a following respect over any other methods. A MeV electron beam can be focused on an area smaller than 0.2 μm in diameter, and can be scanned freely. We can make optional two dimensional (2D) sub-micron periodic structures which consist of a-Si dots in a c-Si film. Fig.V-1 shows an optical photograph and the electron micrograph of a 7x7 of 2D square lattice of a-Si dots in c-Si film, which we produced actually. Since the structure is as fine as wave length of visible light, the optical photograph is fuzzy. The electron micrograph clearly shows that the submicron periodic structure is produced. Moreover, we can also introduce defects in the lattice freely. Applications of the method to making submicron strucures is anticipated. One example of application is to produce photonic crystals[V-1]. Fabrication of Photonic crystals based on silicon-related materials having submicron periodicity come to be possible gradually within a few years[V-2, 3], and development is not enough yet. It is important to try to make a photonic crystal by our new method.

It is necessary that dielectric constant of a-Si is different from that of c-Si so that a periodic structure forms a photonic band. Actually there is a slight difference in dielectric constant of between c-Si and a-Si in the range from visible to ultra violet[V-4]. However, since electromagnetic waves in the energy range can't transmit c-Si, appearance of bandgap don't cause any changes in optical features. The problem originates from severeness of condition that difference of dielectric constant of between c-Si and a-Si is slight. To solve the problem, it is considered to remove only a-Si selectively and to change the system into the structure which air holes are periodically arranged in c-Si film. If such process is achieved, it is expected that the system acts as a photonic crystal. We calculated photonic band respected in such structures. The calculation was

performed by the plane wave expansion method, which is explained in the following.

We assume the following assumptions. First, we assume the electromagnetic field strengths are small enough so that we are in the linear regime. Second, we assume the material is macroscopic and isotropic, so that $E(r,\omega)$ and $D(r,\omega)$ are related by a scalar dielectric constant $\varepsilon(r,\omega)$. Third, we ignore any explicit frequency dependence of the dielectric constant. Fourth, we focus only on low-loss dielectrics, which means we can treat $\varepsilon(r)$ as purely real. Since, for most dielectric materials of interest, the magnetic permeability is very close to unity, we may set $B = H$.

With all of these assumptions in place, the Maxwell equations become

$$\nabla \cdot H(r,t) = 0$$
$$\nabla \times E(r,t) + \frac{1}{c}\frac{\partial H(r,t)}{\partial t} = 0$$
$$\nabla \cdot \varepsilon(r)E(r,t) = 0 \qquad \text{(V-1)}$$
$$\nabla \times H(r,t) - \frac{\varepsilon(r)}{c}\frac{\partial E(r,t)}{\partial t} = 0$$

We employ writing a harmonic mode as a certain field pattern times a complex exponential:

$$H(r,t) = H(r)e^{i\omega t}$$
$$E(r,t) = E(r)e^{i\omega t} \qquad \text{(V-2)}$$

We insert the above equations into Eq.(V-1). The two curl equations relate $E(r)$ to $H(r)$:

$$\nabla \times E(r) + \frac{i\omega}{c}H(r) = 0$$
$$\nabla \times H(r) - \frac{i\omega}{c}\varepsilon(r)E(r) = 0 \qquad \text{(V-3)}$$

By eliminate $E(r)$, we obtain an equation entirely in $H(r)$:

$$\nabla \times \left(\frac{1}{\varepsilon(r)} \nabla \times H(r) \right) = \left(\frac{\omega}{c} \right)^2 H(r) \qquad \text{(V-4)}$$

In uniform materials, ε is a constant independent on r. However, in the case that $\varepsilon(r)$ has spatial periodicity, we can expand the field pattern into a set of plane waves. Requiring that $H(r)$ shares the periodicity of $\varepsilon(r)$ amounts to only including the crystal's reciprocal lattice vectors $\mathbf{G}$ in the expansion:

$$H_\omega^\mathbf{k}(\mathbf{r}) = \sum_{\mathbf{G},\lambda} h_{\mathbf{G},\lambda} \hat{e}_\lambda \exp[i(\mathbf{k}+\mathbf{G}) \cdot \mathbf{r}] \qquad \text{(V-5)}$$

We have identified each mode with a wave vector $\mathbf{k}$, and each mode is built out of plane waves with wave vector $\mathbf{k}+\mathbf{G}$ for all reciprocal lattice vectors $\mathbf{G}$. The polarization of each plane wave is one of the two unit vectors $\hat{e}_\lambda$, indexed by the label λ.

Before inserting this expansion into the master equation, we should also expand $1/\varepsilon(r)$ in plane waves. Call $\varepsilon^{-1}(\mathbf{G},\mathbf{G}')$ the coefficient on the plane wave with wave vector $G-G'$. Inserting both expansions into Eq.(V-4), we obtain a system of linear equations on the expansion coefficients:

$$\sum_{(\mathbf{G},\lambda)} \Theta^\mathbf{k}_{(\mathbf{G},\lambda),(\mathbf{G},\lambda)'} h_{(\mathbf{G},\lambda)'} = \left(\frac{\omega}{c} \right)^2 h_{(\mathbf{G},\lambda)} \qquad \text{(V-6)}$$

Here, theta is the matrix dependent on $\mathbf{k}$ and λ.

$$\Theta^\mathbf{k}_{(\mathbf{G},\lambda),(\mathbf{G},\lambda)'} = [(\mathbf{k}+\mathbf{G}) \times \hat{e}_\lambda] \cdot [(\mathbf{k}+\mathbf{G}') \times \hat{e}_{\lambda'}] \varepsilon^{-1}(\mathbf{G},\mathbf{G}') \qquad \text{(V-7)}$$

Eq.(V-6) is the eigenvalue equation and the solutions are the energy eigenvalues for electromagnetic wave in the material. By calculate Eq.(V-6) about all k-values, we can obtain the photonic band structure in the materials. In the case of 2 dimensional photonic crystals, the mode of electromagnetic wave propagating in the periodic plane

are classified into two polarizations. Transverse-electric (TE) modes have H normal to the plane, and E in the plane. Transverse-magnetic (TM) modes have just reverse. The band structures for TE and TM modes can be completely different.

We considered a 2D square and a triangular lattice with a lattice constant $a = 200$ nm The elementary lattice vectors are $(a, 0)$, $(0, a)$ in the square lattice, and $(a, 0)$, $(a/2, \sqrt{3}a/2)$ in the triangular lattice, respectively. There are circler air holes of 100 nm in diameter at all lattice points. The rest of the sample consists of c-Si. We assumed that the dielectric constant of c-Si and air are 14 and 1, respectively. 64 plane waves were used for the calculations. In Fig.V-2, the calculated photonic band structures are shown along the lines drawn among symmetric three points in the Brillouin zones. We found that in FigV-2, the band structures of TE mode have a band gap. The band gap ranges between 0.22 and 0.35 of $\omega a/2\pi c$, that is, between 0.57 and 0.91 μm in wavelength. The range corresponds to between yellow and infra-red. Electromagnetic waves in the energy range transmit a c-Si film well, on the other hand, they are totally reflected at such 2D structures. Therefore, we must be able to measure the band structures by reflection and transmission experiments using polarized light which magnetic fields oscillate in the plane perpendicular to the 2D photonic structures.

As an example of application of the new amorphization technique, we mentioned that the possibility of fabrication of photonic crystals based on Si. In the future, it is expected that amorphization in Si by means of electron probe is applied to also other submicron technologies.

SUMMARY

We examined the electron-irradiation-induced effects in crystalline Si at low temperature by means of TEM and the associated techniques. The description concerned with amorphization and with creation of lattice defects is mentioned in chapter III and in chapter IV, respectively.

In chapter III, from the investigation into the dose of electrons needed for amorphization with the various irradiation energies (0.2, 0.3, 1, 1.5, 2, 2.5, 3 MeV) and at various temperatures (25, 55, 75, 95, 115 K), we clarified that the irradiation by electron with energy of above above 1.5 MeV below 100K was needed for the amorphization. From the results, we conclude that amorphization in Si by charged particle irradiation is caused by accumulation of not point defects but small cascade damages. Analyzing the change in the intensity of halo rings with irradiation energy and dose precisely, we clarified that the smallest cascade which contributes to amorphization included about only four atoms. This leads us into proposing a new amorphization mechanism that four interstitial atoms form the quasi-stable structure in crystalline Si and become an amorphous embryo. By means of electron-energy-filtered diffraction, electron energy loss spectroscopy, and *in-situ* observation at elevated temperatures, we clarified the atomic structure, the electronic structure, and the thermal stability of amorphous silicon by the new amorphization technique. The short range atomic structure and the electronic state in the conduction band is almost the same as that of amorphous silicon created by other existing techniques. However, unlike amorphous silicon introduced by ion implantation, amorphous silicon by electron irradiation is converted to polycrystals at 550℃.

In chapter IV, we succeeded in observing the process of the defects creation induced by 300 keV electron irradiation at 4.2 K by means of *in-situ* HRTEM observation. The post-irradiation HRTEM and weak beam observation at room temperature show

that the defects are in the shape of distorted sphere, less than 5 nm in diameter, and distributed in specimen bulk. In addition, it was clarified that the defects gradually shrank by annealing at 500 - 700 ℃. From the result and the comparison between observed HRTEM images and simulated ones, we concluded that the defects were voids as the result of athermal migration of lattice vacancies under electron irradiation. We succeeded in finding the athermal diffusion of voids at atomic level and in real time for the first time. In the last of chapter IV, we discussed a generalized view of electron-irradiation-induced effects in crystalline Si at low temperature based on the results in chapter III and IV. We concluded that the agglomeration of lattice vacancies resulted in voids, and on the other hand, the production of cascades lead to amorphization.

Finally, we mentioned about the application of the new amorphization technique to manufacturing Si in submicron scale, such as production of two dimensional photonic crystals.

ACKNOWLEDGMENTS

Reference

Chapter I

[I-1]   G. D. Watkins, " Lattice Defect in Semiconductors ", Inst. Phys. Conf. Ser., No. 23, Inst. Phys, London and Bristol: (1975) p.1.

[I-2]   H. Foll, p.233 in ref.[I-1]

[I-3]   D. N. Seidman, R. S. Averback, P. R. Okamoto and A. C. Baily, Phys. Rev. Lett. 58, (1987) 900.

[I-4]   C. Kittel, Introduction to Solid State Physics(7th Ed.), John Wiley & sons, Inc.(1996)

[I-5]   K. Laaziri, S. Kycia, S. Roorda, M. Chicoine, J. L. Robertson, J. Wang, and S. C. Moss, Phys. Rev. Lett. 82, (1999)3460.

[I-6]   J. Fortner and J. S. Lannin, Phys. Rev. B 39, (1988) 5527.

[I-7]   R. Mosseri, J. C. Malaurent, C. Sella and J. Dixmier, J. Non-Cryst. Solids 35-36, (1980) 507.

[I-8]   P. Duwez, et al. (1960)

[I-9]   S.C. Moss and J.F. Graczyk, "Proc. 10th Int'l conf. Phys. Semicond"(1970) p.658

[I-10] D.E. Polk, J. Non-cryst. Solids, 5 (1971) 365.

[I-11] P. Steinhardt, R. Alben and D. Weaire, J. Non-crystalline Solids, 15 (1974) 199.

[I-12] F. Wooten, K. Winer, D. Weaire, Phys. Rev. Lett., 54 (1985) 1392.

[I-13] D. Weaire and M.F. Thorpe, Phys. Rev. B4 (1971) 2508

[I-14] E.N. Economou, C.M. Soukoulis, M.H. Cohen and S. John, "Disordered Semiconductors" ed. by M.A. Kastner et al. (Plenum Press, 1987) p.681

[I-15] W.E. Spear and C.S. Cloude, Philos. Mag. B58, (1988) 467

[I-16] H. Okamoto and Y. Hamakawa, J. Non-Cryst. Solids 77/78 (1985) 1441

[I-17] D. Adler, " Hydrogenated Amorphous Silicon, Part A", in " Semiconductors and

Semimetals " Vol. 21, ed. by J.I. Pankove (Academic Press, 1984) 291

[I-18] K. Minowa and K. Sumino, Phys. Rev. Lett. 69, (1992) 320.

[I-19] D. R. Clarke, M. C. Kroll, P. D. Kirchner, R. F. Cook and B. J. Hockey, Phys. Rev. Lett. 60, (1988) 2156.

[I-20] S. Kugler, G. Molnar, G. Peto, E. Zsoldos, L. Rosta, A. Menelle, and R. Bellissent, Phys. Rev. B 40, (1989) 8030.

[I-21] A.G. Cullis, H.C. Webber, N.G. Chew, J.M, Poate, P. Baeri, Phys. Rev. Lett. 49,(1982) 219

[I-22] S. Takeda, and J. Yamasaki ,Phys. Rev. Lett., 83, (1999) 320

[I-23] J. Yamasaki, and S. Takeda, Mater. Res. Soc. Symp. Proc., 557,(1999) 231

[I-24] S. Takeda, J. Yamasaki, and Y. Kimura, Physica B, 273-274, (1999)476

[I-25] F.F. Morehead, Jr. and B.L. Crowder, Radiat. Eff. 6, (1970)27

[I-26] O.W. Holland, S.J. Pennycook, and G.L. Albert, Appl. Phys. Lett. 55, (1989)2503

[I-27] L. C. Kimerling, in Defects and radiation effects in semiconductors 1978, edited by J. H. Albany,   Inst. Conf. Ser. No. 46 (Institute of Physics, Bristol and London1979) p. 56.

[I-28] V. J. B. Torres, P. M. Masri and A. M. Stoneham, J. Phys. C: Solid State Phys. 20, (1987)L143.

[I-29] J. W. Corbett, J. P. Karins and T. Y. Tan, Nuclear Instruments and Methods 182/183, (1981)457.

[I-30] T. Motooka, S. Harada and M. Ishimaru, Phys. Rev. Lett. 78, (1997) 2980.

[I-31] J. Bloch, J. Nucl. Mater. 6 (1962) 203

[I-32] J.M. Howe and M.H. Rainville, J. Nucl. Mater. 68 (1977) 215

[I-33] G. Thomas, H. Mori, H. Fujita and R. Sinclair, Scr. Metall. 16 (1982) 589

[I-34] G. D. Watkins, and J. W. Corbett, Phys. Rev. 121(1961)1001.

[I-35] G. D. Watkins, and J. W. Corbett, Phys. Rev. 134 (1964) A1359.

[I-36] G. D. Watkins, and J. W. Corbett, J. W.Phys. Rev. 138 (1965) A543.

[I-37] M. Saito, and A. Oshiyama, Phys. Rev. B53, (1996) 7810.

[I-38] S.I. Tan, B.S. Berry and W. Frank, in "Ion Implantation in Semiconductors and Other Materials" p.19

[I-39] W. Frank, Rad. Effects, 21, (1974)119

[I-40] W.Frank,Conf.Ser. p.23 in ref.[I-1]

[I-41] K.Morita and H.D. Corbett,Rad.Effects,28(1976) 97.

[I-42] W.Jung and G.S. Newell,Phys. Rev., 132 (1963) 648.

[I-43] Y-H. Lee and J.W.Corbett,Solid State Commun.,15 (1974) 1781.

[I-44] D.F. Daly, J.appl.Phys.,42 (1971) 864.

[I-45] K.L.Brower, Phys.Rev., B14 (1976) 872.

[I-46] K.L. Brower,Preprint of the Dubrovnik Conf. (1976) B1(Not presented).

[I-47] Y-H. Lee,Y.M. Kim and J.W.Corbett,Rad.Effects,15 (1972) 77.

[I-48] K.Murakami, K.Masuda, K. Gamo and S.Namba,Ion Implantation in Semiconductors, ed. S.Namba (Plenum Press, New York, 1975) p.533.

[I-49] G.D. Watkins, J. Phys. Soc.Japan 18 (1963) Suppl., Vols. I~III.

[I-50] G.D.Watkins, Radiation Damage in Semiconductors,ParisRoyaumont,1964 ,ed. P.Baruch (Dunod, Paris, 1965).

[I-51] G.D.Watkins,Phys.Rev.,B12 (1075) 4833.

[I-52] G.D. Watkins and J.W. Corbett, Disc.Faraday Soc.,31 (1961) 86.

[I-53] J.W.Corbett and G.D.Watkins,Phys.Rev. Letters, 7 (1961) 314.

[I-54] J W.Cobett and G.D. Watkins, Phys Rev., 138A (1965) 555.

[I-55] Y-H. Lee and J.W. Corbett, phys.Rev., B9 (1974) 4351.

[I-56] K.L. Brower, Rad. Effects, 8 (1971) 213, Radiation Effects in Semiconductors, Albany, 1970, ed.J.W. Corbett and G.D. Watkins, (Gorden and Breach, London, New York and Paris, 1971).

[I-57] K.L. Brower and W.Beezhold,II Int. Conf.Ion Impl. inSemiconductors, ed. I.

Ruge

and J.Groul (Springer,Berlin, 1971) ;.7,cited in F.L.Vook, Radiation Damage and Defects

in Semiconductors,Reading, 1972, ed.J.E.Whitehouse,Conf.Ser. No.16 (The Institute of

Physics,London and Bristol, 1973).

[I-58] M. Nizenoff and H.Y.Fan, Phys.Rev., 128 (1962) 1605.

[I-59] Y-H.Lee and J.W. Corbett, phys.Rev., B8 (1973) 37.

[I-60] S. Takeda and T. Kamino, Phys. Rev. B, 51, (1995) 2148

[I-61] Tang, Z., Hasegawa, M., Chiba, T., Saito, M., Kawasuso, A., Li, Z.Q., Fu, R.T.,

Akahane, T., Kawazoe, Y., Yamaguchi, S.,Phys. Rev. Lett.,78,(1997)2236

[I-62] Corbett, J. W. and Bourgoin, J. C. (1975) Defect creation in semiconductors,

in Point Defects in Solids, Vol. 2, Semiconductors and Molecular Crystals edited by J.

H. Crawford, Jr. and L. M. Slifkin (Plenum Press, New York and London): 1-162.

[I-63] Stolk, P.A., Gossmann, H.-J., Eaglesham, D.J., Jacobson, D.C., Rafferty, C.S.,

Gilmer, G.H., Jaraiz, M., Poate, J.M., Luftman, H.S., Haynes, T.E., J. Appl. Phys., 81

(1997) 6031.

[I-64] N.F. Mott, Proc. Roy. Soc. A124, 426 (1929).

[I-65] N.F. Mott, Proc. Roy. Soc. A135, 429 (1932).

[I-66] W.A. MacKinley and H. Feshvach, Phys. Rec. 74, (1948) 1759.

[I-67] Lang, D. V. and Kimerling, L.C. Appl. Phys. Lett. 28 (1976) 248.

[I-68] Spence, J. C. H and Kolar, H. Philos. Mag. A39 (1979) 59.

[I-69] Chiang, S.-W., Carter, C. B. and Kohlstedt, D. L.Philos. Mag. A42 (1980) 103.

[I-70] Sato, M., Hiraga, K. and Sumino, K. Jpn. J. Apll. Phys. 19 (1980) L 155.

[I-71] Anstis, G. R., Hirsch, P. B., Humphreys, C. J., Hutchison, J. L. and Ourmazd, A.

(1981) Lattice images of the core of $30°$ partialas in silicon.

[I-72] Coene, W. Bender, H. and Amelinckx, S. Philos. Mag. A52 (1985) 369.

[I-73] Ichinose, H., Ishida, Y., Furuta, T. and Sakaki, S. J. Electron Microscopy,
36(1987) 82.

[I-74] Ourmazd, A., Schwander, P. Krisielowski, C., Seibt, M. , Baumann, F. H. and Kim, Y. O. (1993) Analysis of the information in transmission electron micrograph, in Proc. Microsc. Semicond. Mater. Conf., edited by A. G. Cullis, A. E. Staton-Bevan and J. L. Hutchison (Oxford, 5-8 April 1993), Inst. Conf. Ser. No. 134: 1-10.

[I-75] Ikarashi, M. , Tatsumi, T. and Ishida, K. Jpn. J. Appl. Phys. 33 (1994) 1228.

[I-76] Krivanek, O. L., Isoda, S, and Kobayashi, K. Philos. mag. 36 (1977) 931-940.

[I-77] Bourret, A. and Desseaux, J. Philos. Mag. A39(1979) 405.

[I-78] Sinclair, R. , Ponce, F. A., Yamashita, T., Smith, D. J., Camp, R. A., Freeman, L. A., Erasmus, S. J., Nixon, W. C., Smith, K. C. A and Catto, C. J. D. Nature 298(1982) 127.

[I-79] R. F. Egerton, in *Electron Energy-Loss Spectroscopy in the Electron Microscope*, 2nd edition (Plenum, NewYork, 1986), p.1.

Chapter II

[II-1] D.J.H. Cockayne, J. Microsc. 98, (1973) 116

[II-2] J.M. Cowley and A.F. Moodie, Acta Cryst. 10, (1957)609

[II-3] P. Goodman and A.F. Moodie, Acta Cryst. A30, (1974)280

[II-4] for example, J.M. Cowley, Diffraction Physics (2nd Ed.), North-Holland Pub. Com.(1981)

[II-5] p.521 in ref.[I-4]

[II-6] M.Tanaka, K.Tsuda, M.Terauchi, K.Tsuno, T.Kaneyama, T.Honda and M.Ishida, J. Microscocpy, 194, (1999) 219-227

[II-7] K.Tsuda and M.Tanaka, Acta Cryst., A55(5), (1999)939

[II-8] N. Mori, T. Oikawa, Y. Harada and J. Miyahara, J. Electron Microsc. 39, (1990) 433

[II-9] R. F. Egerton, in *Electron Energy-Loss Spectroscopy in the Electron Microscope*, 2nd   edition (Plenum, NewYork, 1986), p. 154.

Chapter III

[III-1] For instance, S. S. Nandra and P. J. Grundy, J. Phys. 7, (1977)207 .

[III-2] P. A. Doyle,and P. S. Turner, Acta Cryst. A 24, (1968)390 .

[III-3] J. S. Custer, M. O. Thompson, D. J. Eaglesham, D. C. Jacobson, and J. M. Poate, J. Mater. Res. 8, (1993)820.

[III-4] L. Ley, in *The Physics of Hydrogenated Amorphous Silicon II ; Electronic and vibrational properties*, edited by J. D. Joannopoulos and G. Lucovsky, Topics in Applied Physics Vol. 56 (Springer-Verlag, Berlin, 1984), p. 68.

[III-5] K. Zellama, P. Germain, S. Squelard, and J. C. Bourfoin, J. Appl. Phys. 50, (1979)695.

[III-6] Y. Masaki, P. G. LeComber, and A. G. Fitzgerald, J. Appl. Phys. 74, (1993)129.

[III-7] C. C. Ahn, and O. L. Krivanek, in *EELS Atlas* (Gatan Inc., Pennsylvania, 1983).

[III-8] I. Berbezier, J. M. Martin, C. Bernardi, and J. Derrien, Appl. Surf. Sci. 102, (1996)417

[III-9] p. 301 in ref.[II-9]

[III-10] K. Tsuji and S. Minomura, J. de Phys., C4, 42 (1981) C4-233

[III-11] P. R. Okamoto, N. Q. Lam and L. E. Rehn, Solid State Physics.

[III-12] H. Mori, in Current Topics in Amorphous Materials, edited by Y.Sakurai, Y. Hamakawa, T. Masumoto, K. Shirae and K. Suzuki, 1993, p. 120, Elsevier Science Publishers B. V.

[III-13] N. Arai, S. Takeda and M. Kohyama, Phys. Rev. Lett. 78, (1997) 4265.

[III-14] S. Takeda, Jpn. J. Appl. Phys. 30, (1991)L639 .

[III-15] R. Perez, M. C. Payne and A. D. Simpson, Phys. Rev. Lett. 75, (1995) 4748.

[III-16] D. J. Chadi and K. J. Chang, Phys. Rev. B38, (1988)1523.

[III-17] M. J. Caturla, T. D. de la Rubia, and G. H. Gilmer, J. Appl. Phys. 77, (1995)3121.

[III-18] D. Cherns, Surf. Sci. 90, (1979)336.

Chapter IV

[IV-1] J. Bourgoin and J.W. Corbett, Inst. Phys. Conf. Ser. 23 (1975) 149

[IV-2] M. Kiritani, "Fundamentals of radiation damage" (1993) North-Holland, p.220.

Chapter V

[V-1] J.D. Joannopoulos, R.D. Meade and J.N. Winn, "Photonic Crystals" (1992) Princeton University Press.

[V-2] V.V. Poborchii, T.Tada and T.Kanayama, Appl. Phys. Lett. 75, (1999)3276

[V-3] Hanaizumi, Y. Ohtera, T.Sato, and S.Kawakami, Appl. Phys. Lett. 74,(1999) 777

[V-4] J. Leng, etal, J. Vac. Sci. Technol. A 16,(1998) 1654

light ion implantation   heavy ion implantation

E E

E_{trans} E_{trans}

homogeneous amorphization[*1]   heterogeneous amorphization[*2]
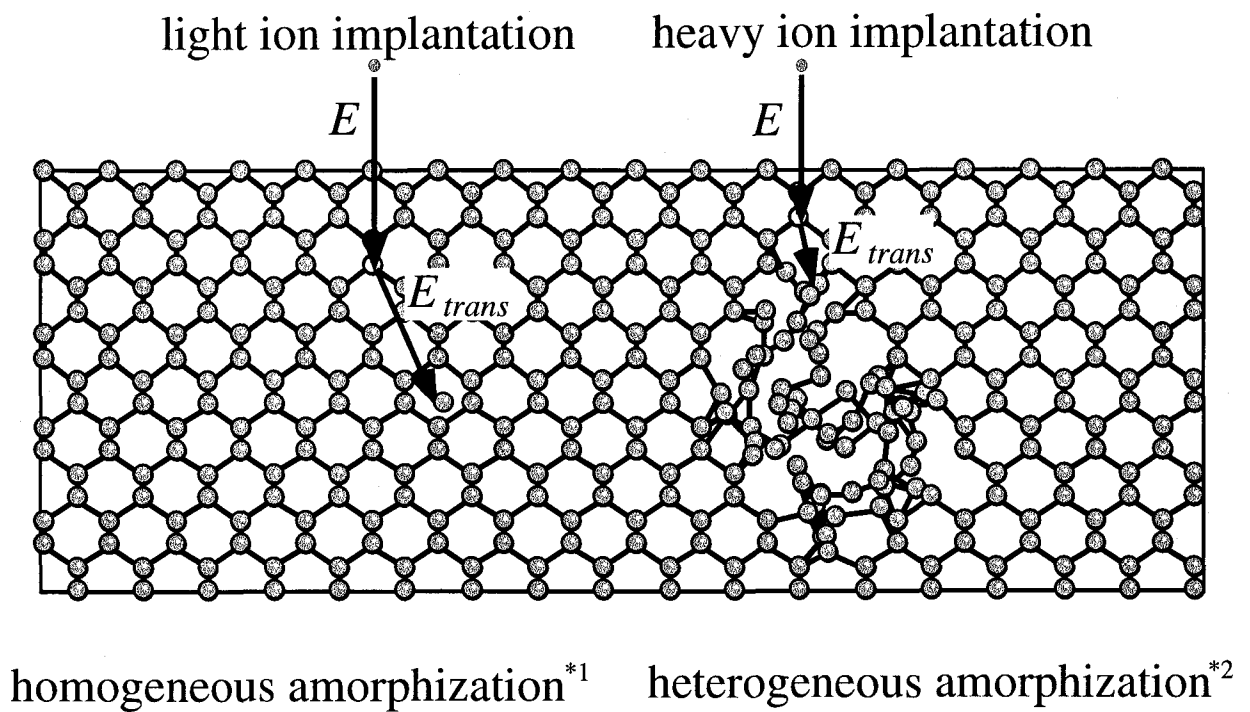
*1) After O.W.Holland,et al [I-26]
*2) After F.F Morehead,et al [I-25]

Fig.I-1   Schematic diagram of two amorphization mechanisms in charged particle irradiation.

Method	Conductivity	Structure	Reference
Vacuum evaporation	Semiconducting	4 (3,5) fold coordinate	[I-5](1989)
Sputtering	Semiconducting	4 (3,5) fold coordinate	[I-6](1988)
CVD	Semiconducting	4 (3,5) fold coordinate	[I-7](1980)

Table.I-1.   List of various methods for producing a-Si

Method	Conductivity	Structure	Reference
Laser melting	Metalic	6 fold coordinate	[I-21](1982)
Indentation	Metalic	6 fold coordinate	[I-19](1988)
Surface scratch	Semiconducting	4 (3,5) fold coordinate	[I-18](1992)
Ion implantation	Semiconducting	4 (3,5) fold coordinate	[I-20](1989)
Electron irradiation	Semiconducting	4 (3,5) fold coordinate	Present study (preliminary reports[I-22, 23,24])

Table.I-2.   List of various methods for amorphizing c-Si

	charge state	symmetry	method	creation condition	rotation temparature	E,eV	anneal temparature	E,eV	refer-ences
I		<100> main axis	ESR	n type (Pdope) 46MeV⁻, e-irrad⁻. 20K			170K	?	[I-1]
	I⁺<100>	orthorhombic <100>split	Infrared absorption	p-type(B dope) 100keV B⁺,RT	340K	0.70	370K	0.85	[I-38, 39,40]
	I⁰<100>	tetragonal <100>split		220℃	450K	0.92	570K	1.50	
	?	bond centre +Hsite mixture	BS	p-type(B dope) 2 MeV, He, RT					[I-41]
I₂	I_{y2}⁺	D_{2d}(315K) <100> di-interstitialcy	ESR	⁰n_f,d irradiation	360K	0.6 ±0.2	~420K		[I-42, 43]
		C₂ or C_{1h} (at 200K)							[I-43]
	I₂⁺	D_{2d} <100> main axis	ESR ENDOR	only in B dope p type ⁰n_f irradiation after aneal at	≧670K	2.3			[I-45, 46,47]
		two I at a distance of 9Å I(<100>split)	ESR	50~175℃ ⁰n_f, RT			430K		[I-48]
		<100> main axis	ESR	ion implantation					[I-49]
I_n		(113) planar	HRTEM	e⁻ irradiation					[I-61]

Table.I-3   Summary of the previous studies about interstitials in Si

	charge state	symmetry	method	creation condition	rotation temparature	E,eV	anneal temparature	E,eV	references
V	V^{--}	(C_{2v})					70K	0.18 ±0.02	[I-1,50, 51,52]
	V^-	C_{2v}	ESR		~20K ~26.8K	0.0081			
	V^0	D_{2d}					170K	0.33 ±0.03	
	V^+	D_{2d}	ESR		~2K	0.013			
V_2	V_2^-	C_{2h}	ESR	As irrad. or n type ~70K	370~ 470K	1.3	620K	1.3	[I-51,53, 54,55,56]
	V_2^0								
	V_2^+	C_{2h}	ESR						
	V_2^-	D_{3d}	positron annihilation	p-dope 15MeV e⁻ RT					[I-62]
V_3	V_3^-	(110) planar	ESR	100~250℃ 170℃	500K		520K (250℃)		[I-48,56]
V_4	V_4^0	C_{2h} (111) planar	ESR	?	410K		440K		[I-42,56, 57]
	V_4^-		ESR						[I-58]
	V_4^-	C_{3v} (111) planar	ESR	170℃	500K		620K		[I-48,56]
	V_4^+?	non planar	ESR	~170℃			570K		[I-56]
V_5	V_5^-	C_{1h} non planar	ESR	~170℃	500K		~720K		[I-59,57, 60]

Table.I-4   Summary of the previous studies about vacancies in Si
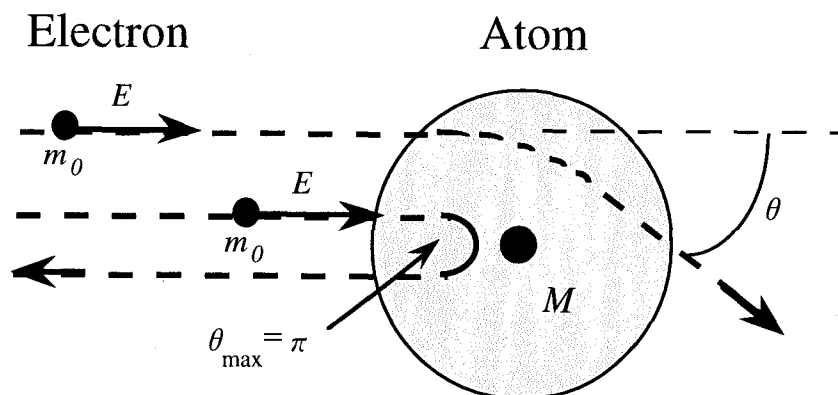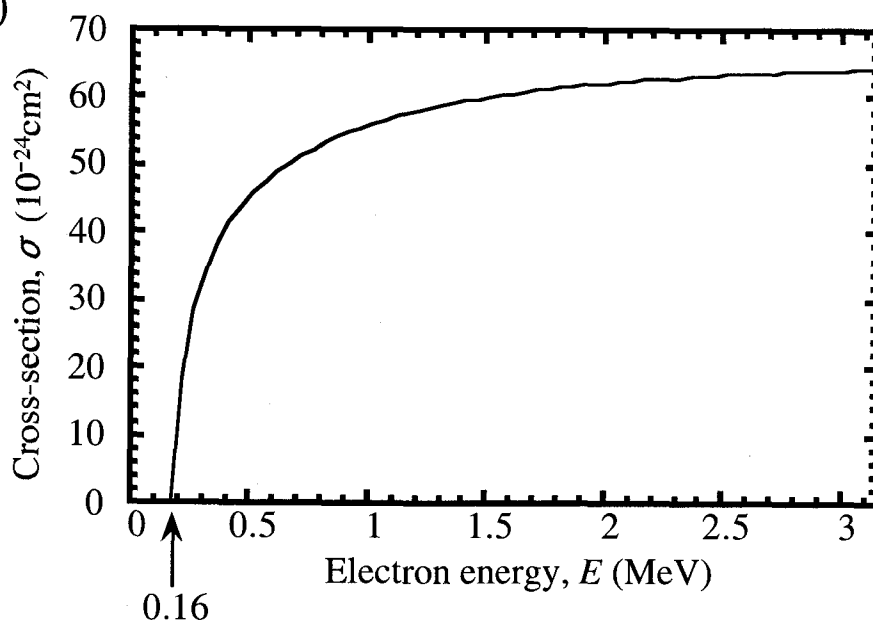
Fig.I-2　(a) A collision between an electron of mass m_0 and an atom of mass M.　(b) Estimated cross-section σ for the displacement of Si atoms.
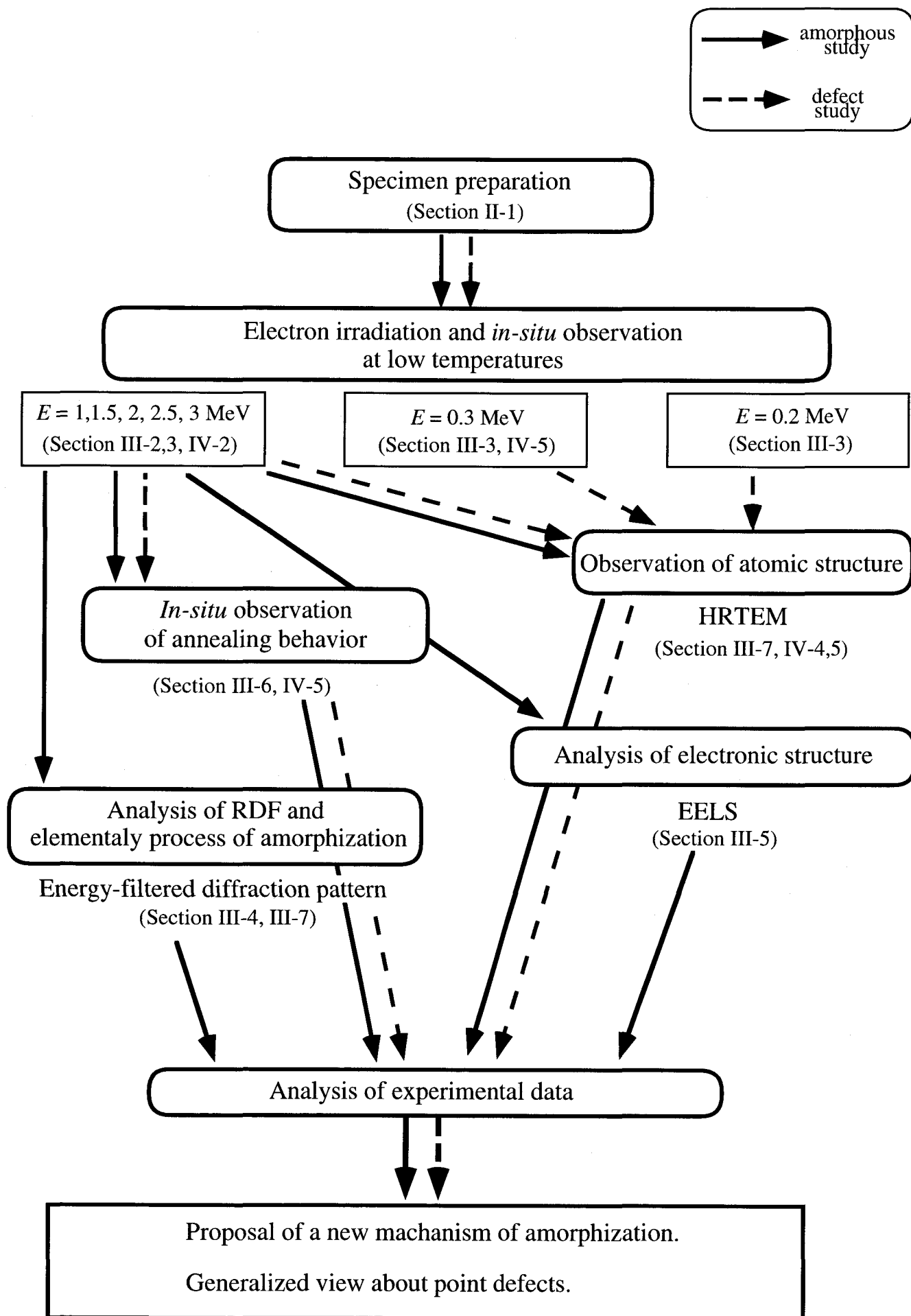
Fig.II-1 Procedure of experiments

Purpose	Instrument		Electron energy in operation	Specimen temperature	Spatial resolution
Electron irradiation and *in-situ* observation at low temperatures	Hitachi H-3000 (Fig.II-3)	in UHVEM center, Osaka University	1, 1.5, 2, 2.5, 3 MeV	25 K-115 K	0.14 nm
	JEM-3000HFI (Fig.II-4)	in Biomolecular Engineering Research Institute	0.3 MeV	4.2 K	0.14 nm
In-situ observation of annealing behavior	JEM2000EX	in our laboratory	0.2 MeV	15 K	0.27 nm
				R.T. - 800°C	
Observation of atomic structure by HRTEM	JEM2010	in our laboratory	0.2 MeV	R.T.	0.19 nm
Analysis of RDF and elementary process of amophization by energy-filtered diffraction patterns	JEM2010FEF (Fig.II-8)	in Tanaka Lab.,Research Institute for Scientific Measurements, Tohoku University	0.1 MeV	R.T.	0.19 nm
Analysis of electronic structure by EELS	JEM3000F	in Osaka National Research Institute	0.3 MeV	R.T.	0.17 nm

Table.II-1 List of instruments used in this study

(a)

silicon <110> wafer

↓ cut the wafer into a form of a disk

<110>

0.27mm

3mm

↓ ultrasonic drilling
(the hole 0.1mm in depth)
(cross section)

↓ dimpling on the other side of t
(cross section)

about 100 μm

chemical etching
(HNO₃ : HF≈6:1)
(cross section)

hole   hole

(b)

0.12mm   [1̄11]   [11̄0]   0.8mm

guide line
for cleavage   0.5mm

Si (110) wafer   0.12mm

cleavage of the sample   paste on a Mo mesh

Mo mesh

set the sample on the Mo mesh   0.12mm

[111]   0.4mm

35   0.6mm   [110]

3mm

Fig.II-2   Process of making TEM samples.
(a) The way by mechanical and chemical etching.
(b) The way by cleavage.
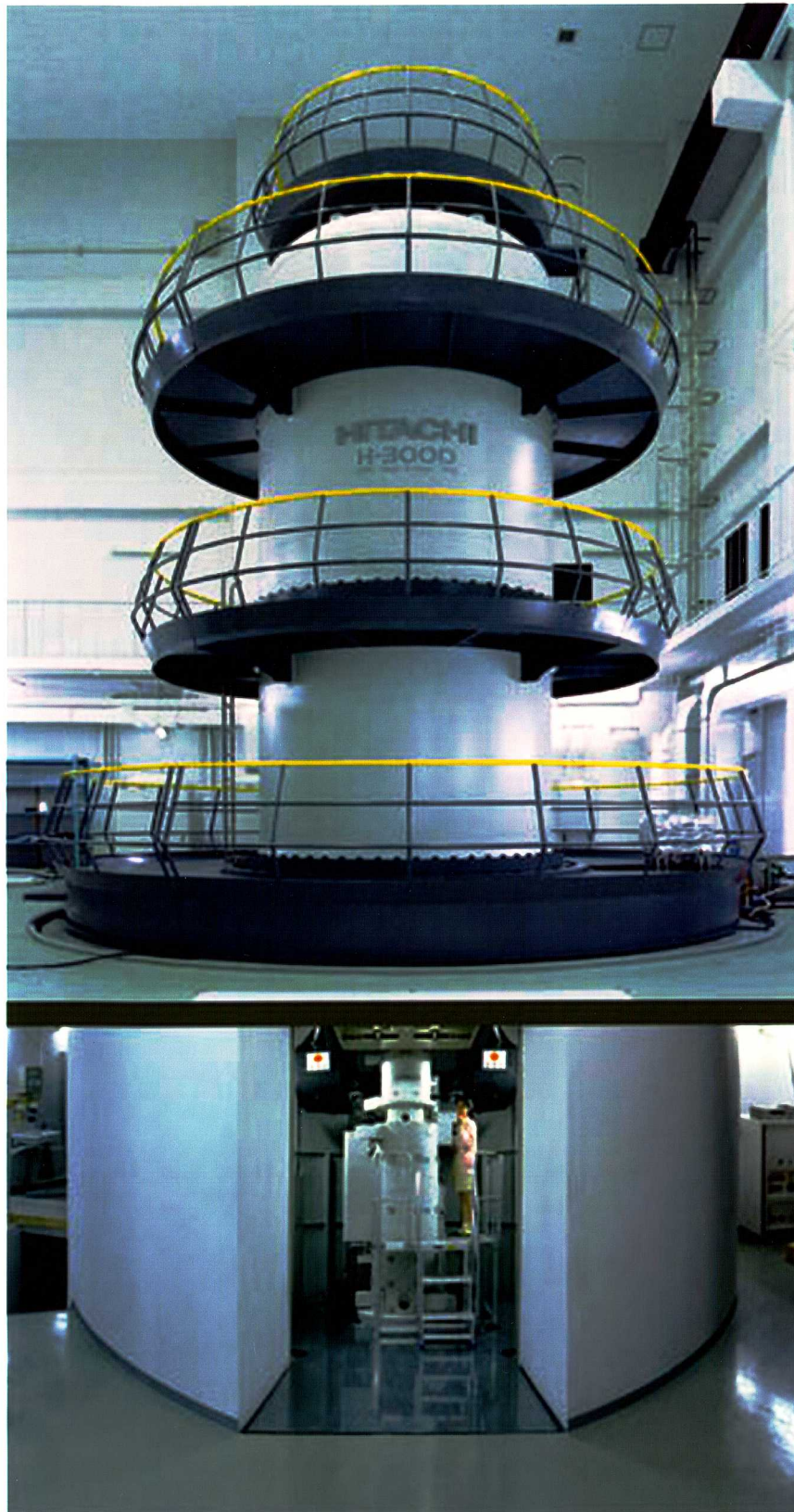
Fig.II-3   3MV HVEM(Hitachi H-3000) at the ultrahigh
voltage electron microscope center, Osaka University.
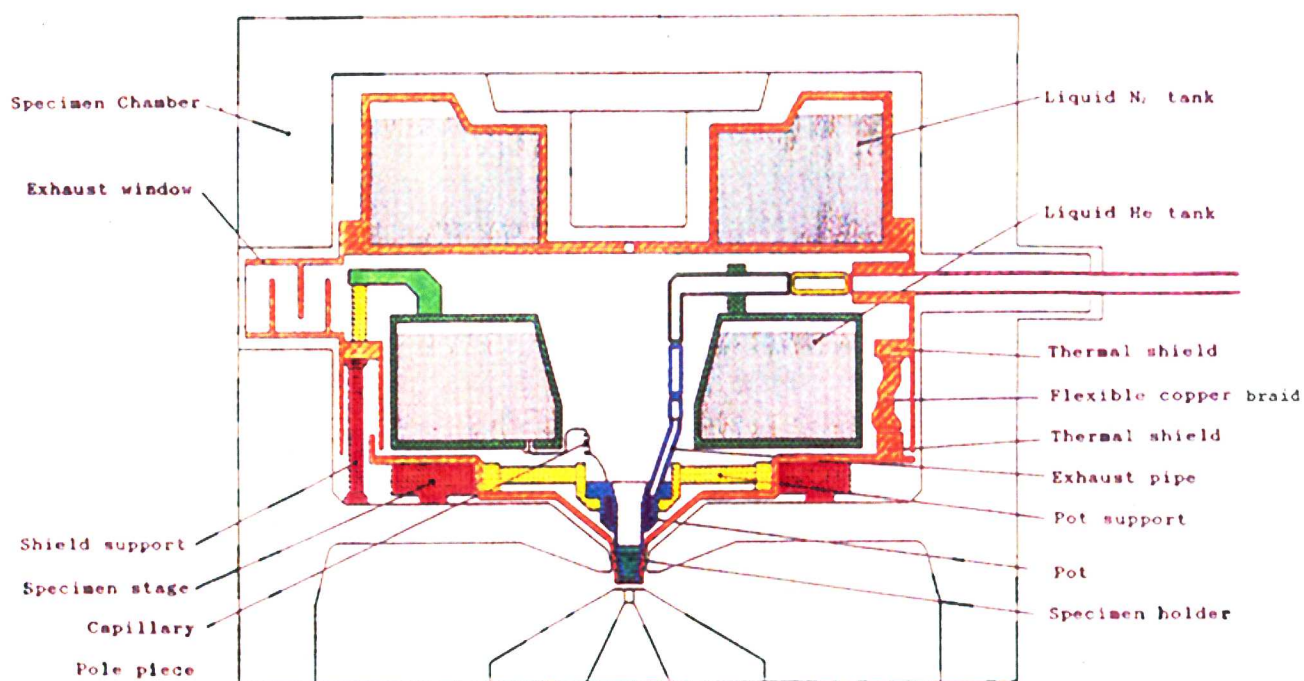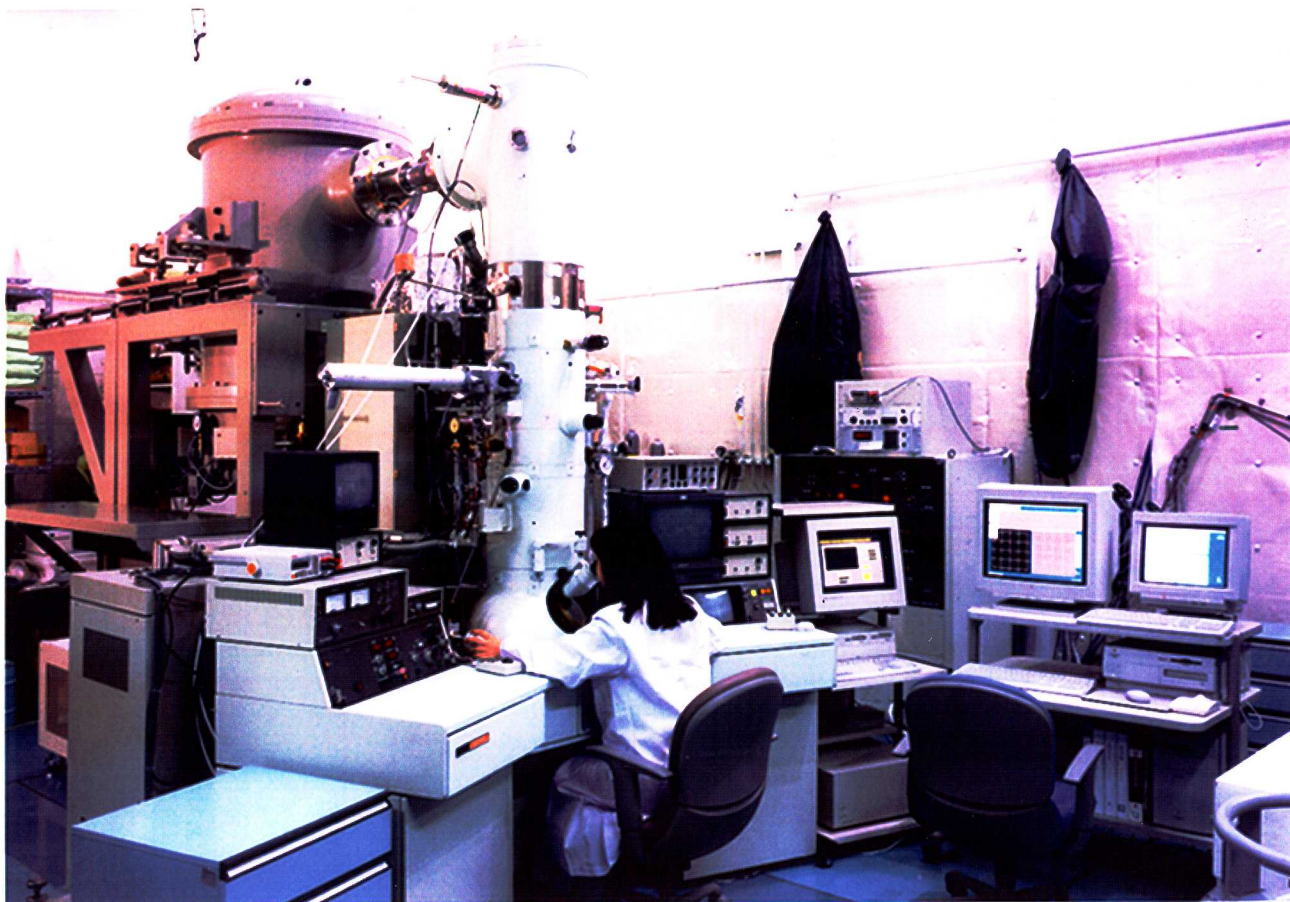
Fig.II-4   0.3 MV TEM (JEM-3000HFI) equipped with a top-entry type liquid-helium cooling stage and field emission gun of Biomolecular Engineering Research Institute.
(a)General view. (b)Cooling system in the column.
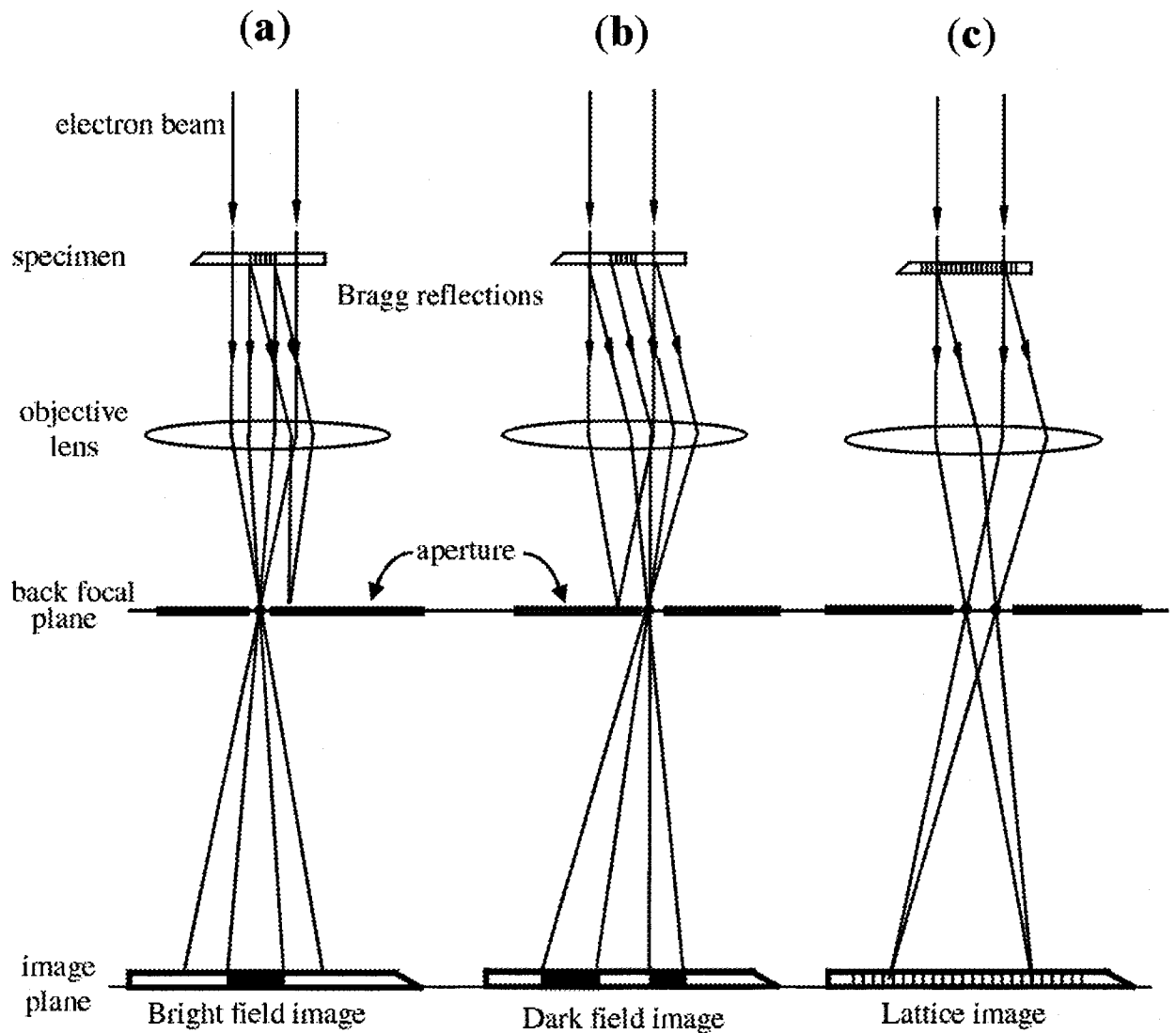
Fig.II-5 Ray paths in the transmission electron microscope on imaging:

(a) Bright field image by diffraction contrast.

(b) Dark field image.

(c) Lattice image by interforence of two beams.

(a)
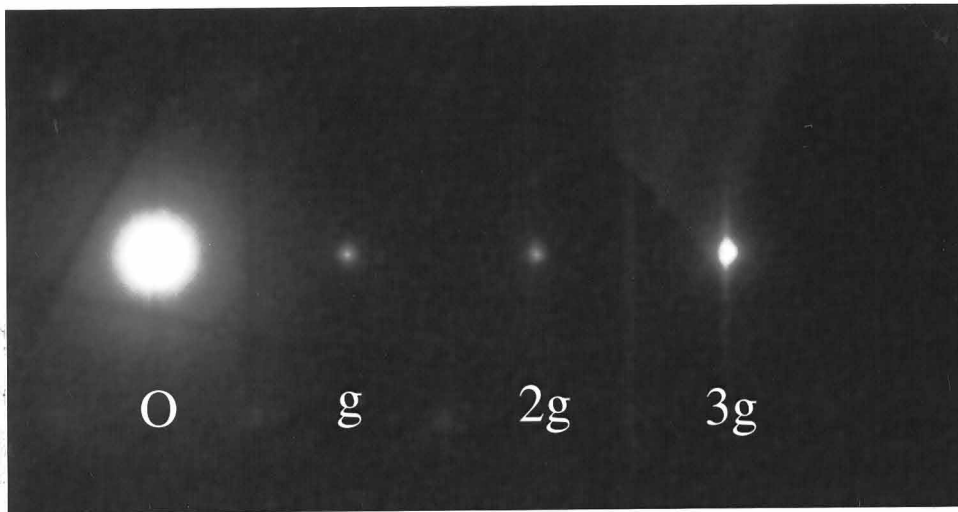
(b)
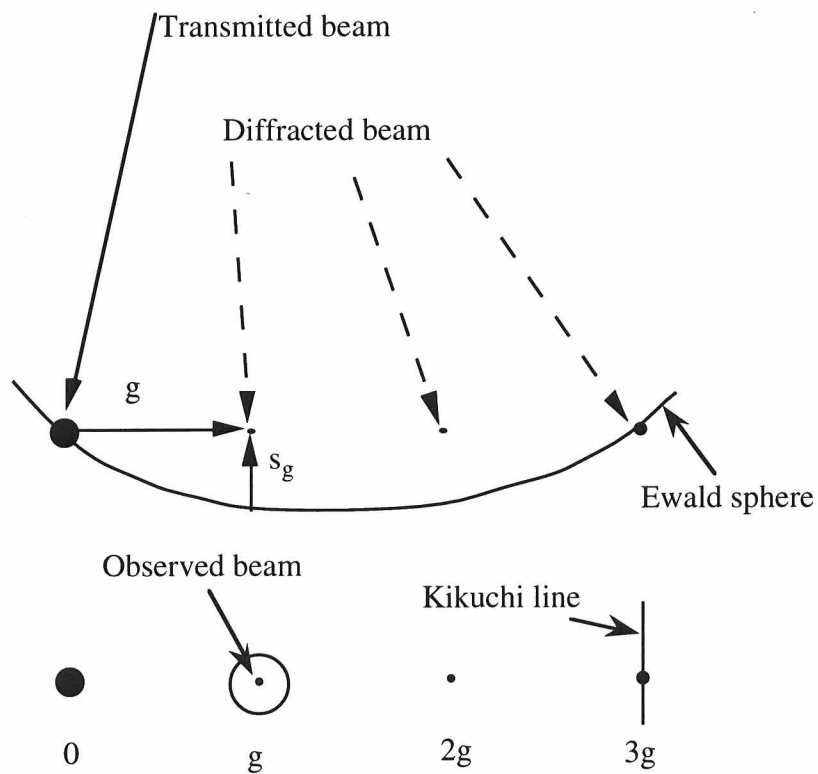
Fig. II-6　(a) Electron diffraction pattern in weak-beam diffraction condition, and (b) corresponding schematic representation.

Recording experimental HRTEM images

Experimental parameters ———————————————————

Electron energy : E

Spherical abberation constant : C_s

Defocus spread caused by chromatic abberation : δ

Beam divergence semi angle : α

Objective aperture size

Unknown experimental parameters ————

Defocus : Δf

Thickness : t

(Section IV-8)

Determination of the values of defocus, Δf.

Fourier transform of HRTEM images.

input

Determination of thickness, t.

Comparison between the experimental and
the simulated images of perfect crystals.

Proposing of defect structure models

(Section IV-7)

input

Producing supercells for simulations

(Section IV-8)

No

Image simulations with the supercells
at various values of defocus and thickness

(Section IV-8)

The results reproduce general features in observed images ?

Yes

Detailed simulation

Refinement of the defect structures

(Section IV-10)

Fig.II-7 Procedure of HRTEM image analysis

Field Emission
Gun

Ω-filter

(a)

(b)
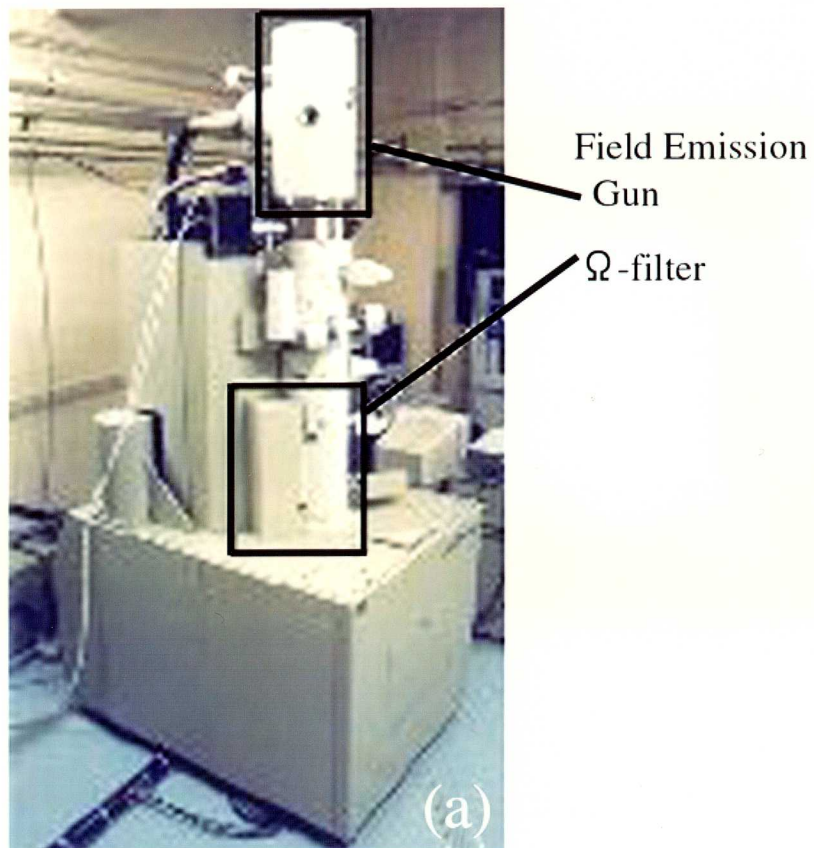
Fig.II-8   Energy-filtering TEM (JEM2010FEF)
at Tanaka Lab.,Research Institute for Scientific
Measurements,Tohoku University [II-5, 6]
(a)General view of energy-filtering TEM
(b)Control part which is separated from the column
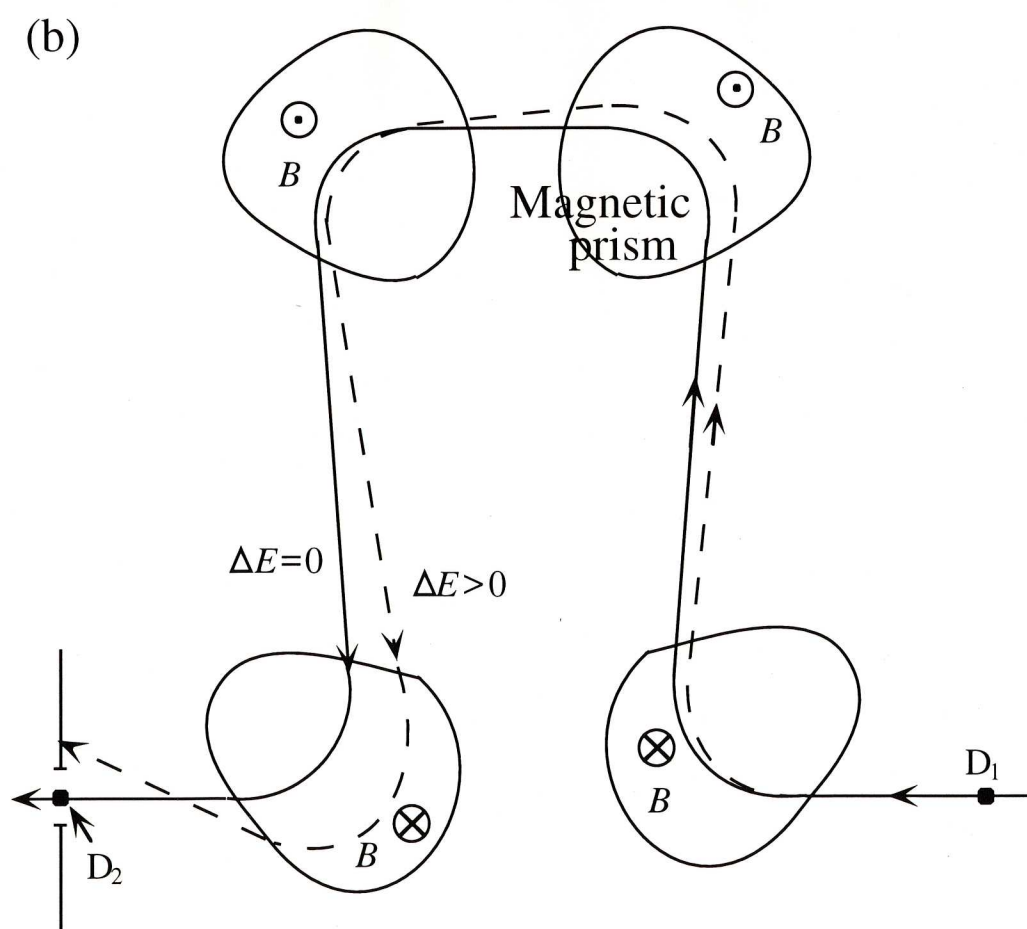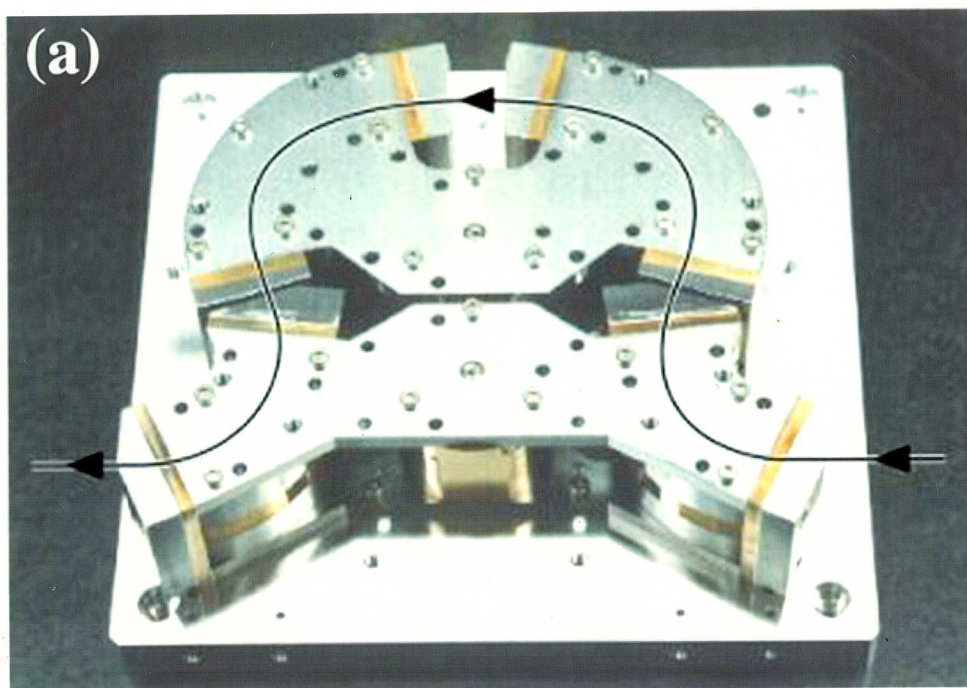
Fig.II-9   (a) General view of an omega-type energy filter. (b) Optics
of an omega-type energy filter. The plane through D2 contains an
energy-dispersed diffraction patter.
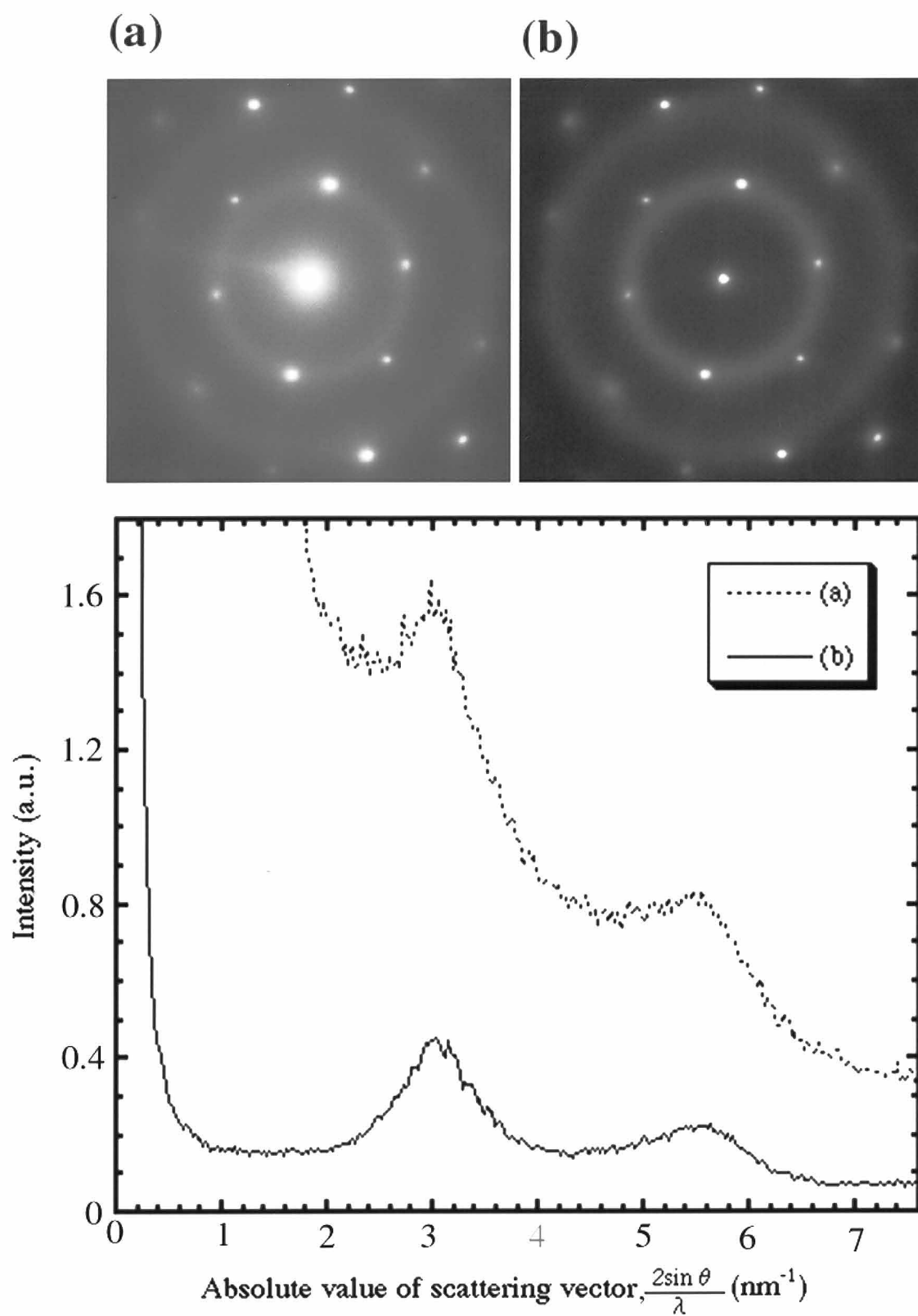
Fig.II-10 Diffraction patterns obtained from an irradiated area
(a) without and (b) with the energy filter, respectively. The halo
intensity profile from (a) includes large inelastic background.
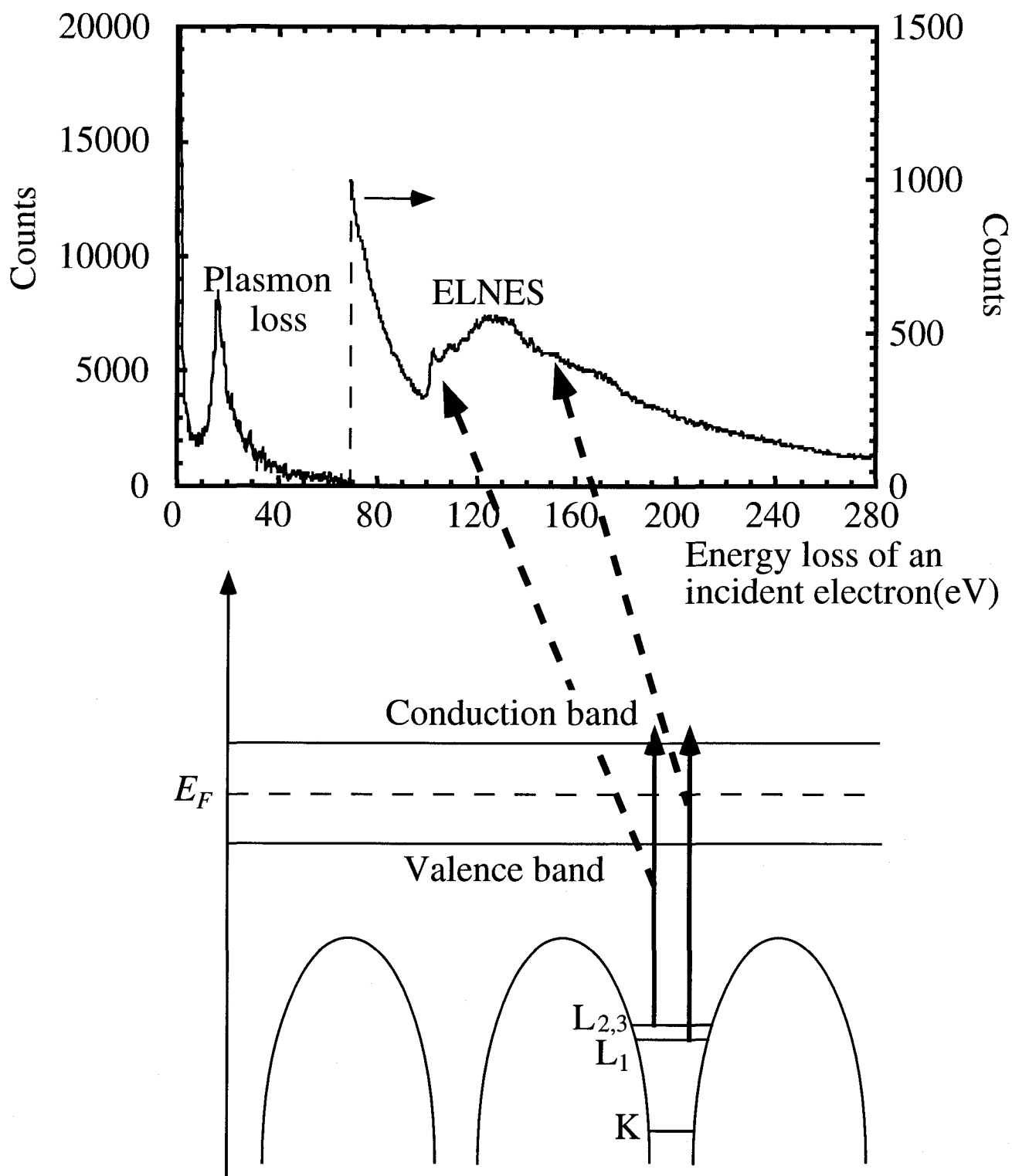
Fig.II-11   Energy-level diagram of Si and a typical loss spectrum recorded from a thin c-Si film. E_F is the Fermi level. The edges caused by excitation of inner shell electrons into the conduction band (ELNES) are located at about 100 eV and 150 eV. The former is coused by $L_{2,3}$ electrons and the latter, L_1 electrons, respectively.
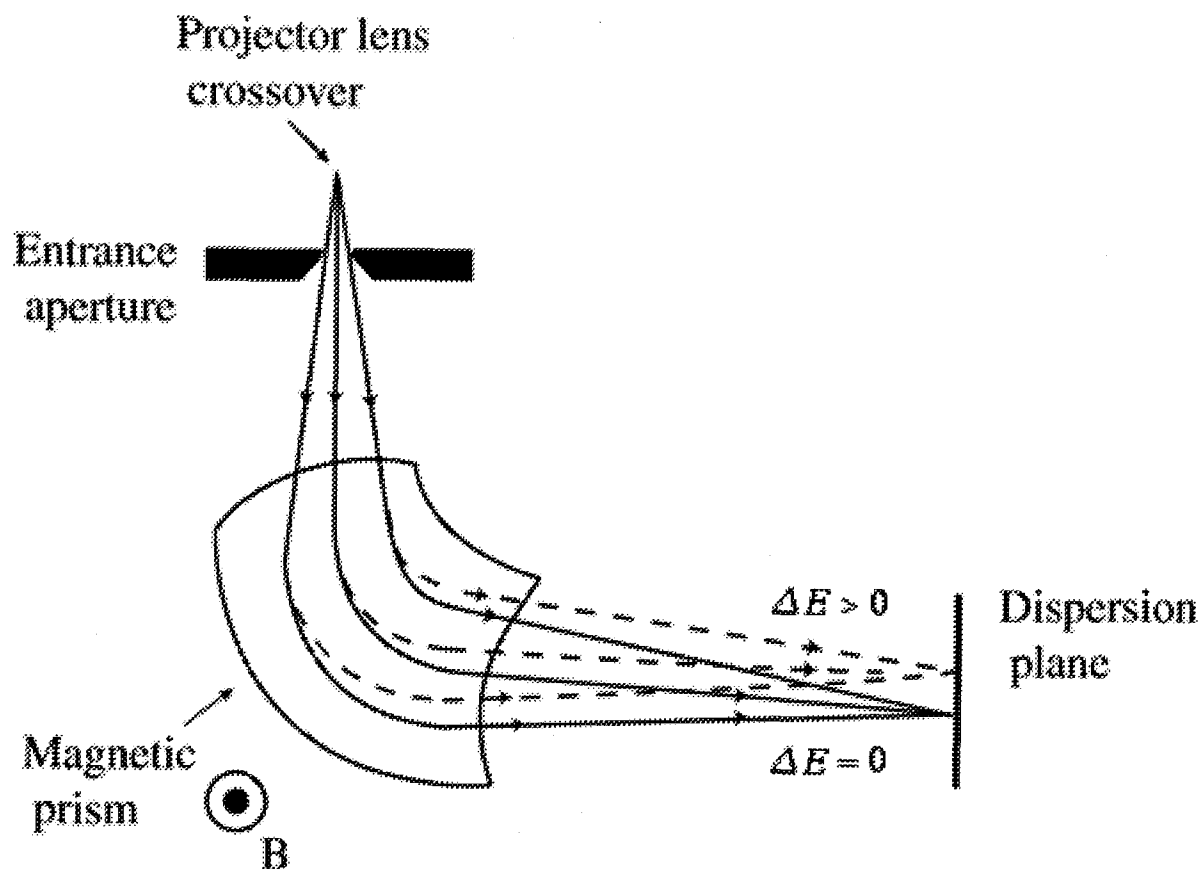
Fig.II-12 Focusing and dispersive properties of a magnetic prism.
The trajectories of electrons which have lost energy are indicated
by dashed lines.

Characterization	Method of characterization	Related section
Atomic structure	RDF	III-4
Electronic structure	EELS	III-5
Thermal stability	Annealing	III-6
Elementary process	SAD	III-7
Structure of an *a-c* interface	HRTEM	III-7

Table.III-1   Experimental techniques to characterize electron-irradiation-induced *a*-Si.
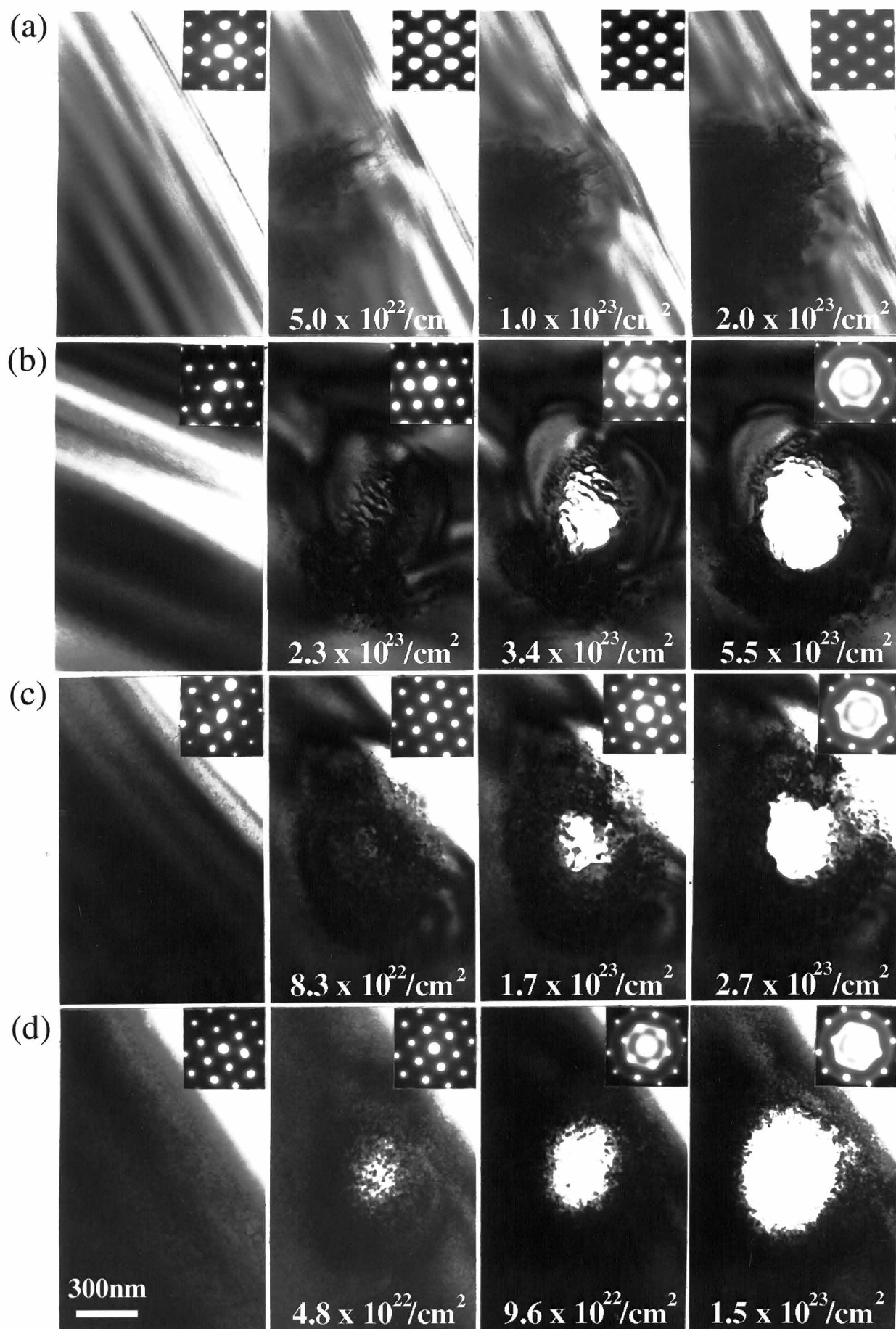
Fig.III-1 *In-situ* TEM observation of amorphization processes as a function of irradiation temperature. (a) room temperature, (b) 94 K, (c) 60K, (d) 25 K. The dose,D is shown in each image. The insets are the corresponding electron diffraction patterns. (E = 2.0 MeV)
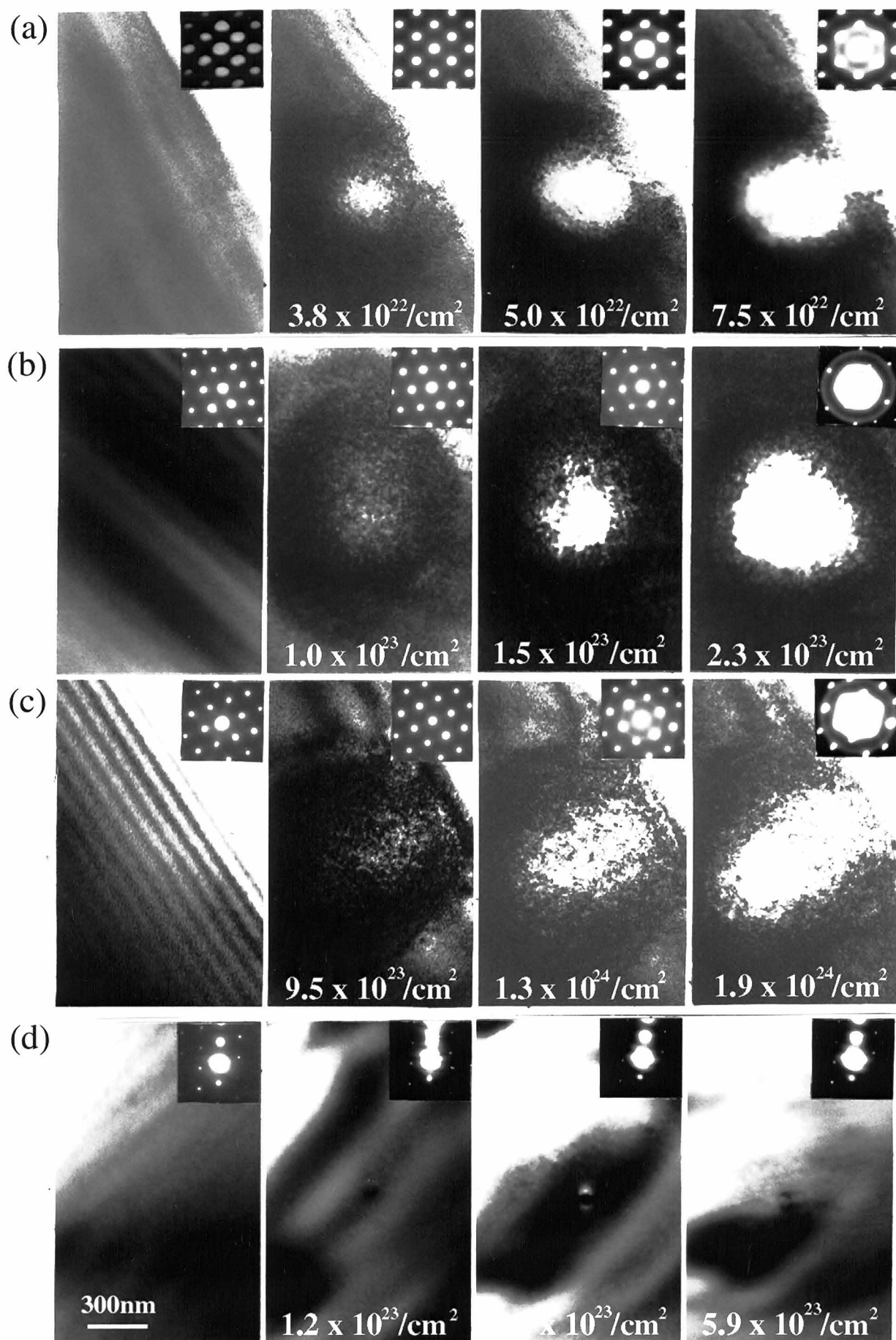
Fig.III-2   *In-situ* TEM observation of amorphization processes as a function of irradiation energy, *E*.   (a) 2.0 MeV, (b) 1.5 MeV, (c) 1.0 MeV, (d) 0.2 MeV.   (*T* =15 - 25 K)
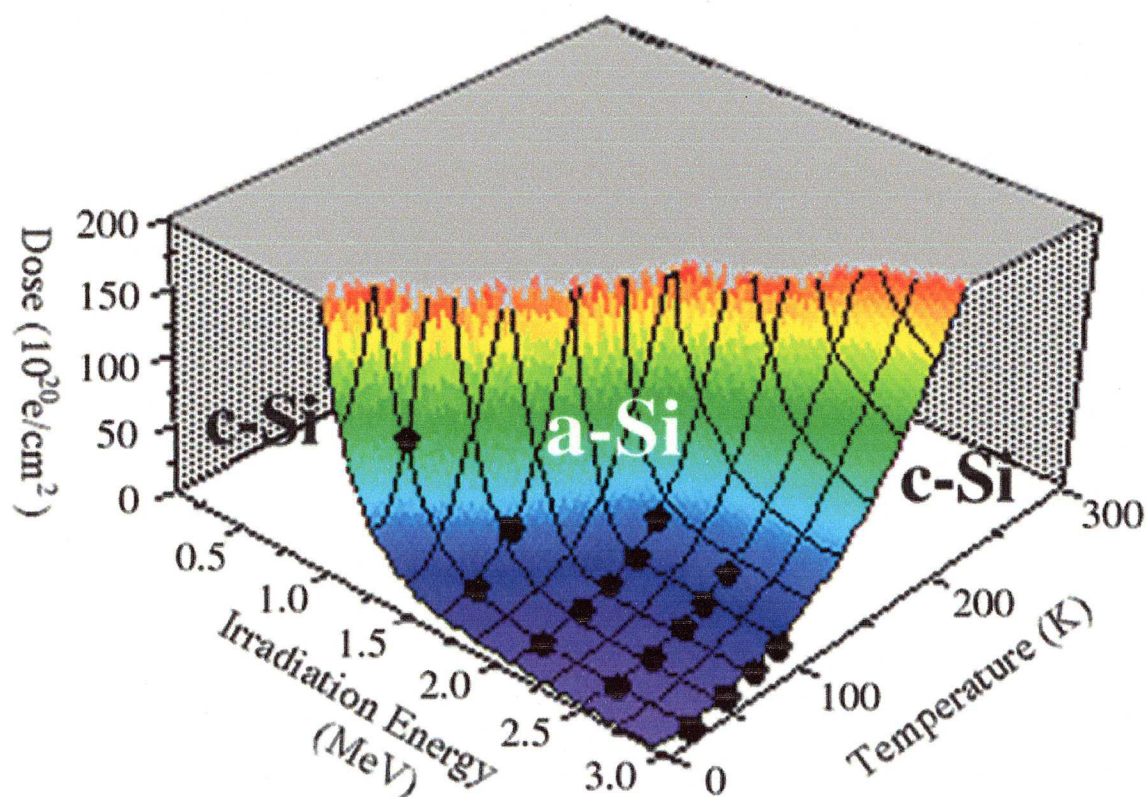
Fig.III-3   Irradiation conditions needed for amorphization expressed by *E*, *T*, and *D*. Black dots on the curved surface are the experimental data points. The curved surface is colored in order to remarkably indicate the value of *D*.
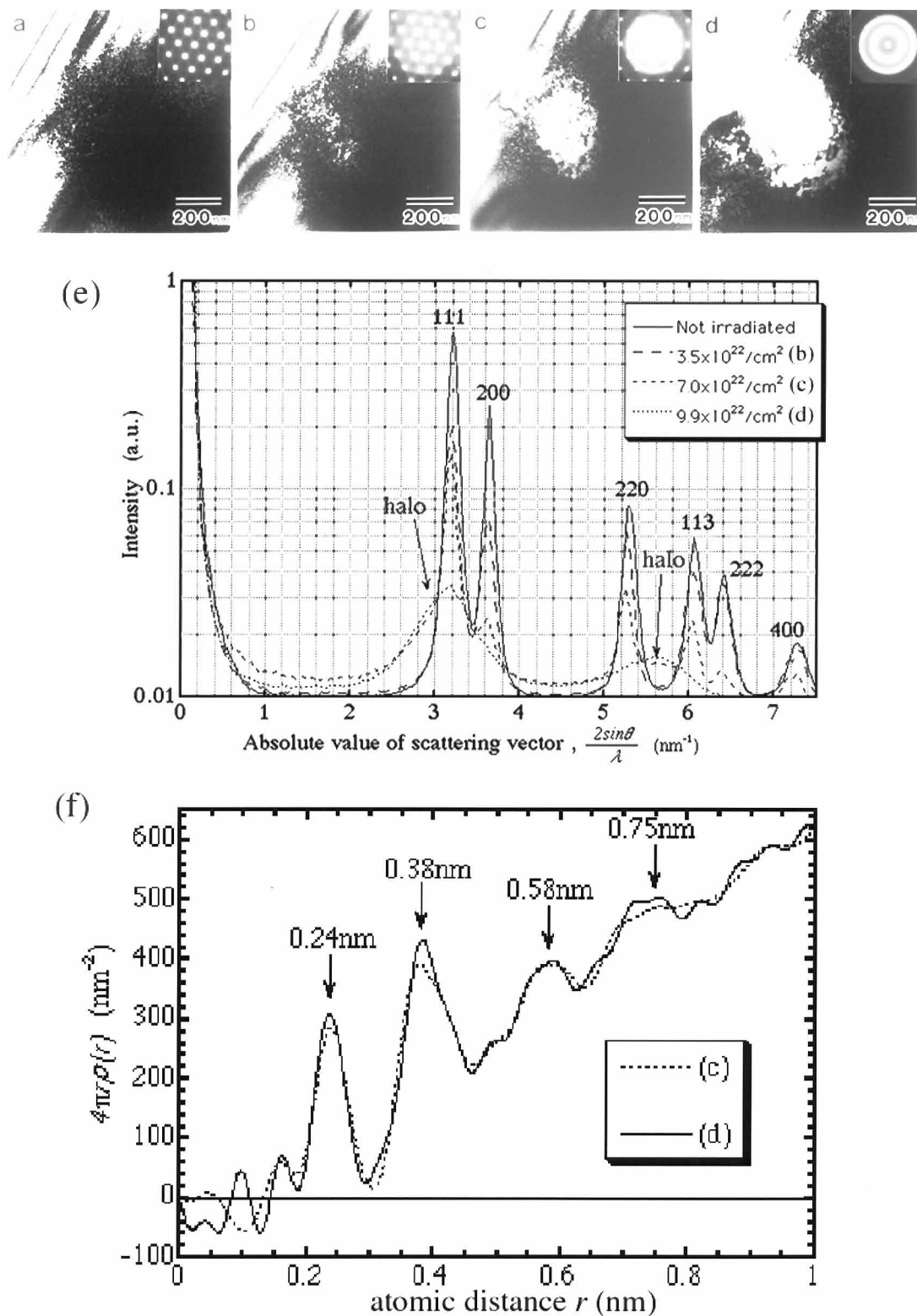
Fig.III-4 Electron-irradiated areas which received the doses of (a) $1.7 \times 10^{22} cm^2$, (b) $3.5 \times 10^{22} cm^2$, (c) $7.0 \times 10^{22} cm^2$ and (d) $9.9 \times 10^{22} cm^2$. The insets are the corresponding electron diffraction patterns, in which the selected area aperture covered the central area of about 250 nm in diameter. (e) Radial intensity profiles of electron diffraction of a non-irradiated area and the areas (b) to (d). (f) Radial distribution functions of a-Si from the intensity patterns (c) and (d).

Amorphization method	Peak positions in RDF (nm)			Plasmon peak	Recrystal-lization	Activation energy for SPE
	first	second	third			
Electron irradiation dose 7.0 x 10²² cm⁻¹ (partially amorphized)	0.235	0.382	0.588	16.3 eV	poly	2.6 eV
dose 9.9 x 10²² cm⁻¹ (fully amorphized)	0.238	0.378	0.581			
Si⁺ ion implantation	0.235	0.387	0.582 [III-3]	---	mono [III-3]	2.7 eV [III-3]
Vacuum evaporation	0.234	0.384	0.584 [I-20]	16.3 eV [III-4]	poly [III-5]	2.4 eV [III-5]
Sputtering	0.237	0.384	0.586 [I-6]	16.3 eV [III-4]	---	---
PECVD	0.236	0.383	0.584 [I-7]	16.0 eV [III-4]	poly [III-6]	3.1 eV [III-6]

Table.III-2   Comparison *a*-Si created by electron irradiation with *a*-Si by conventional techniques. Shaded data were determined in the present study. *a*-Si created by plasma enhanced chemical vapor deposition (PECVD) contains hydrogen. In the table, "---" means that there is no report.
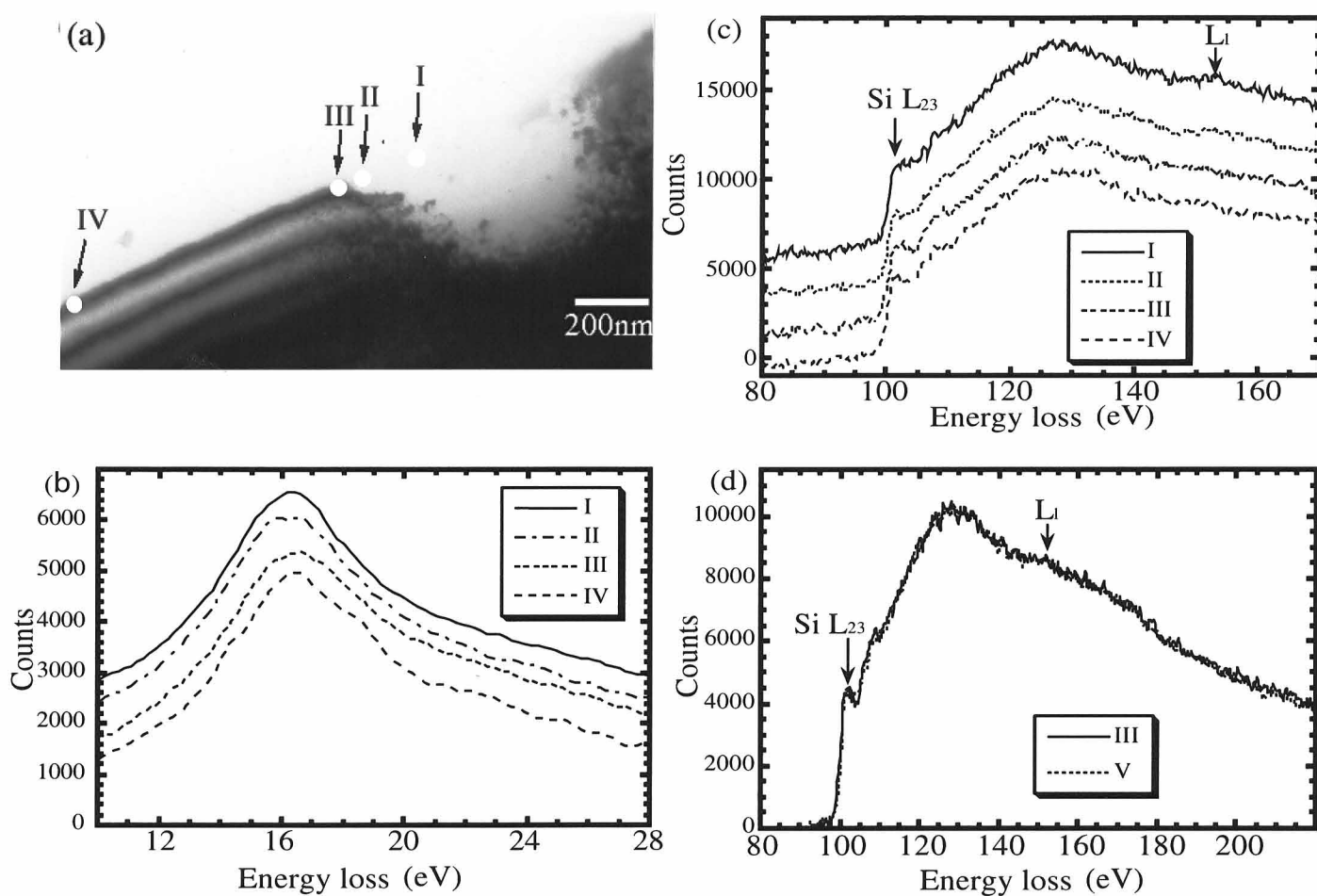
Fig.III-5   (a) The four area I, II, III, IV in which EELS measurements were performed. I: perfectly amorphized area. II: amorphous side of *a-c* interface. III: crystalline side of *a-c* interface. IV: crystalline area. (b) The Low Loss spectra and (c) ELNES from the areasI, II, III, IV in (a).   (d) Reproduction of ELNES from the area III by superposition of the spectrums from perfect crystal and from amorphous. The symbol V means the superposition of the spetra from the amorphous area I and from the crystalline area IV.
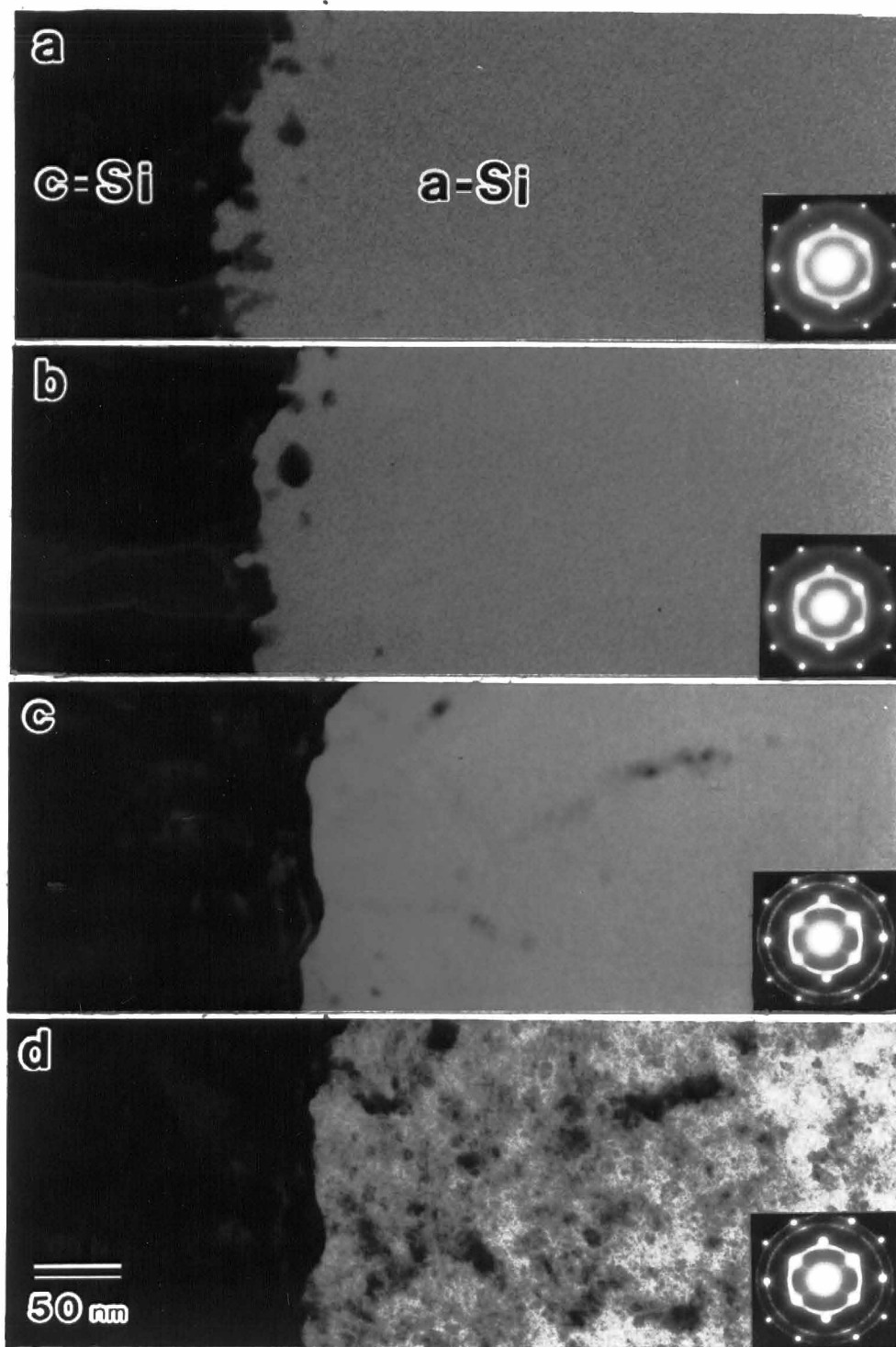
Fig.III-6   *In-situ* TEM observation of the recrystallizing process of *a*-Si. (a) As irradiated, (b) after annealing at 500 °C for 120 minutes, (c) after annealing at 550 °C for 35 minutes and (d) after annealing at 550 °C for 43 minutes.

Electron irradiation in HVEM

$E = 1.0, 1.5, 2.0, 2.5, 3.0$ MeV

$T = 25$ K

partly amorphized areas   fully amorphized areas

Measurements of halo ring intensity
in energy-filtered SAD patterns

halo intensity I (D, E, t)
from the partly amorphized areas

halo intensity I_0 (t)
from the fully amorphized areas

normalization about t (thickness)

Amorphized volume is equal to
sum of all cascade volumes

the graph of

$$n(D, E) = \rho \frac{I(D,E,t)}{I_0(t)}$$

$$n(D, E) = \int_{E_{th}}^{E_{max}(E)} n_c(E_{trans}) \cdot \sigma(E_{trans}, E)\rho D \cdot dE_{trans}$$

approximation

$n_c(E_{trans}) = \alpha(E_{trans} - 15eV) + 1$

$n_c(15eV) = 1$: creation of a Frenkel pair

(experimental values)

$$k_0(E) = \frac{\partial n(D,E)}{\partial D}$$

comparison

(theoretical values)

$$k_0(E) = \frac{\partial n(D,E)}{\partial D}$$

$$= \int_{E_{th}}^{E_{max}(E)} (\alpha(E_{trans} - 15eV) + 1) \cdot \sigma(E_{trans}, E)\rho \cdot dE_{trans}$$

fitting parameters

Determination of the fittest values

$E_{th} = E_{th}^0$ $\alpha = \alpha^0$

Determination of the number of atoms included
in the smallest cascade which contributes to amorphization.

$$n_{cth} = n(E_{th}^0) = \alpha^0(E_{th}^0 - 15eV) + 1$$

Fig.III-7   Determination of the number of atoms in the smallest cascade, n_{cth}
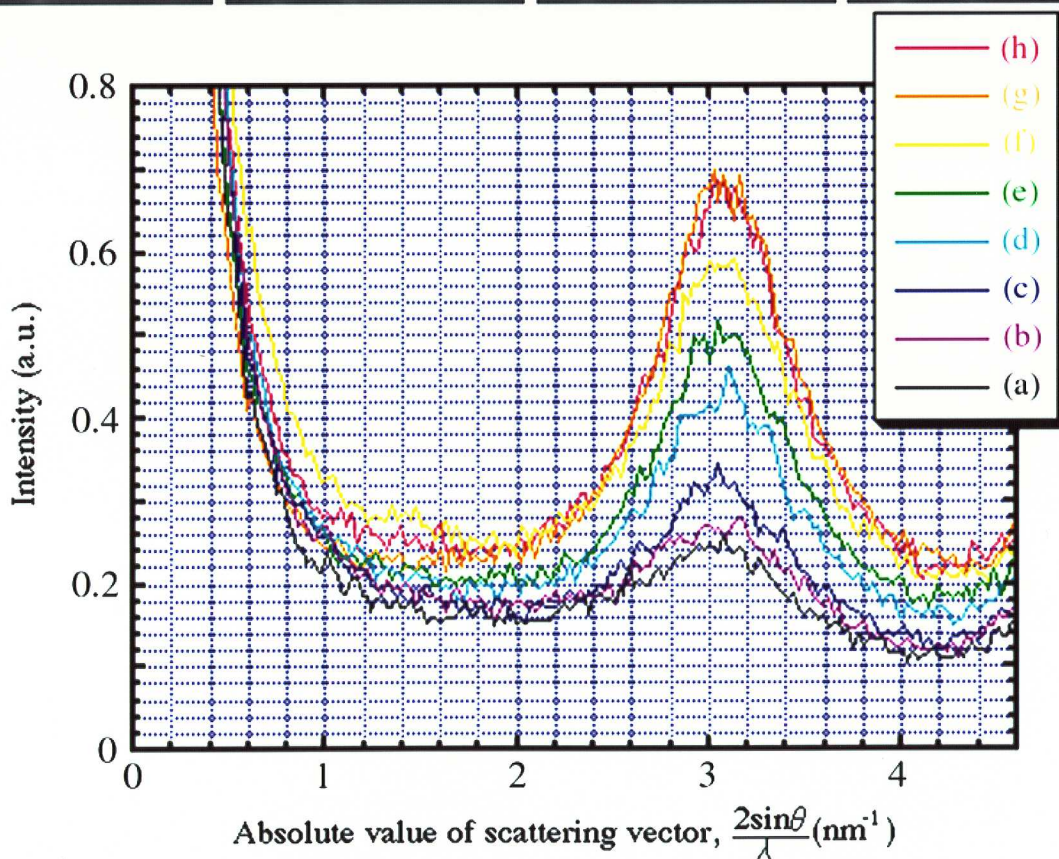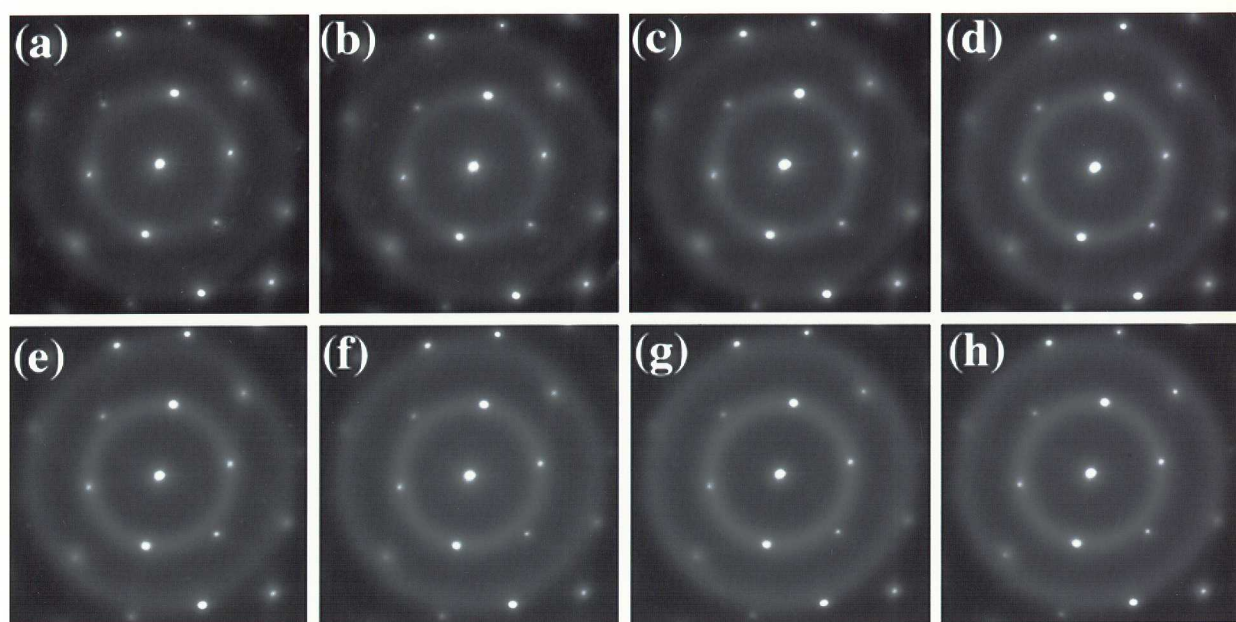
Fig. III-8   Dose dependence of halo intensity. The shown halo patterns are obtained from areas (a) - (h) which received the dose (a) 3.3×10^{21}/cm^2, (b) 6.6×10^{21}/cm^2, (c) 9.9×10^{21}/cm^2, (d) 1.3×10^{22}/cm^2, (e) 2.0×10^{22}/cm^2, (f) 2.7×10^{22}/cm^2, (g) 3.3×10^{22}/cm^2 and (h) 4.0×10^{22}/cm^2, respectively. We measured the first halo intensity in the radial profiles. (E=3 MeV, T=25 K)
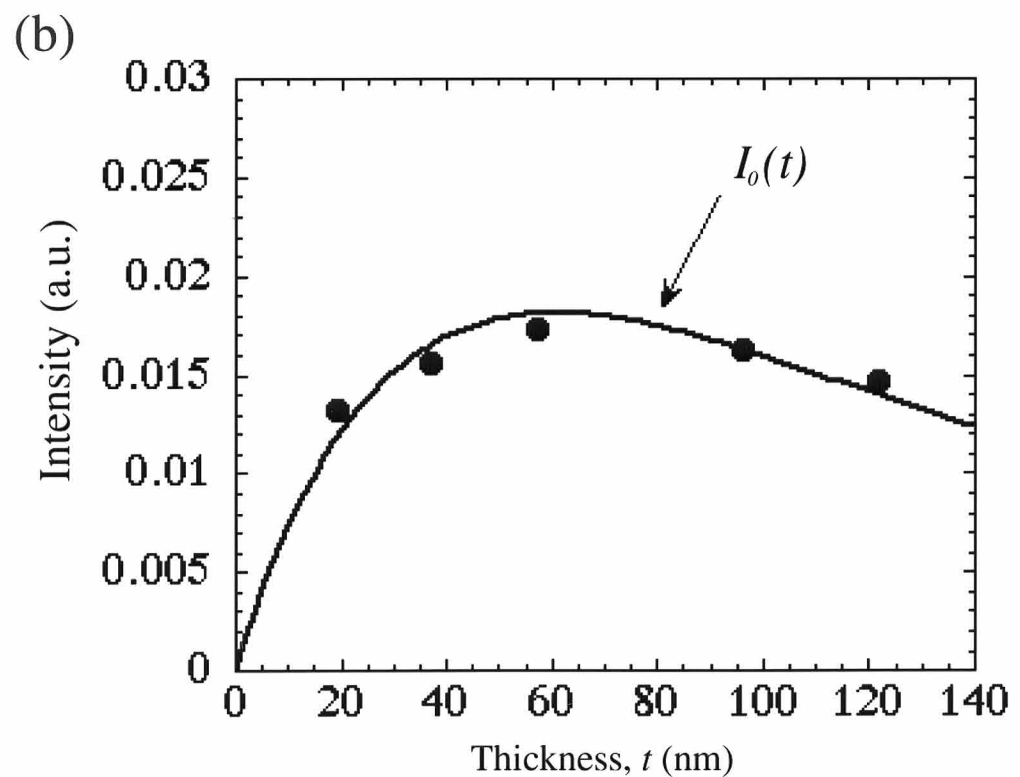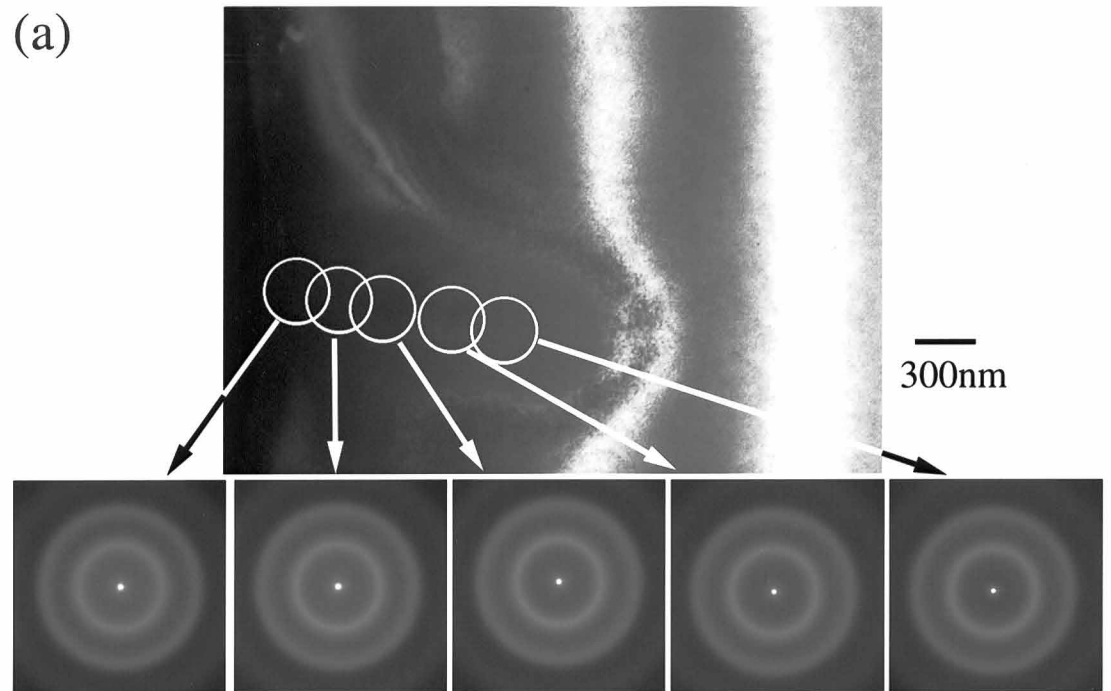
Fig.III-9 Thickness dependence of halo intensity from fully
amorphized areas. (a)Halo ring patterns were obtained from five
fully amorphized area having different thikness. The thickness
was estimated by thickness fringes.(b) The measured halo intensity
and the fitted curṼe $I_0(t)$. (E=2.5MeV, T=25K)
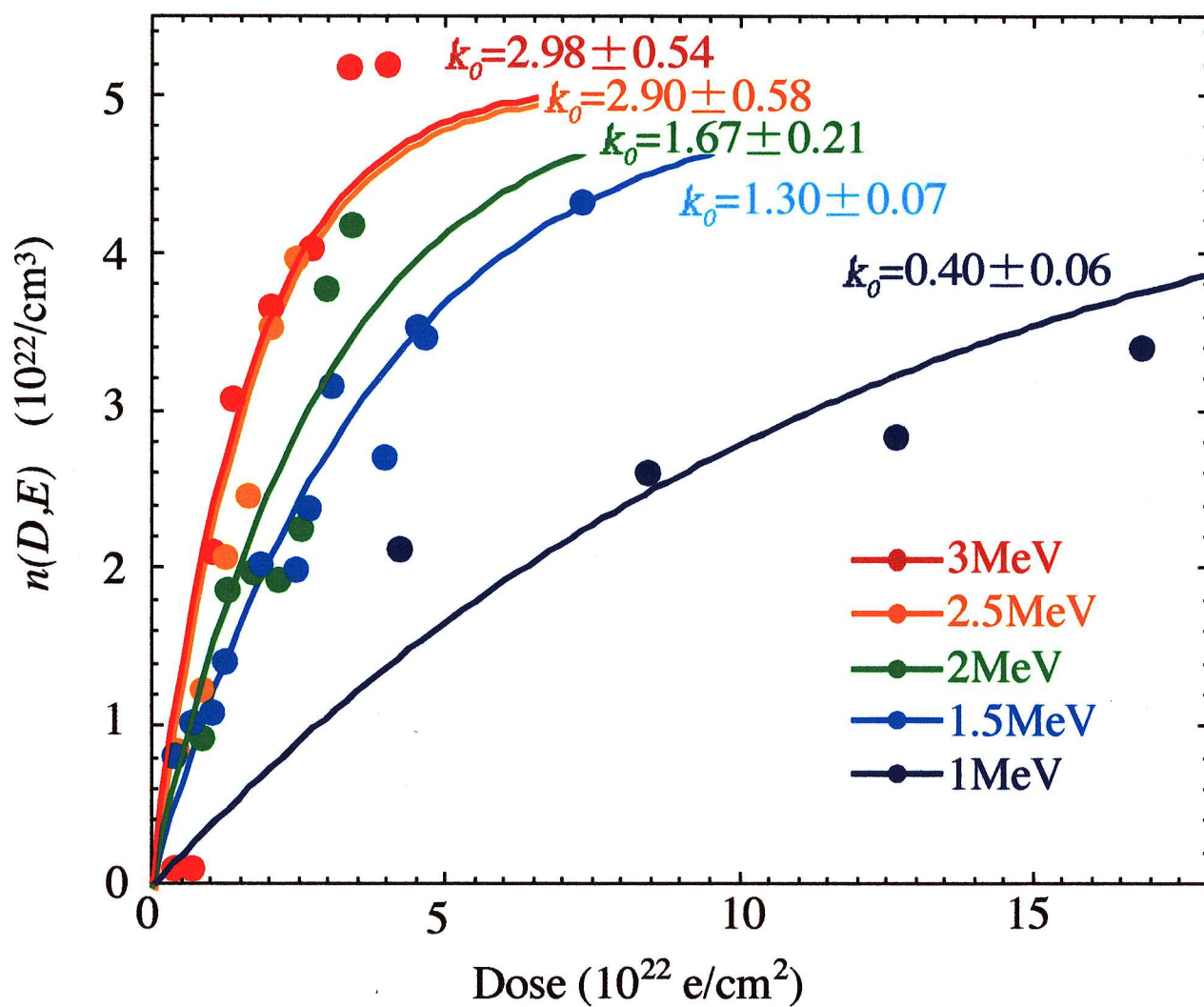
Fig.III-10   The number of atoms included in *a*-Si per unit volume, *n*.
The normalization shown in Eq.(III-8) were applied to the measurements
of halo intensity.
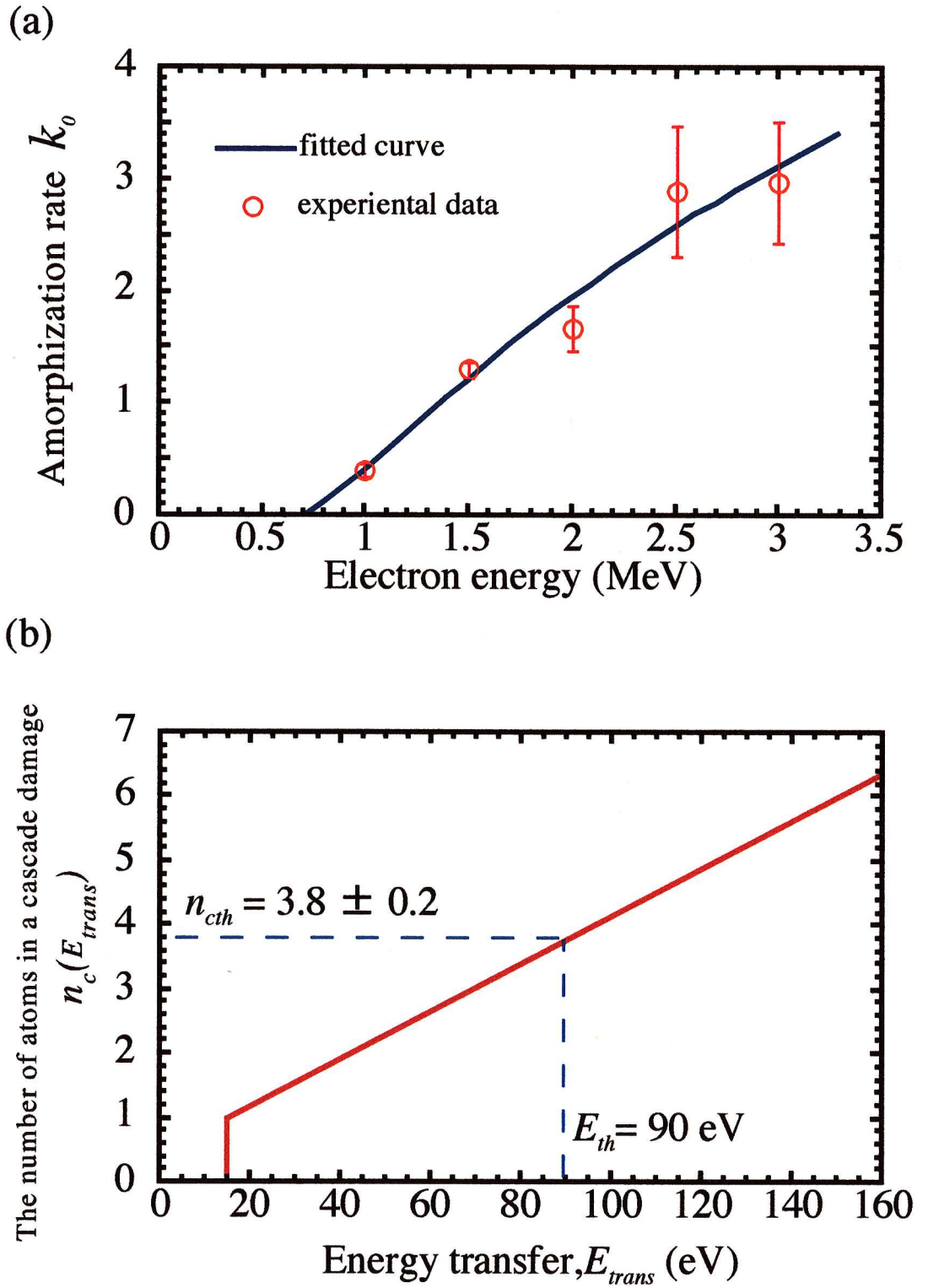
Fig.III-11 (a)Experimental k_0 and the fitted curve (Eq.(III-10)). The suitable values of the fitting parameters are E_{th}=90eV and α=0.037. (b) $n_c(E_{trans})$ obtained by substituting α=0.037 into Eq.(III-7). In addition, by substituting $E_{trans}=E_{th}(=90\ \text{eV})$ into the determined $n_c(E_{trans})$, we obtain $n_{cth} \equiv n_c(E_{th})$=3.8±0.2, which is the number of atoms included in the smallest cascade which contributes to amorphization.
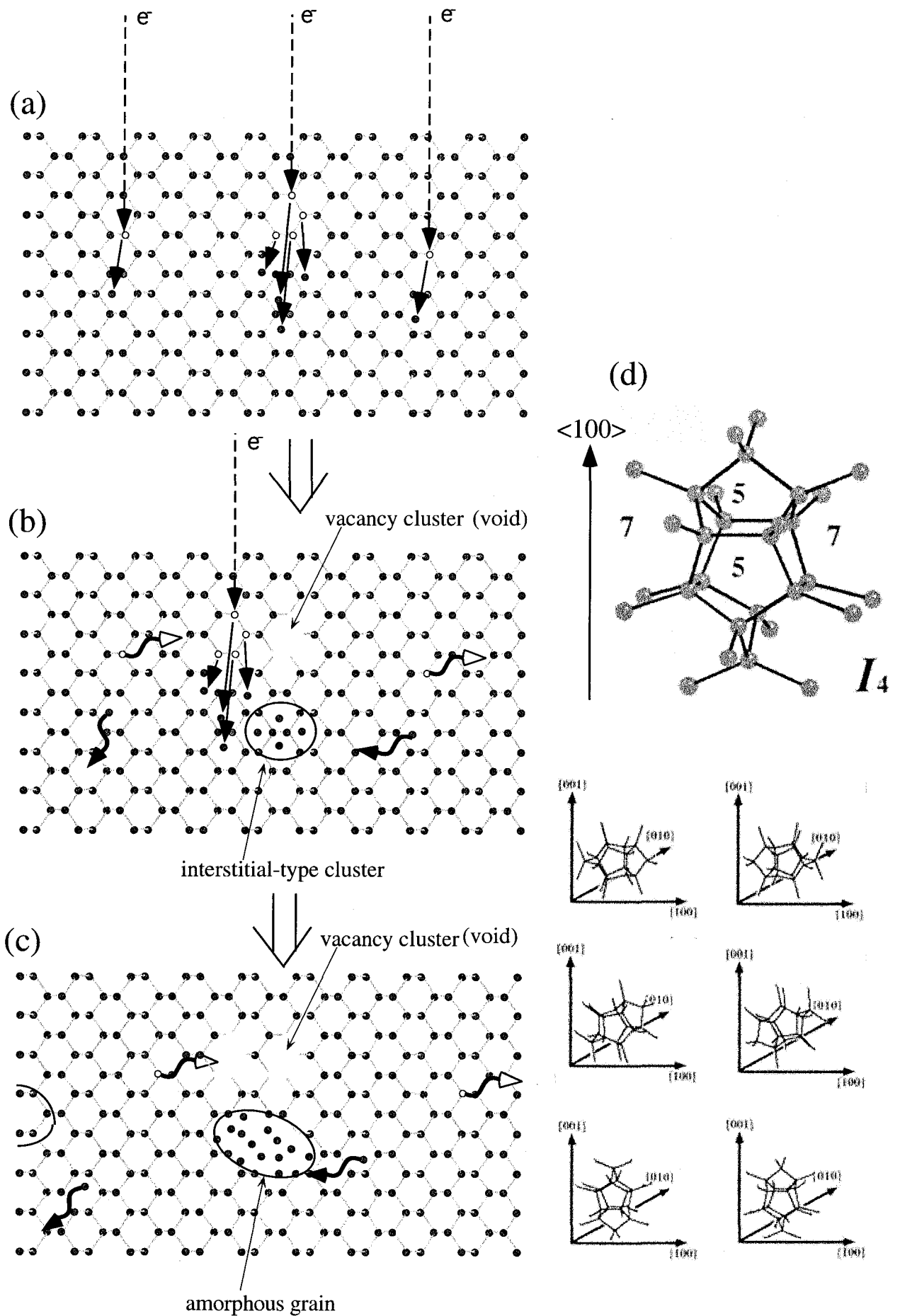
Fig.III-12 (a)-(c) Schematic illustration of the new amorphization mechanism.
(d) The structure of I4 and its six orientation variants. In contrast to the {113}
defect structure, the I4 structure has no periodicity in any direction. The structural
characteristic of I4 is compatible with the structure of *a*-Si.
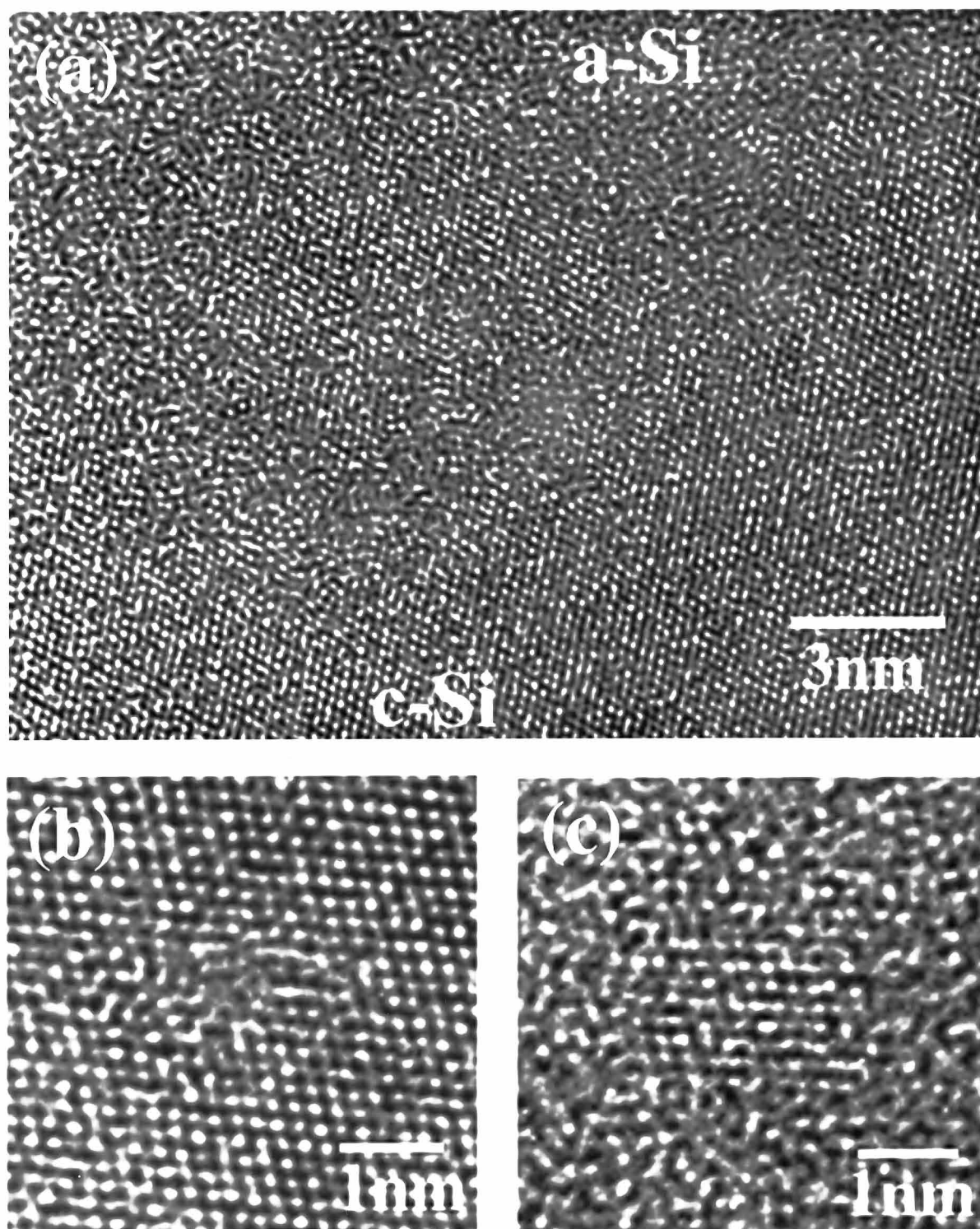
Fig.III-13   Post-irradiation HRTEM observation of a translational region between *a*-Si and *c*-Si. (a)The structural transition at *a-c* interface is very rough and complicated. There are many (b) localized amorphized areas in the damaged crystal and (c) many fragmented *c*-Si areas embedded in *a*-Si .
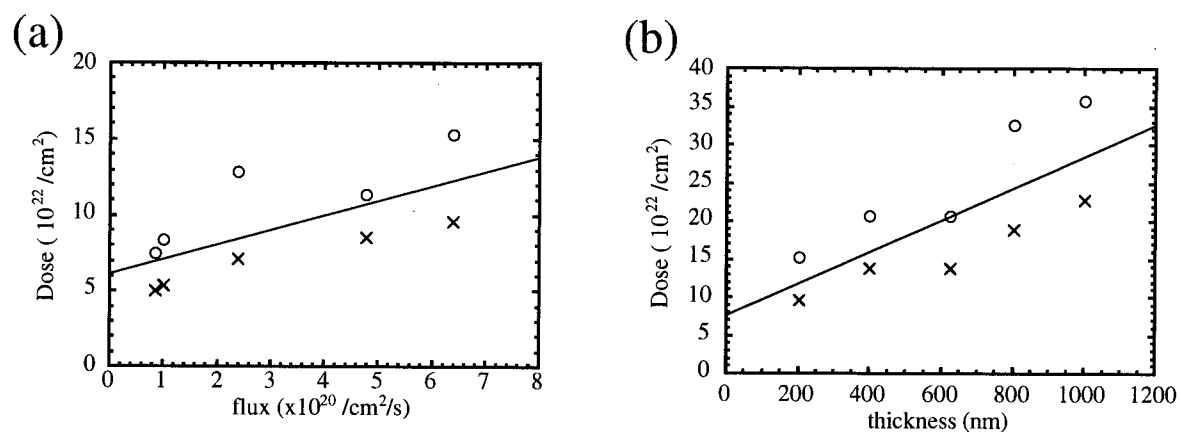
Fig.III-14   Conditions of amorphization in Si by electron irradiation.
(a) Dependence on flux, Φ (E=2.0MeV, T=25K, t=100-200nm)
(b) Dependence on specimen thickness, t (E=2.0MeV, T=25K, Φ=5.4-6.4x10^{20} cm^{-2}s^{-1}).
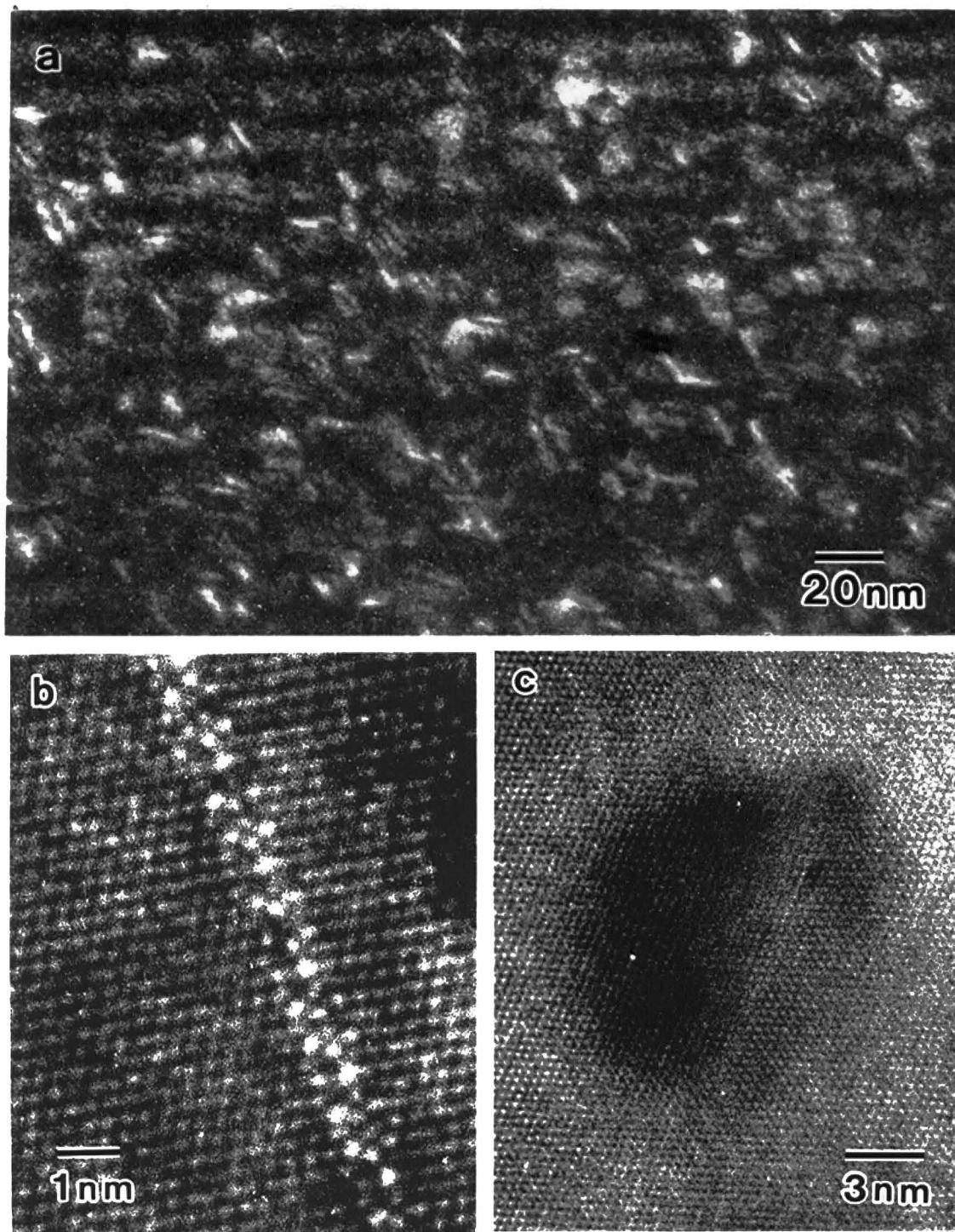
Fig.IV-1   Electron micrographs of {113} defects induced by electron irradiation at 500 ℃ in Si-Ge. (a) The weak-beam-observation from near a [110] direction. (b) The HRTEM images of a side view and (b) an inclined view of {113} defects.
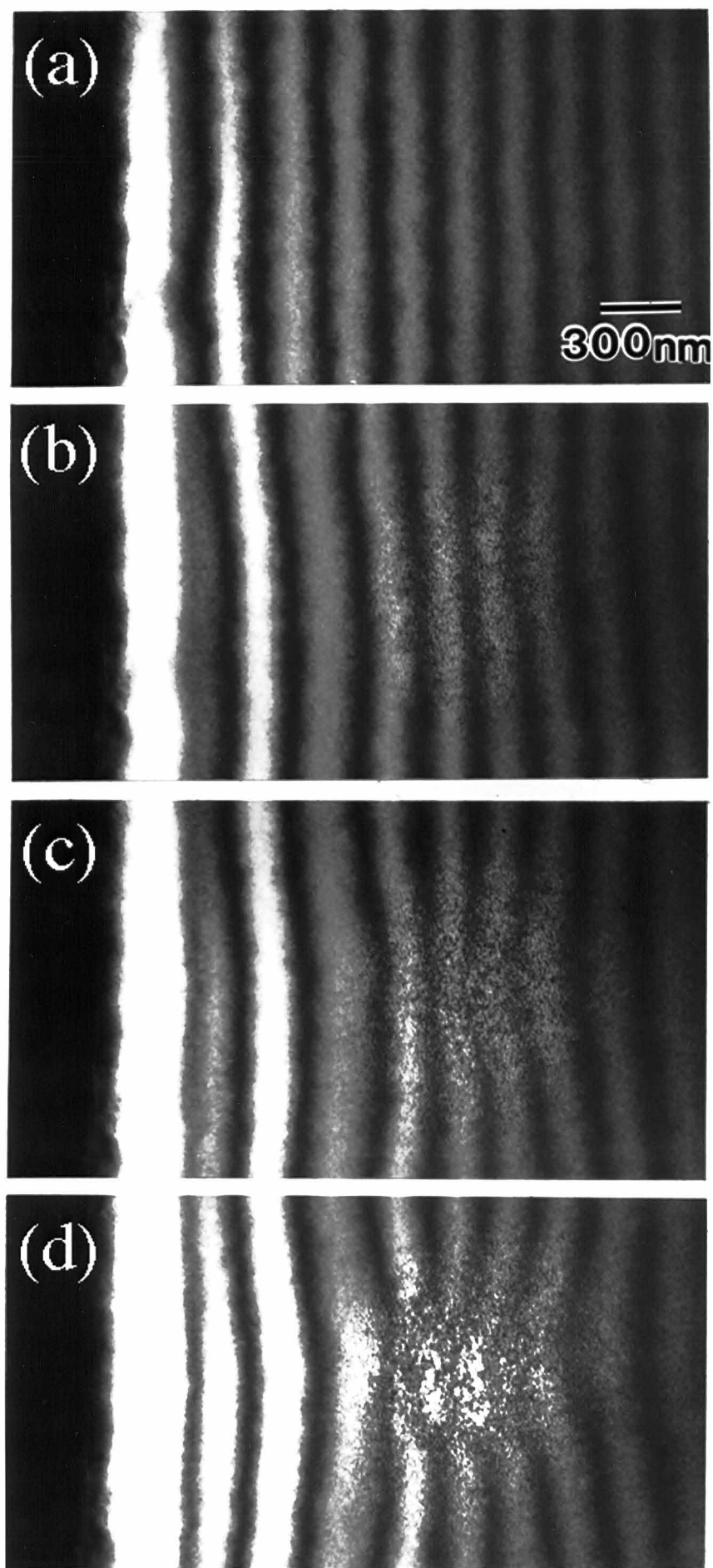
Fig.IV-2   *In-situ* HVEM observation of defect creation
by 2 MeV electron irradiation at 25 K.

(a)
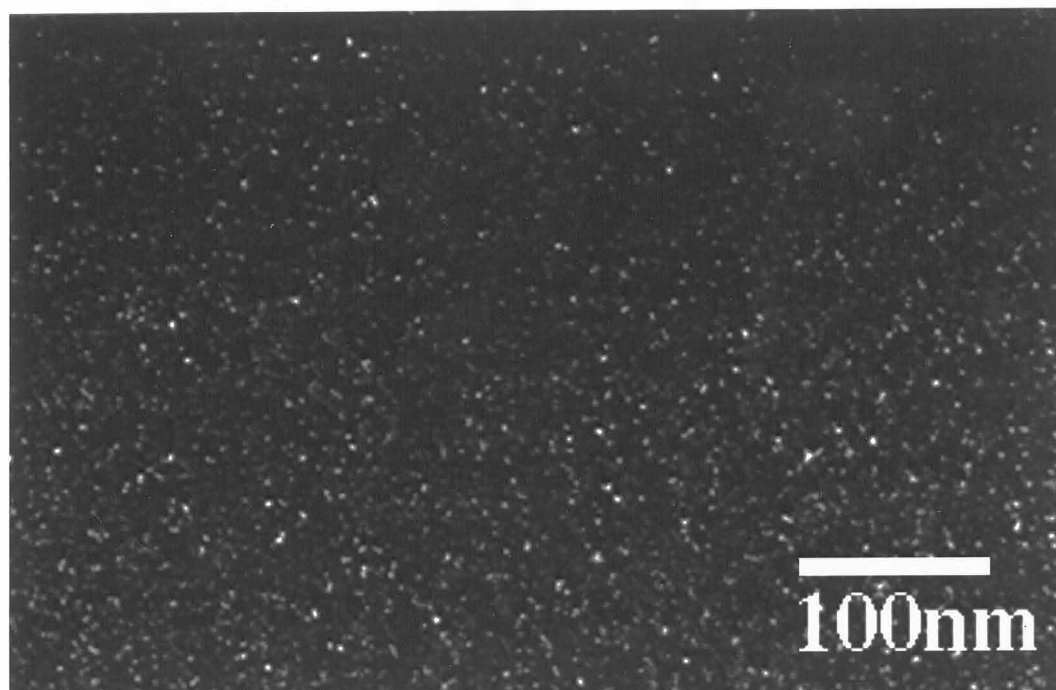
(b)
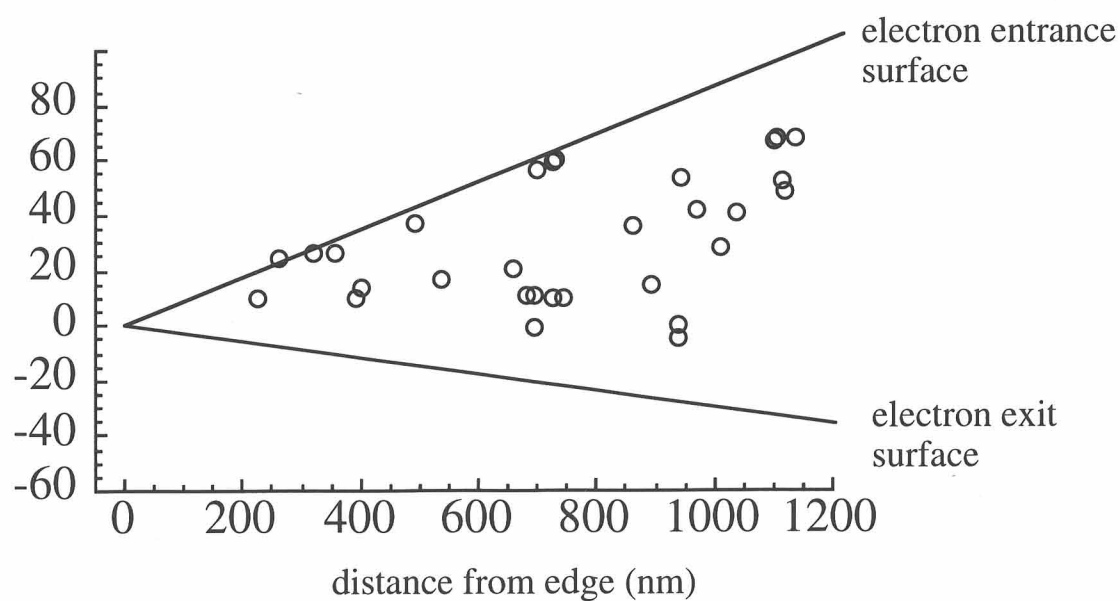
Fig.IV-3   (a) A weak beam image of the area irradiated by 2 MeV electrons. (b) Cross-sectional representation of the measured spatial distribution of the defects.
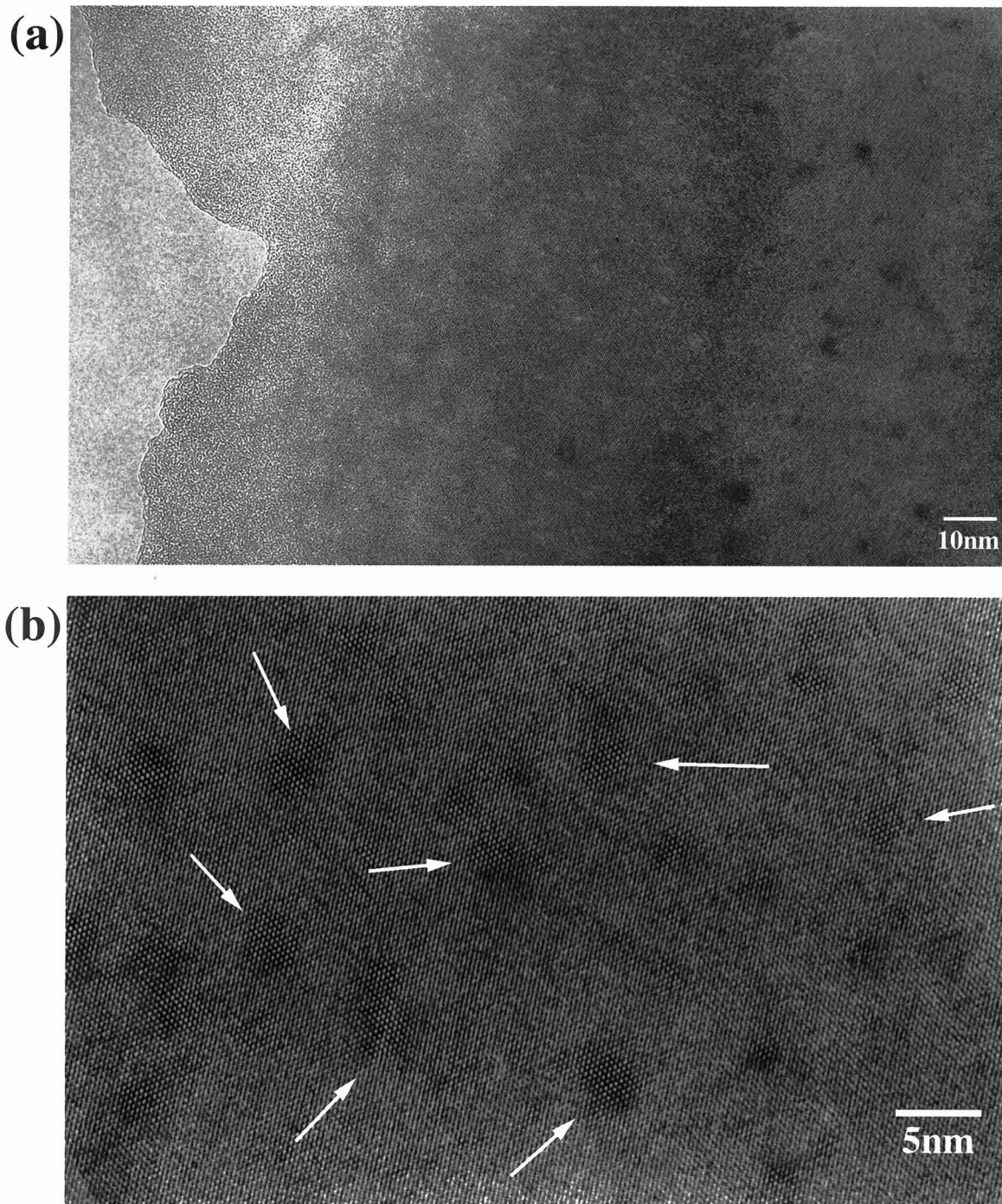
Fig.IV-4　(a) Low magnification image of the irradiated area where a lot of defects are created.(b) Magnified image of the irradiated area. The defects (arrows) show characteristic image contrast.

(A) $\Delta f = -61nm$ -70nm   -80nm

Defect located at
a thinner area
(thickness ~ 13nm)

Defect located at
a thicker area
(thickness ~ 20nm)

1nm

(B)

3nm
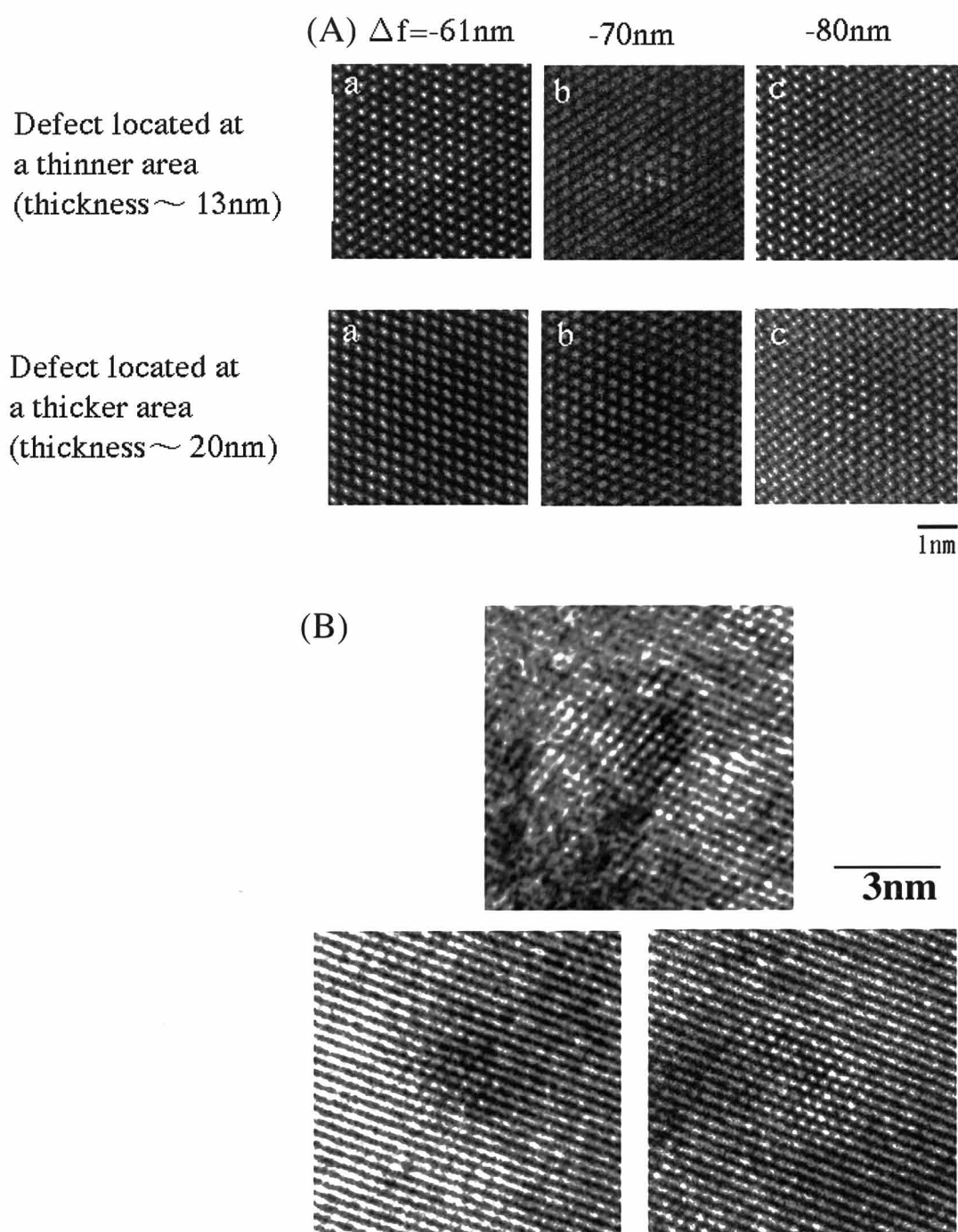
Fig.IV-5   The defects showing the characteristic image contrast.
(A) Post-irradiation HRTEM observation at room temperature of
the defects produced by 2 MeV electron irradiation at 25 K. (B)
In-situ HRTEM observation of the defects produced by 0.3 MeV
electron irradiation at 4.2 K. They show the same image contrast
as that of (A).
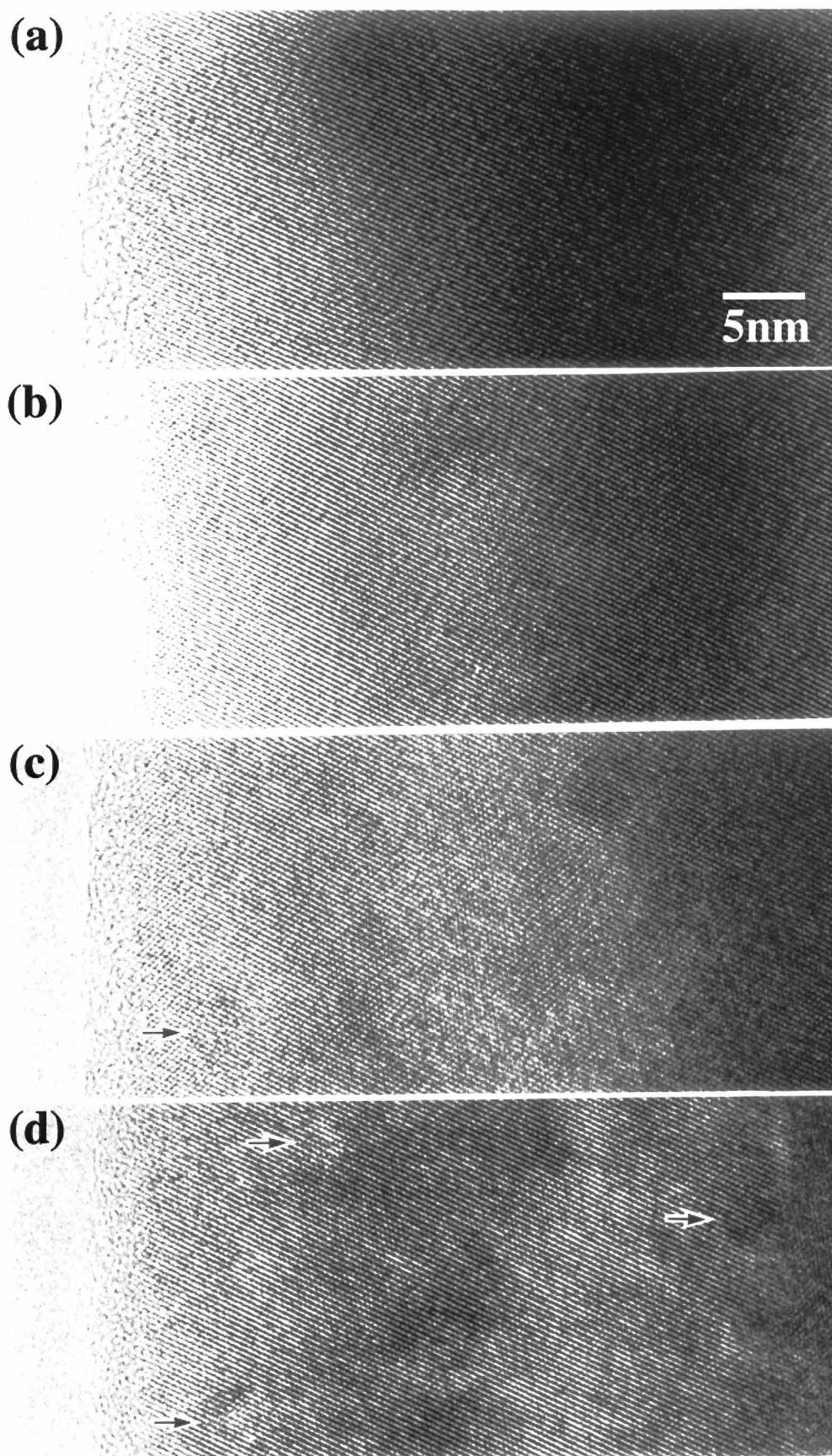
Fig.IV-6　*In-situ* HRTEM observation of a Si crystal under electron (0.3MeV) irradiation at 4.2K. The arrows indicate the defects introduced by electron irradiation.
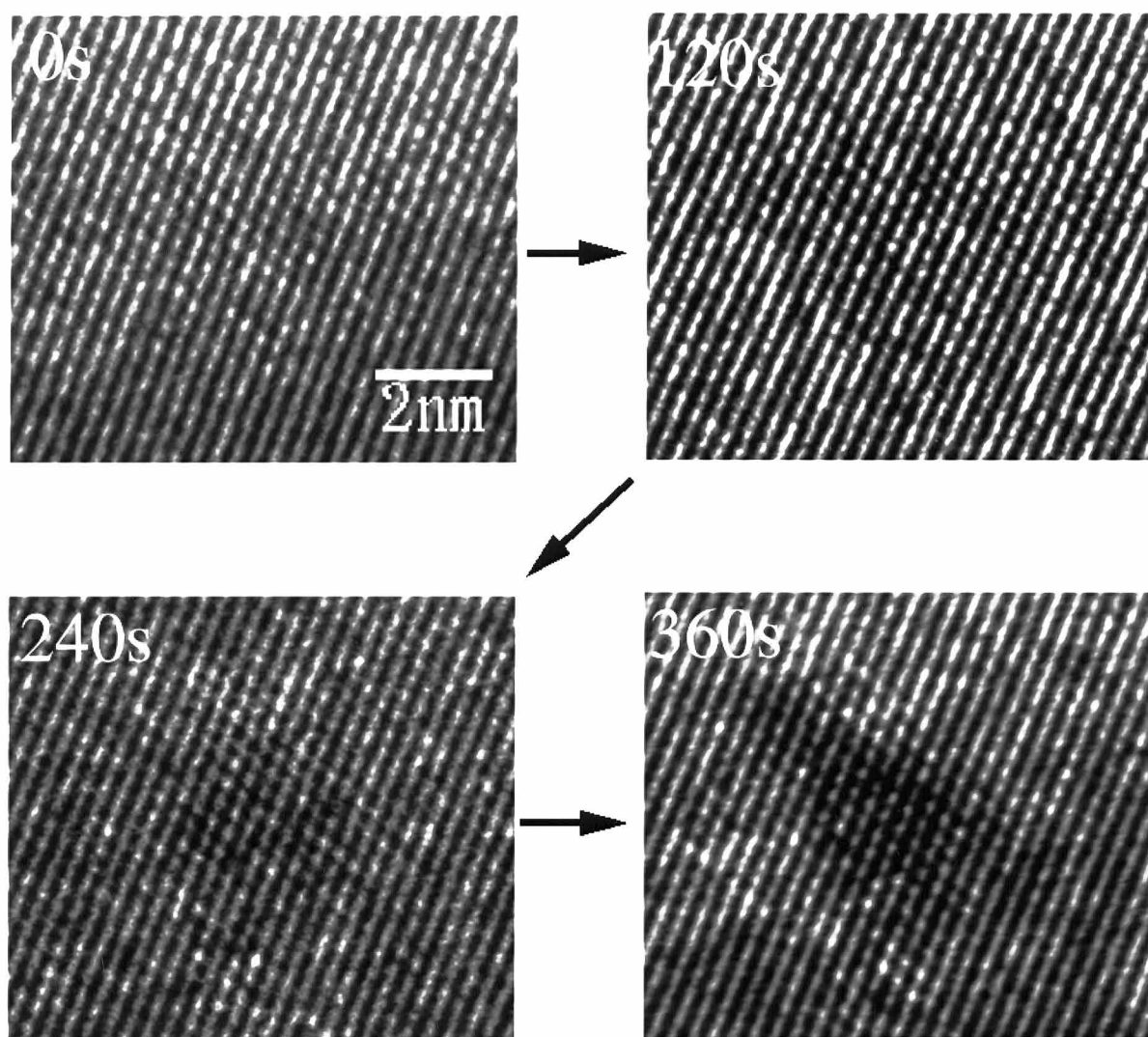
Fig.IV-7   *In-situ* HRTEM observation of the defect creation at 4.2 K. Irradiation time are denoted in each micrographs. The irradiation flux is $7.0 \times 10^{20} e/cm^2$.

(a)
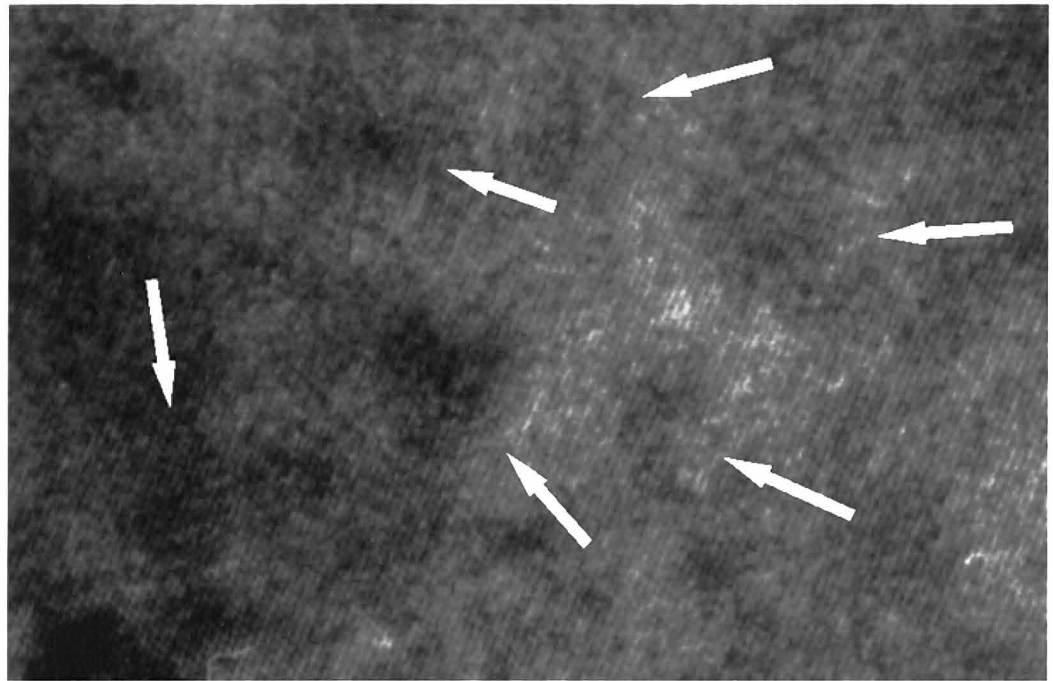
(b)
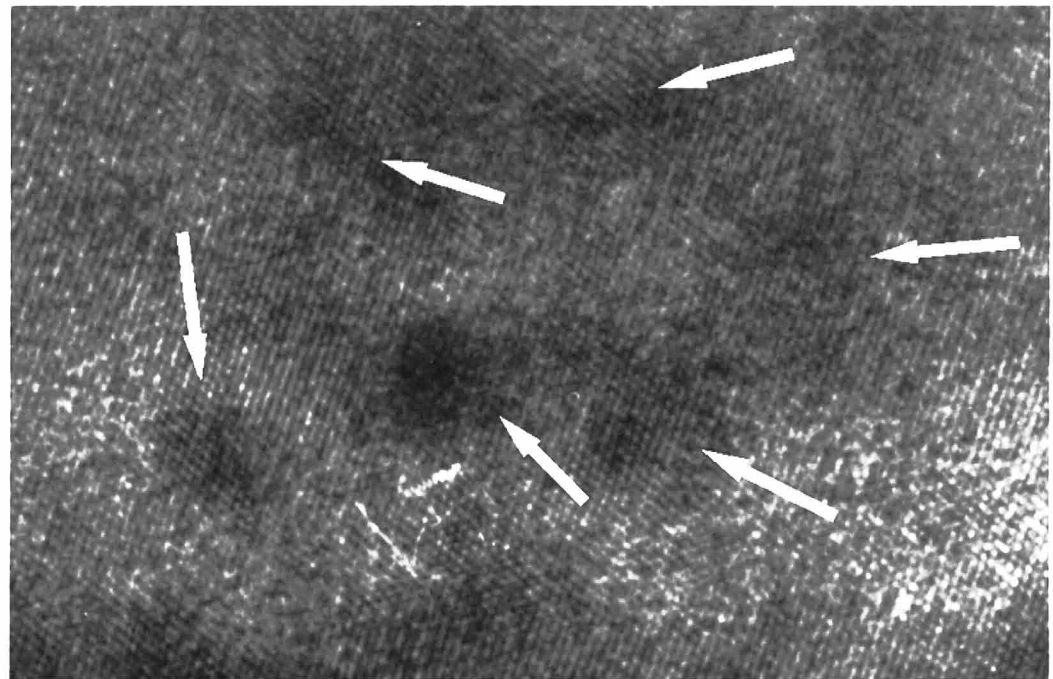
5nm

Fig.IV-8   HRTEM images at (a) 4.2 K and (b) room temperature
of the same irradiated area in which many defects are introduced.
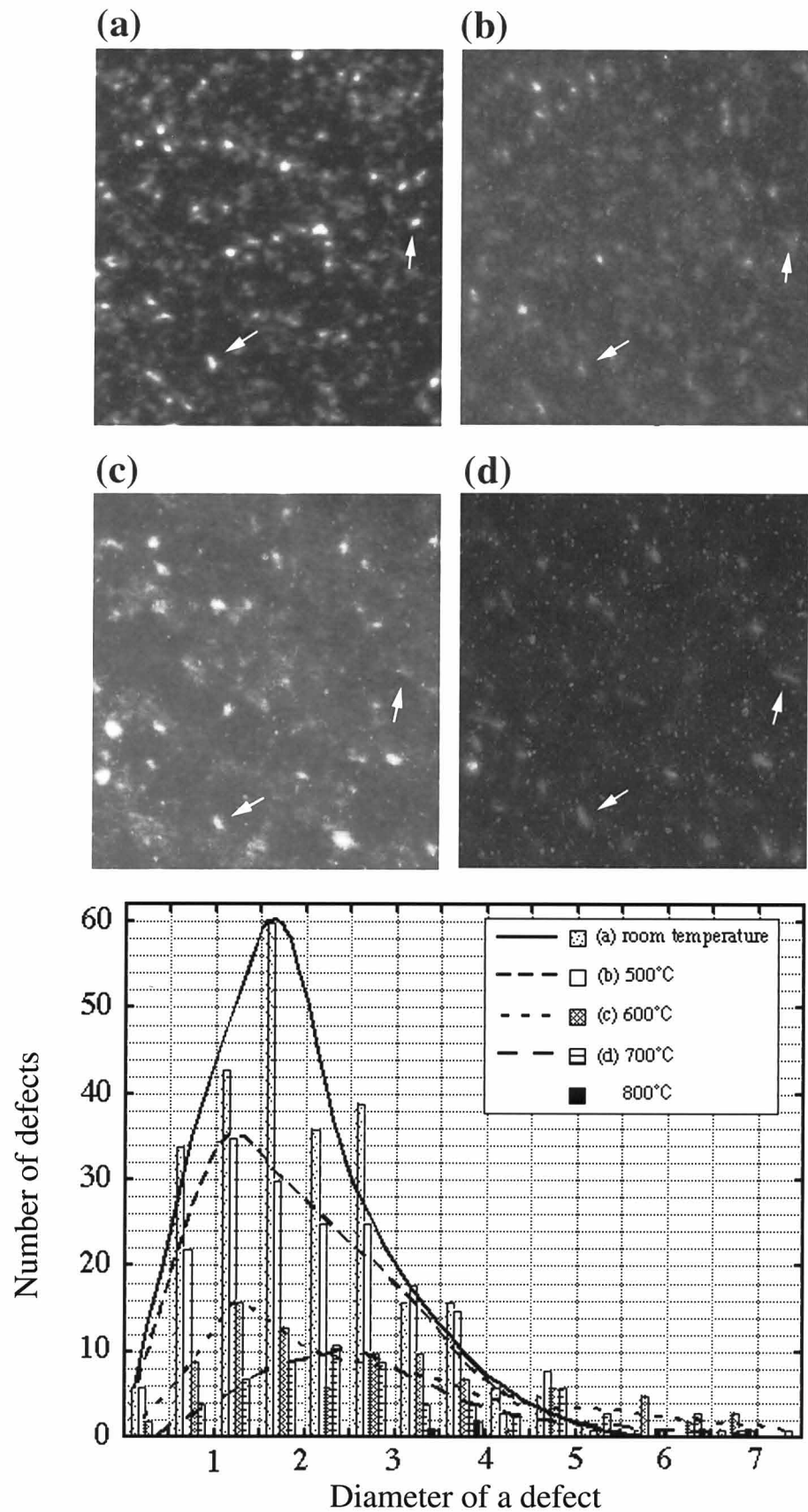
Fig.IV-9   *In-situ* observation of the annealing process of the defects
(a) at room temperature,
(b) after annealing at 500 ℃ for 1 hour,
(c) after annealing at 600 ℃ for 1 hour, and
(d) after annealing at 700 ℃ for 1 hour.
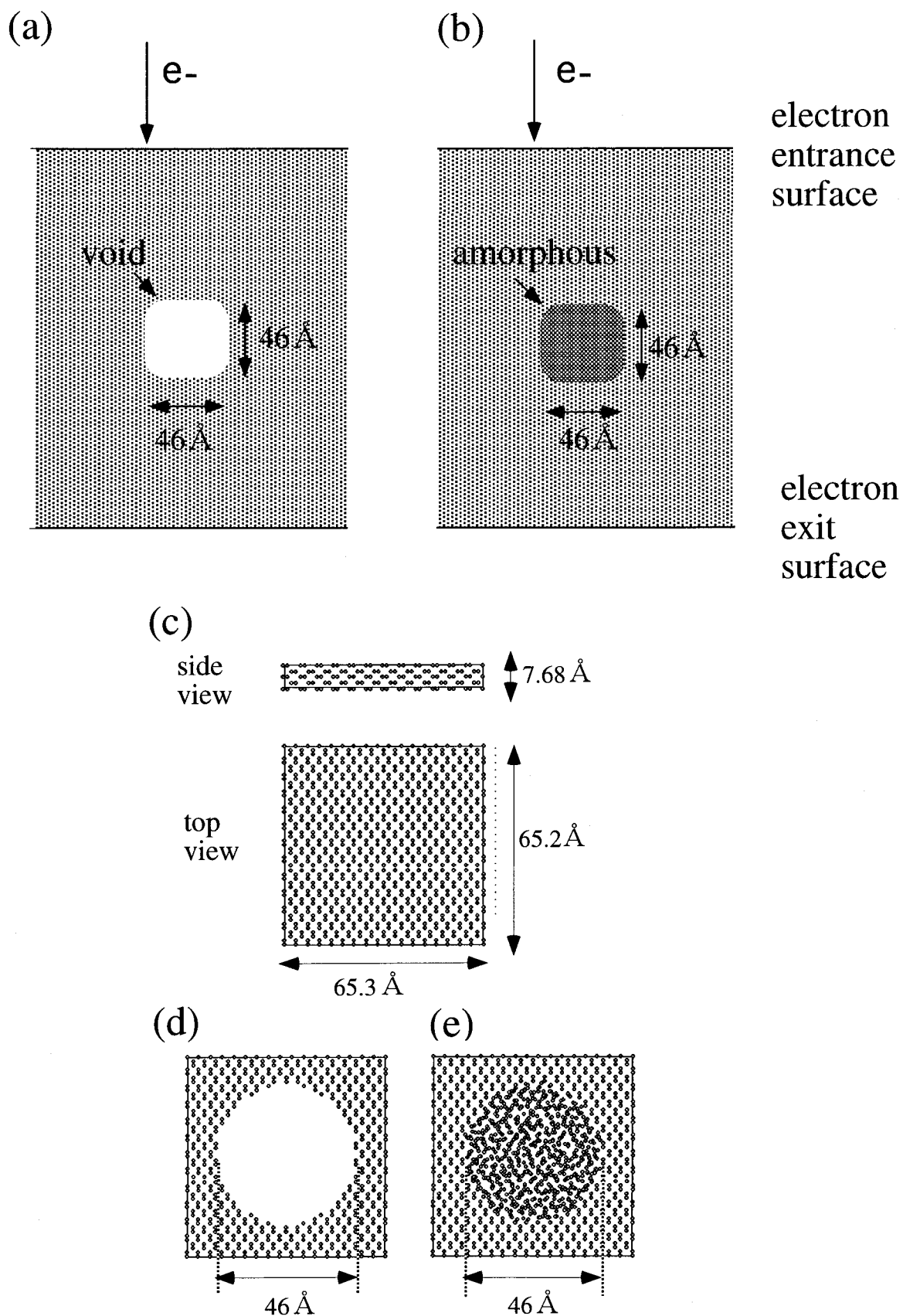
Fig.IV-10   Schematic cross-sectional view of the structures used in
HRTEM image simulations of (a) the void model, and (b) the amorphous
model. The structures consist of stacking of 3 types of supercells shown
in (c),(d) and (e).
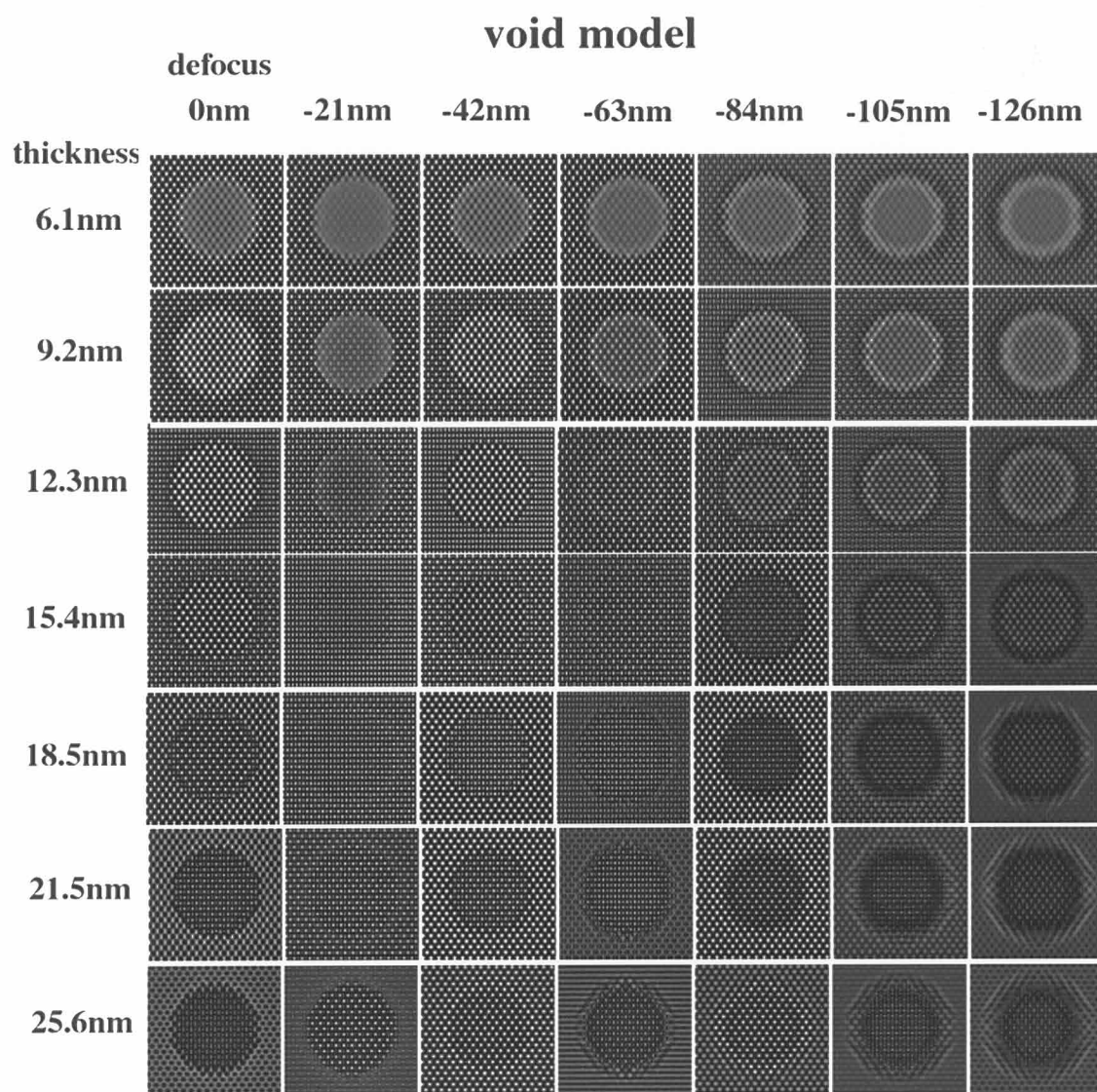
Fig.IV-11　　HRTEM image simulation of the void model.
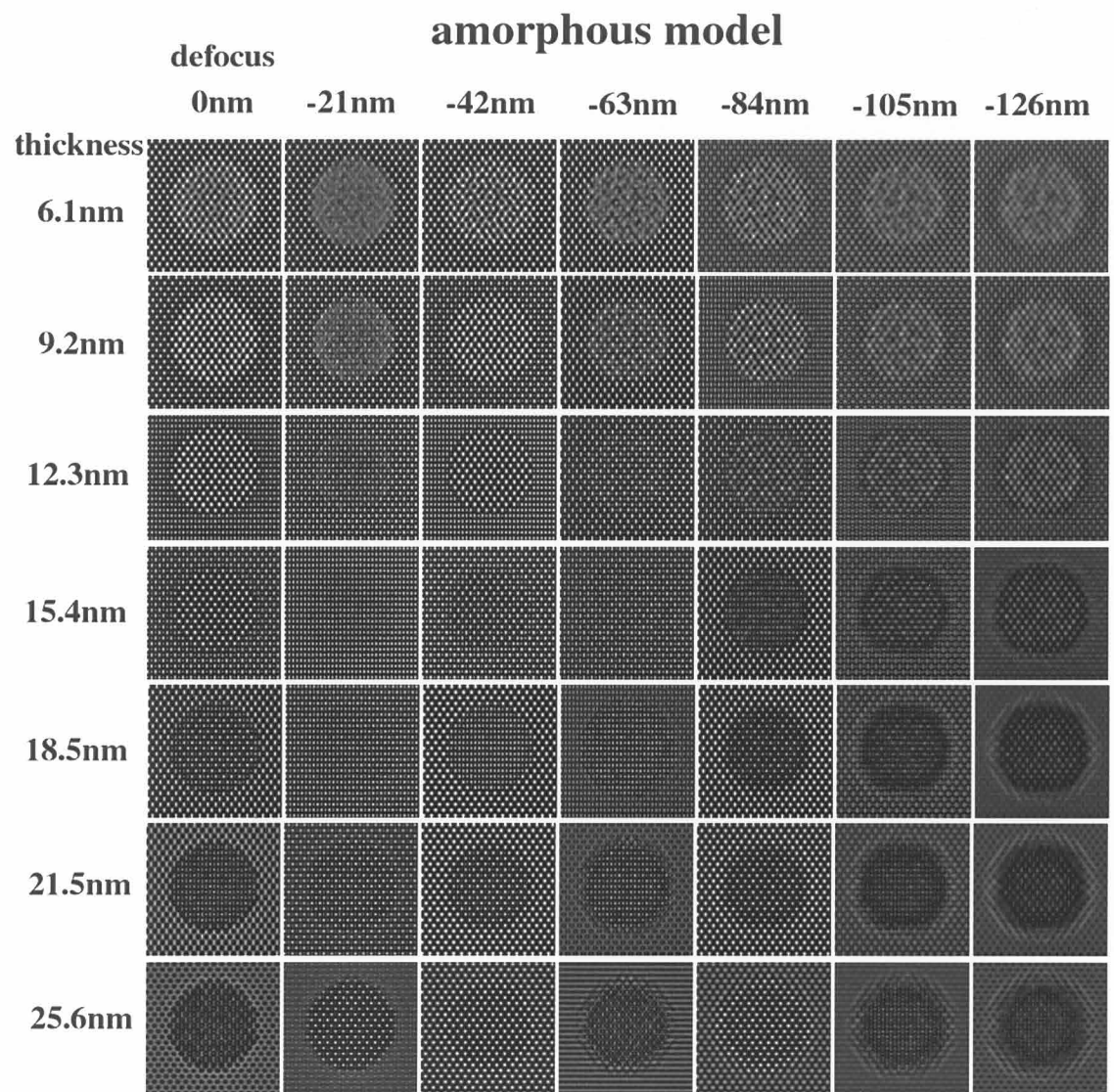
Fig.IV-12   HRTEM image simulation of the amorphous model.

Characteristics	Description
Condition of creation	Electron irradiation · 0.3 MeV at 4.2 K · 2 MeV at 25 K
Size	< 5 nm
Shape	Distorted sphere (not planar)
Distribution	In specimen bulk (not localized near surface)
Thermal stability	Gradually shrinking at 500 - 700℃ within 1 hour

Table.IV-1　Characteristics of the defects created by electron irradiation at low temperatures.
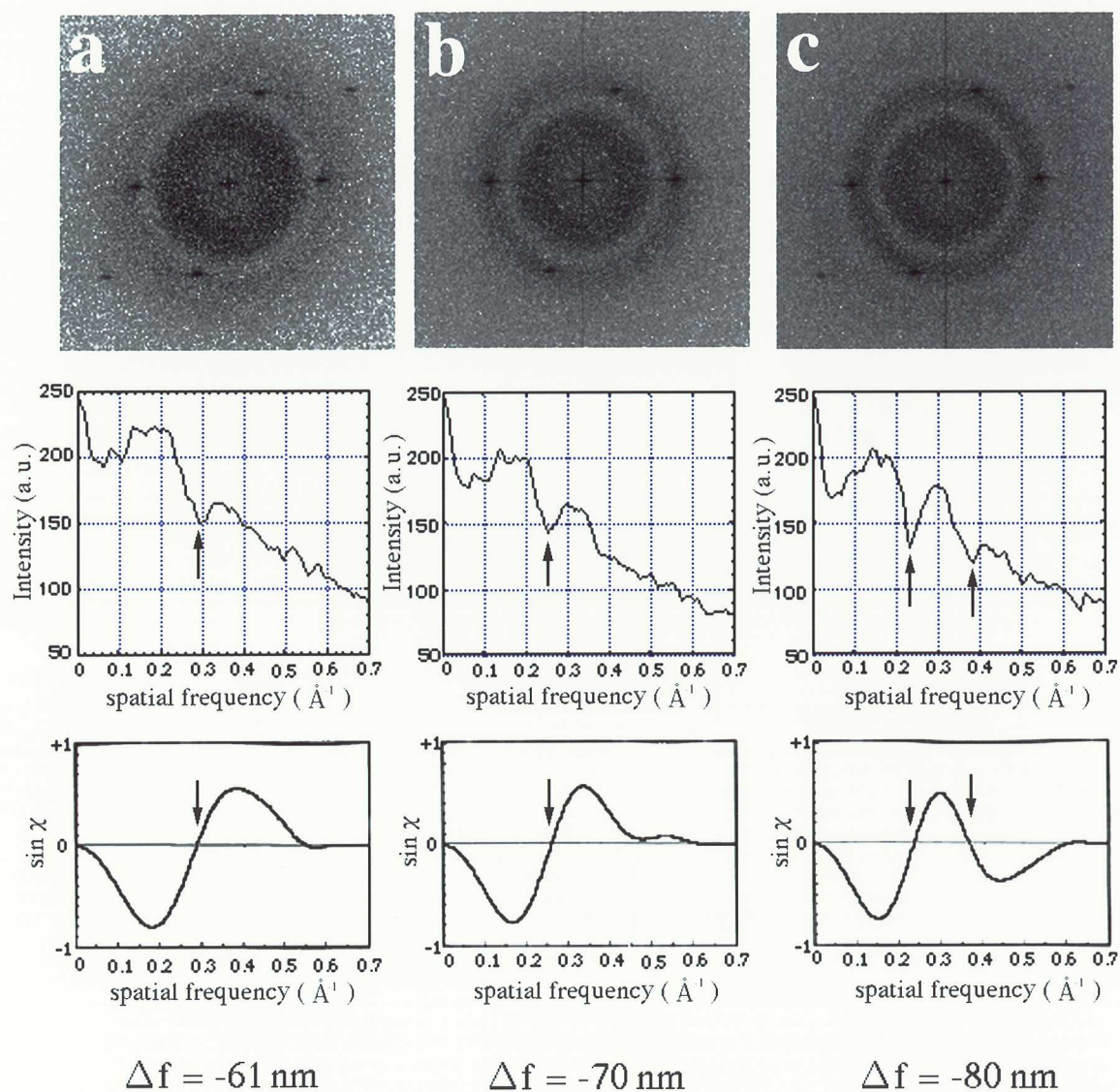
Fig.IV-13   HRTEM images with the different values of defocus of same irradiated area. The defect shown by arrows shows typical change of image contrast.

-68nm   -76nm   -86nm

Observed

Simulated

thickness 13nm

2nm
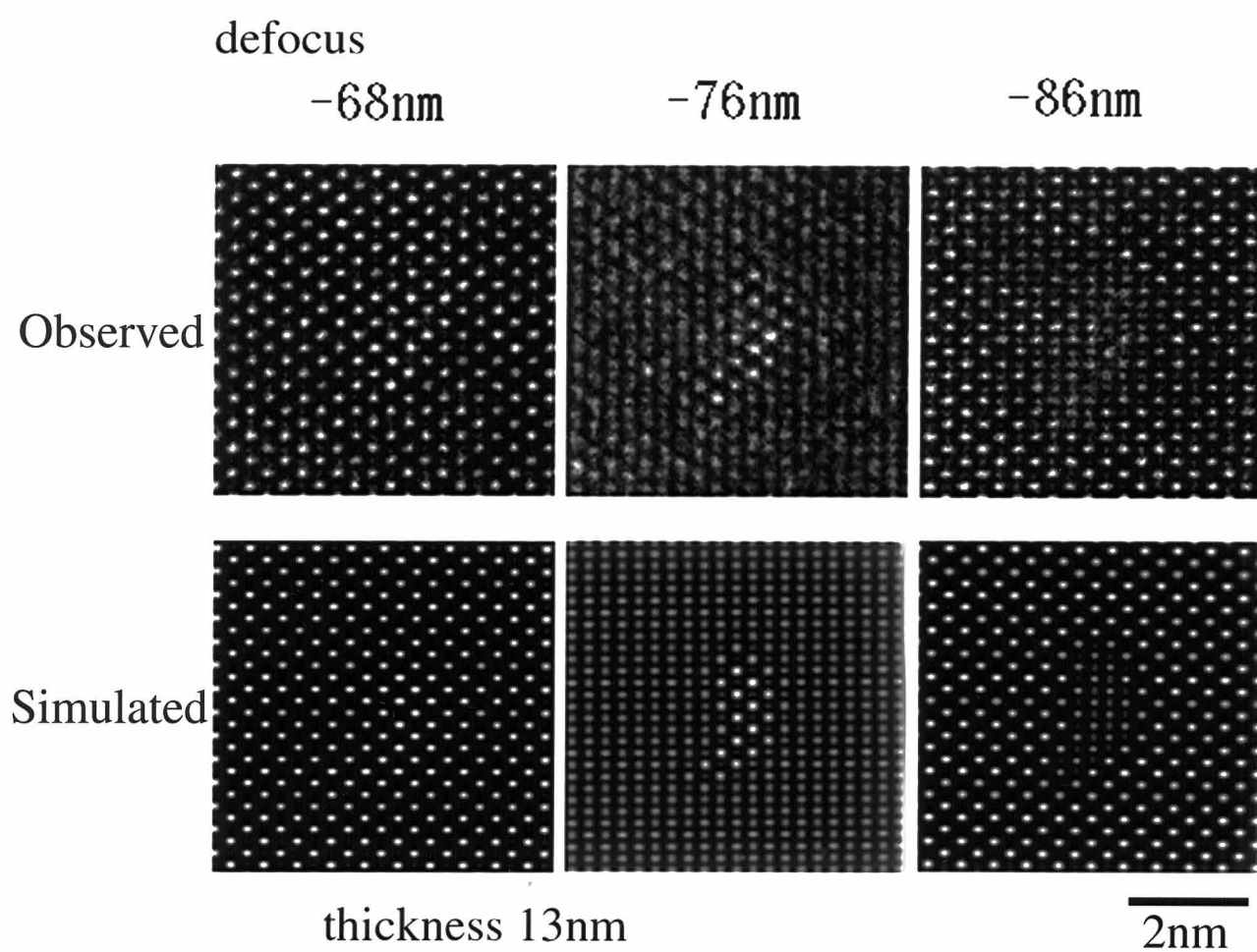
Fig.IV-14   Comparison the refined image simulations of void model with experimental HRTEM images of a defect. The simulated images agree well with the observed images.
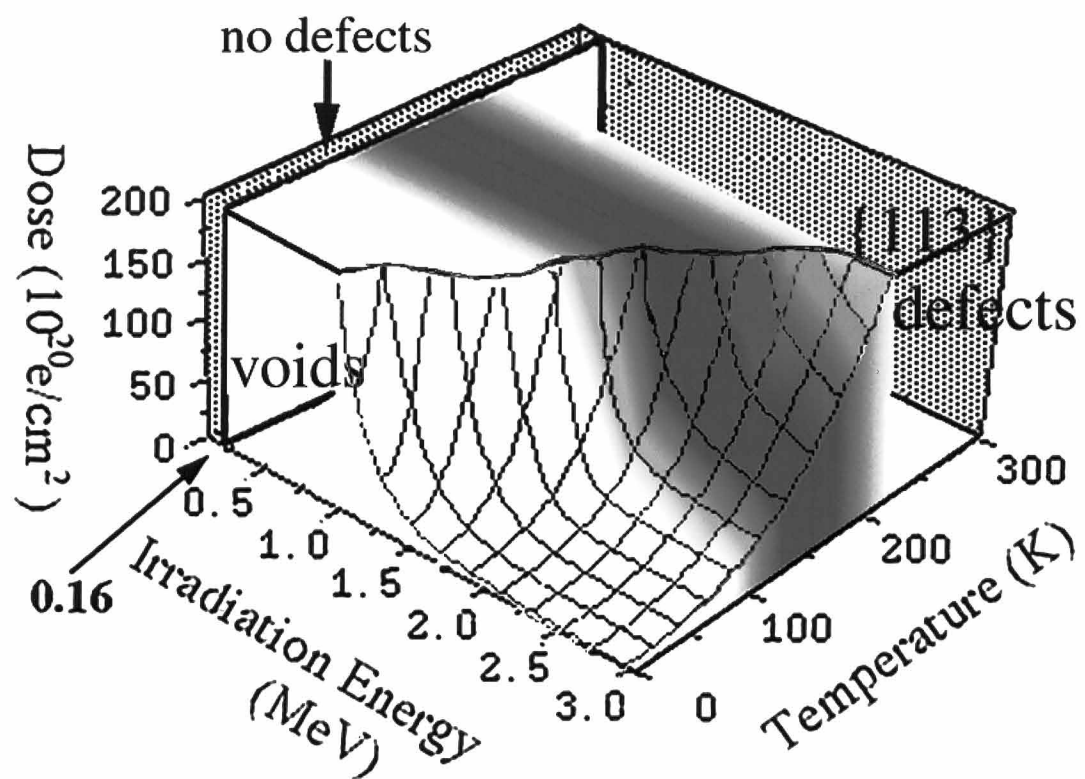
Fig.IV-15　Irradiation conditions on defect creation
expressed by *E*, *T*, and *D*.
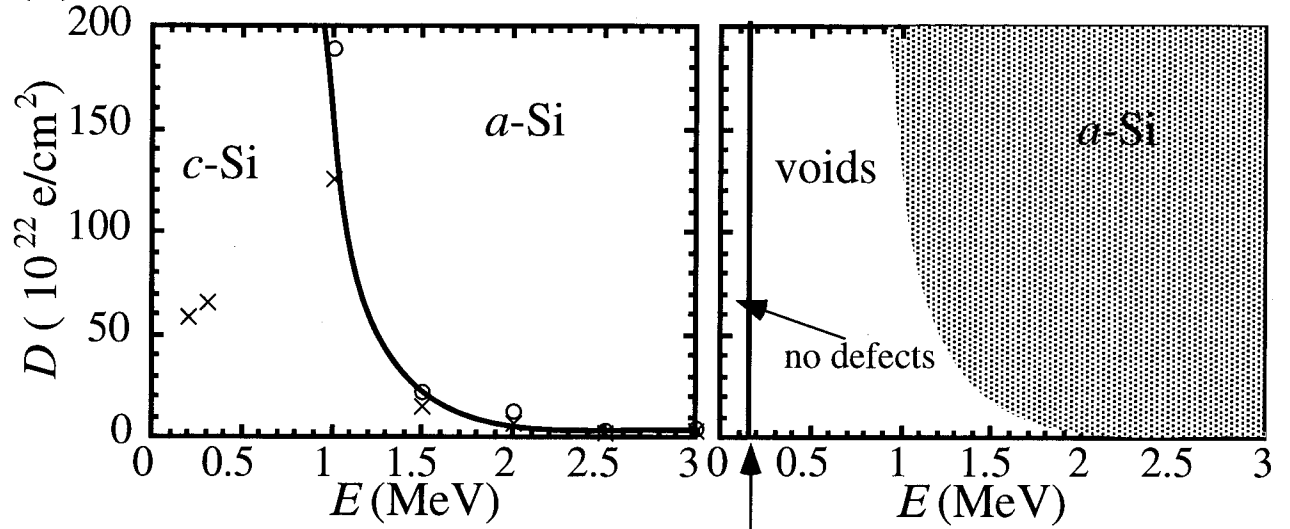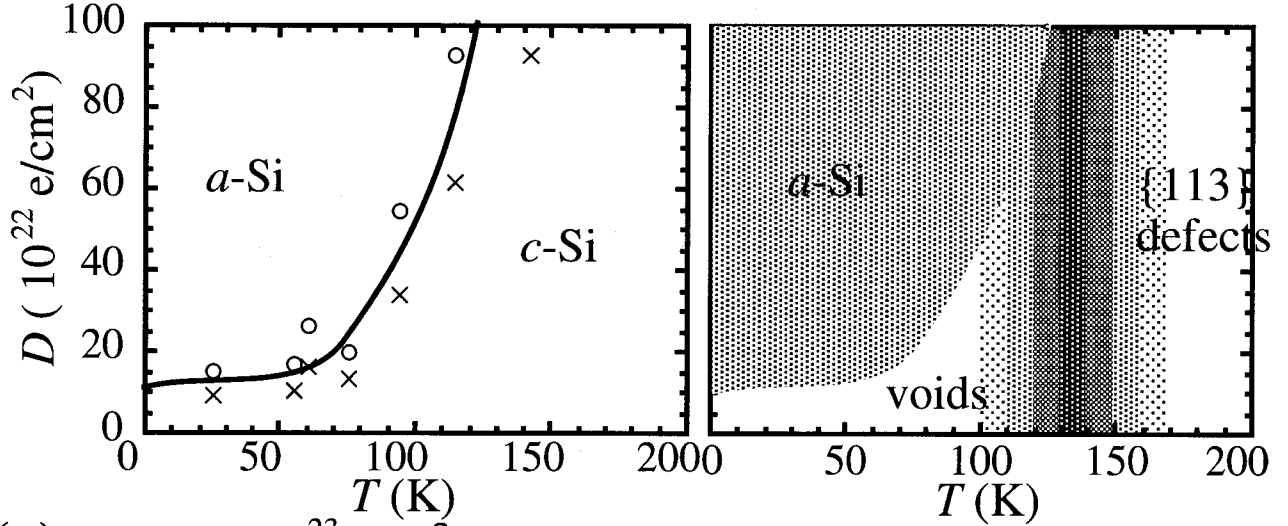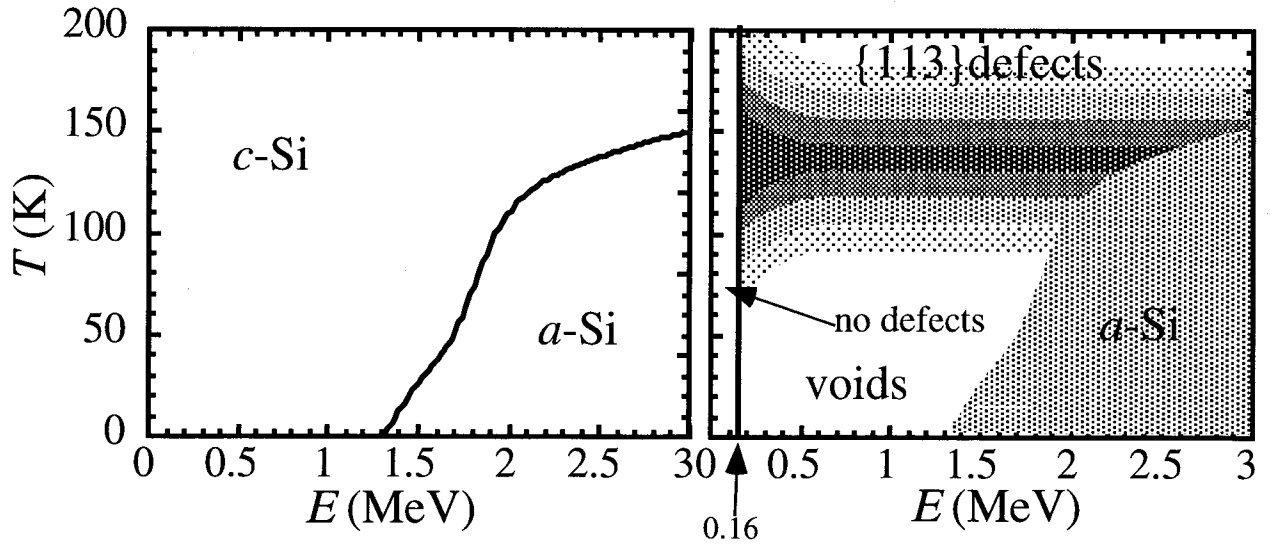
Fig.IV-16.   The condisions of morphization and defect creation expressed
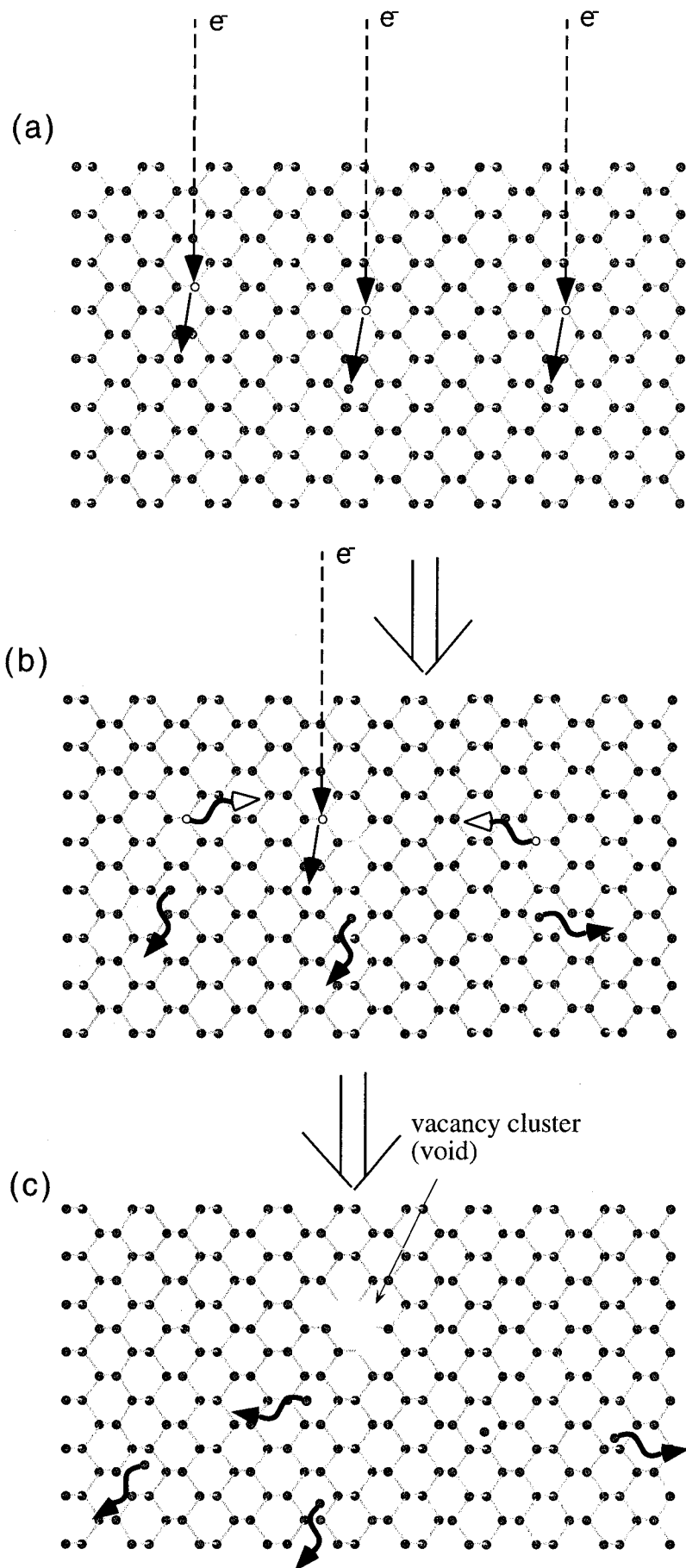as the cross-sectional view of Fig.III-3 and Fig.IV-15.

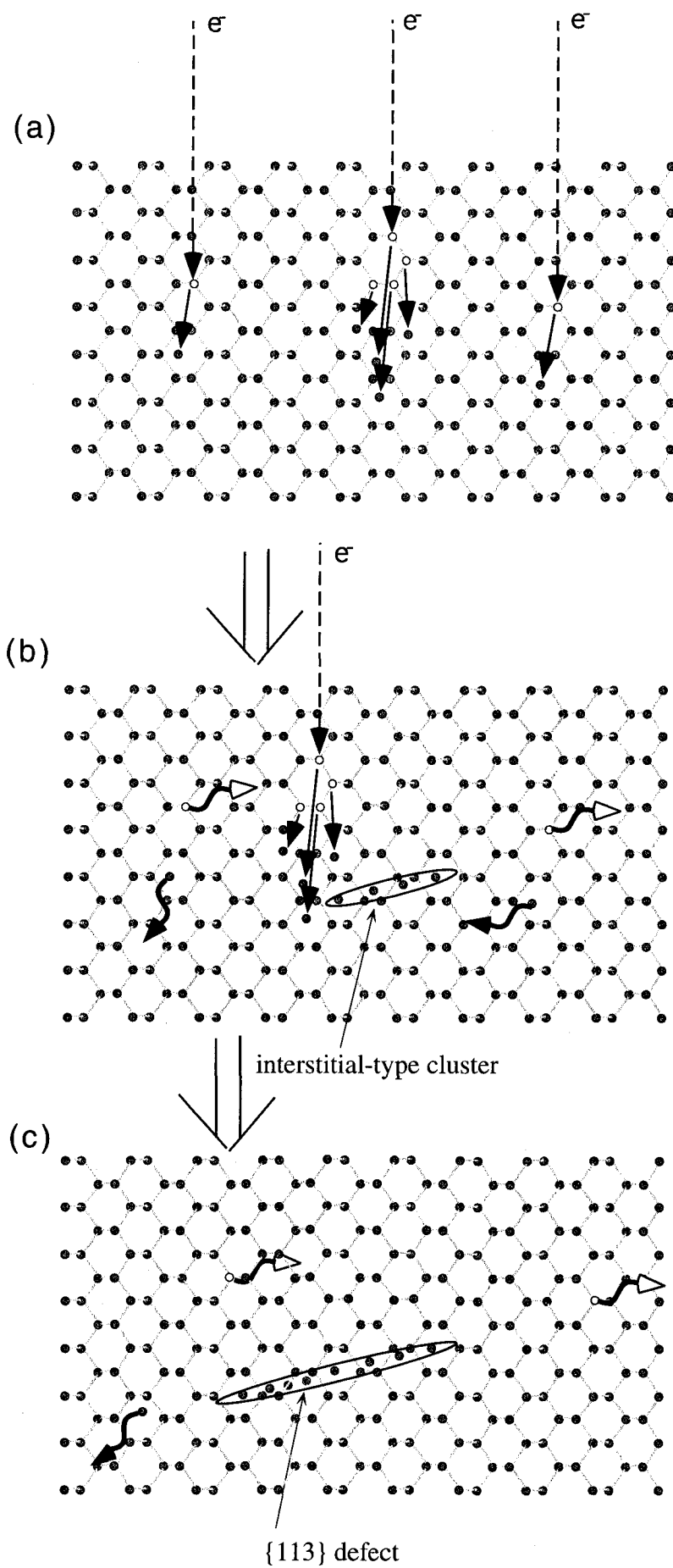Fig.IV-17 Schematic illustration of voids creation mechanism.

(a)

(b)

interstitial-type cluster

(c)

{113} defect

Fig.IV-18   Schematic illustration of {113} defects creation mechanism.
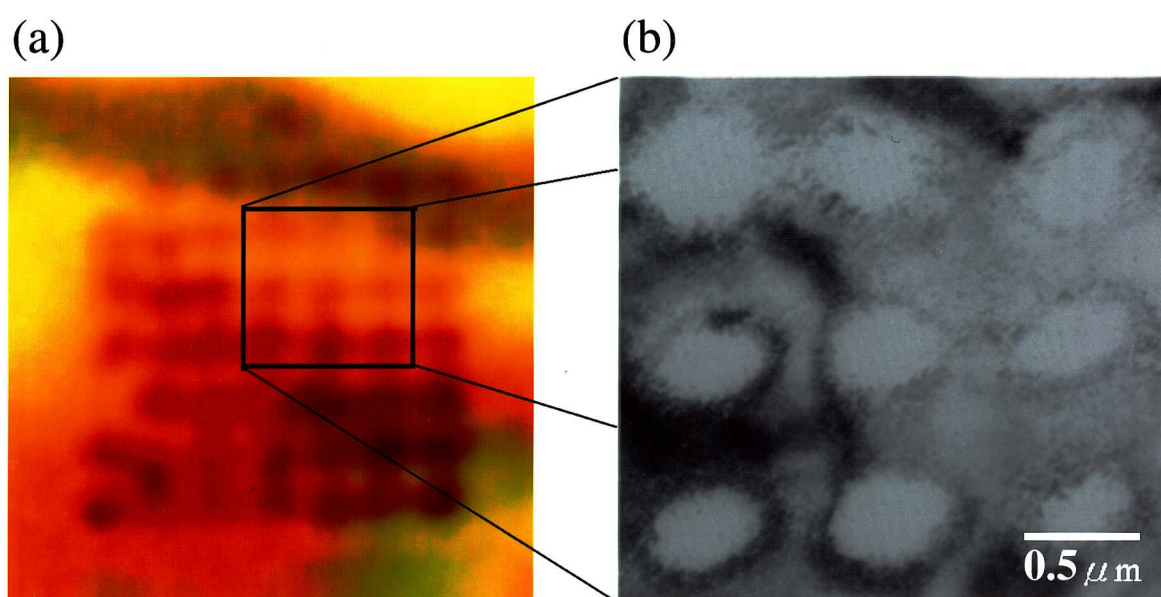
Fig. V-1   Two dimensional square lattice of a-Si dots created by electron irradiation in *c*-Si film. (a) Optical photograph. (b) Electron micrograph.
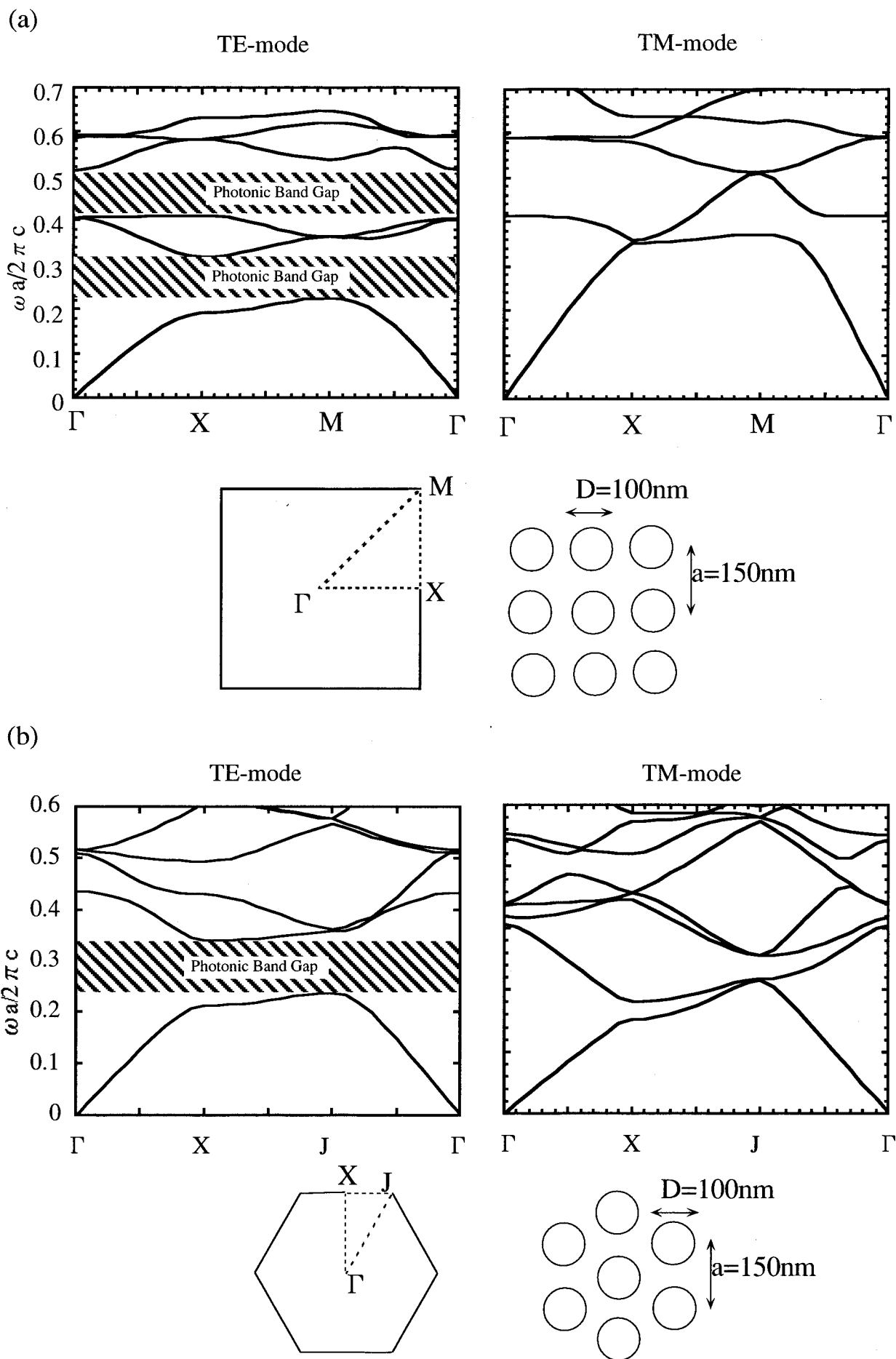
Fig.V-2 The band structure of 2D (a) square lattice and (b) triangular lattice of air rod in c-Si film. Band gaps exist in TE mode of both structure. Lattice parameters and Brillouin zones are also shown.